Doctoral Dissertation

Numerical Analysis on the Pile Loading in Sand Considering Large Deformation and Particle Crushing

Wu Yang

Graduate School for International Development and Cooperation
Hiroshima University

September 2013

Numerical Analysis on the Pile Loading in Sand Considering Large Deformation and Particle Crushing

D106560

Wu Yang

A Dissertation Submitted to
the Graduate School for International Development and Cooperation
of Hiroshima University in Partial Fulfillment
of the Requirement for the Degree of
Doctor of Engineering

September 2013

We hereby recommend that the dissertation by Mr.Wu Yang entitled "Numerical Analysis on the Pile Loading in Sand Considering Large Deformation and Particle Crushing" be accepted in partial fulfillment of the requirements for the degree of DOCTOR OF ENGINEERING.

Committee on Final Examination:

H. Yamamoto

Haruyuki YAMAMOTO, Professor

Chairperson

Yasushi HIGO, Professor

Takao YAMASHITA, Professor

Takashi TSUCHIDA, Professor

Graduate School of Engineering, Hiroshima university

Koji ICHII, Associate Professor

Graduate School of Engineering, Hiroshima university

Date: 2013.07.29

Approved:

FUJIWARA Akimasa, Professor

Dean

Date: Sep. 6, 2013

Graduate School for International Development and Cooperation

Hiroshima University

Abstract

The behavior of piles remains one of the largest sources of uncertainty in geotechnical engineering. Much of the uncertainty is because of a lack of understanding of the physical mechanism that controls the characteristics of deformation, strain and stress in the soil during pile installation and loading. It is hard to estimate the behavior of pile because that soil particles around the pile tip tend to be crushed when the external force exceeds their crushing strength. Another difficulty is to describe the mechanical behavior of structures interacting with soil. Simulating behaviors of sand crushing and sand-pile interactive region around pile tip provides insight understanding of the pile loading and penetration process. The numerical results will make valuable suggestions to the pile design into crushable soil in practical engineering.

The deformation of soil under complex stresses in surrounding of the pile tip exhibits typical large deformation behavior. It is important to consider the geometrical nonlinearity caused by the large deformation to establish a model of the actual behavior of the structure. This study aims to implement a thorough numerical analysis on sand behavior around pile tip considering effects of large deformation and mechanical feature changes of sand crushing.

To investigate the mechanical behavior of granular material crushing, the experimental and numerical research of sand particle crushing is conducted respectively. The high compression test apparatus is proposed and three kinds of granular materials are tested to be crushed. The mechanical behavior and crushing ability of three granular materials are analyzed. An elastoplastic constitutive model is employed to represent the mechanical behavior of sand in numerical analysis. Its constitutive tensor is obtained for being integrated with finite element analysis.

This study presents a numerical analysis on pile loading with different tip shapes in sand under three kinds of surcharge pressures. The innovation of this study is that numerical analysis of pile loading is implemented in consideration of both the geometrical and material nonlinearities. The elastoplastic constitutive model and joint element are employed to represent the behavior of sand ground and interactive region. A mixed incremental method for the UL method is integrated with finite element method to solve large deformation problem in this study.

The numerical values of normalized bearing stress and displacement is compared with the experimental results. It is found that numerical values by large deformation can improve the prediction accuracy than that by small deformation and agree well with the experimental results. The predicted results show that the distributed shape of the high-level mean stress is ellipse and becomes wider with larger surcharge pressure and displacement. The distributed shape of the high-level deviatoric stress appears firstly near the edge of pile tip and forms the shear band.

The effects of pile tip shape on sand behavior around pile tip are investigated. The axial, radius and circumferential stress and axial, radius and circumferential strain contours around pile tip are displayed. A significant finding is that an underreamed pile with a smaller convergent angle can prevent crack failure on the pile base surface.

Finally, the mechanical behaviors of three selected elements beneath the pile tip at different depths are examined. The predicted relationship between the stress ratio and the deviatoric strain shows that the stress ratio changes for the three elements exhibit nearly the same tendency. The predicted results represent that the volume of element near to pile tip is heavily compressive. The volume of element far from tip slight expands. Such prediction is compatible with the actual deformation of sand in surrounding of pile tip.

ACKNOWLEDEMENTS

First of all, I would like to express my deepest gratitude to my supervisor, Professor Haruyuki YAMAMOTO, for his guidance, patience, encouragement, and continual support throughout my study in Hiroshima University for the past five years. He provided me the chance to study in Japan and spent plenty of time instructing me and guided me to move forward. The dissertation could not be completed without him.

I also express my sincere gratitude to my vice-supervisors, Professor Yasushi HIGO and Professor Takao YAMASHITA, for their thorough review of my dissertation and their valuable suggestions and comments in revising the dissertation.

Special thanks are due to the members of my Dissertation Committee, Professor Takashi TSUCHIDA and Associate Professor Koji ICHI of Graduate school of Engineering, Hiroshima University, for their constructive ideas on my dissertation. Their innovative ideas and unique insights into the research impressed me a lot and made me progress faster.

I would like to particular thank Professor Wei LI, Shenyang Jianzhu University, who take me into the geotechnical field when I was an undergraduate. Specifically, I would like to thank Professor Daichao SHENG, Newcastle University and Dean SUN, Shanghai University. They broaden my vision and shared me the valuable research experiences when they were in Hiroshima University as visiting professor.

I would like to thank the Japan government for providing the MEXT scholarship for five years. During this period, I can completely focus my time on research.

I also want to express my sincere grateful to all the other members of the laboratory for their

technical help in laboratory test and care in dairy life. Special thank is given to Dr. He HUANG, who provided invaluable help to the compiling of my computer program.

At last, I would like to express my thanks to my wife, Liwei WEN, for her firm support, encouragement and love during my doctoral study. I still express my beloved parents. Their love and support enabled me to complete this dissertation.

Wu Yang

Table of contents

List of Figures

List of Tables

CHAPTER 1

INTRODUCTION

1.1 Research background

As pointed out by White (2002), the behaviour of pile remains one of the largest sources of uncertainty in geotechnical engineering. Much of the uncertain is due to the lack of understanding of the physical mechanism that controls the characteristics of deformation, strain and stress in the soil during pile installation and loading. Until now, most fundamental and convinced aspects of pile design formulation are still relied on experiences and practices (Poulos, 1989; Poulos, 2005). Much of the design of pile foundation is still dominated by estimation of axial capacity (Randolph, 2003). In recent thirty years, tremendous progress has been made in numerical computation analysis of pile foundation. Finite element method (FEM) can be served as a time-saving and flexible tool compared to traditional experienced-based methods. However, numerical analysis of pile test under surcharge pressure is generally challenging because that soil-structure interaction system involving large deformation is complicated. The strength reduction of soil after crushing should also be considered when estimating the bearing capacity of the pile. Some soil particles around the pile tip tend to be crushed when the external force exceeds their crushing strength. It is necessary to employ a suitable constitutive model to represent soil behavior in high compression stress regions. It is pointed by Potts and Zdravkovic (2001) that another important issue is the modeling of the interface between the pile and the soil adjacent to the pile shaft. Deep and comprehensive understanding of pile bearing mechanism cannot be realized without considering particle crushing.

It is revealed that deformation of structure can become large during loading. In order to describe the actual phenomena of structures considering the change in geometry, an alternative must be adopted to replace the small strain whose expression is incomplete. Many researchers (Hibbitt et al., 1970;

Mcmeeking et al., 1975; Cater et al., 1977; Hu and Randolph, 1998; Sheng et al., 2008) made much attempt to implement the numerical analysis of pile by aid of finite element method involving large deformation. It is proved that soil particle will show negative dilatancy and lose its strength when crushing failure occurs.

1.2 Soil behavior and modeling

Soil mechanics along with all other branches of mechanics of solids requires the consideration of geometry or compatibility and of equilibrium or dynamics. The essential set of equations that differentiate the soil from other materials is the link relationship between stress and strain. It is noted that the behavior of soil is quite complicated. Therefore, we cannot hope that one single mathematic model can describe all the soil behavior. Even if such model is constructed, it will be too complex to serve as the master key for analysis of practical geotechnical problem. The purpose of the model is not to give a mirror image of reality, not to include all its elements in their exact sizes and proportions, but rather to single out and make available for intensive investigation those elements which are decisive (Muir wood, D., 1991).

Simplifications and idealizations are necessary for producing simper model that can describe those properties that essential to the considered problem, such as dilatancy or particle crushing. Thus, any such simpler model should not be expected to be valid over a wide range of conditions.

With the current state of computer programs, the simple but inadequate materials models frequently become the major factors in limiting the capacity and precision of stress analysis. This is especially true in soil mechanics where majorities of constitutive model are derived from triaxial state of stress which does not exist. Nevertheless, the new model is established from other starting points more close to true soil behavior to represent the link between stress and strain. All newly-constructed models have certain

inherent advantages and limitations depending to a large degree on their particular applications.

1.3 Motivation and objectives

Aiming to gain a thorough understanding of sand behavior in surrounding of pile tip under complex compressive and shear stress, the crushing behavior of sand are incorporated into the numerical analysis and the large deformation as well as interaction between the sand and pile are also taken into account.

The objectives of this study include:

1. Confirmation of the existence of particle crushing. It is recognized that sand particles will be crushed in the high compressive and shear stress distributed region such as pile tip. To deeply understand the existence of particle crushing and the crushing degree of different granular materials, a simple one dimensional compression test apparatus providing significant high compressive stress is proposed and applied to cause particles to be crushed. The loading condition of high compressive stress beneath pile tip is simulated by this test apparatus.
2. Implementation of the thorough numerical analysis of model pile loading in sand. To overcome the difficulties of material nonlinearities, the constitutive model for sand with particle crushing is applied to represent the behavior of the sand and the joint element is utilized to simulate the interactive region between sand ground and pile. In concerned with geometrical nonlinearities, the finite element analysis incorporating large deformation is accomplished. It initially introduces particle crushing model expressing stress-strain nonlinearity relation into the large deformation numerical analysis.
3. Apprehension of the bearing mechanics of pile loading in sand and visualization the compressive and dilative region of sand behavior around straight pile. Comparison of the predicted results from the small deformation and large deformation theory respectively.

4. Investigation on the effect of the pile tip shape on the behavior of sand in surrounding of pile tip. The distribution of stress and strain contours of sand around model pile with different pile tip shape are represented and compared.

1.4 Methodology

Numerical methods are very useful in geomechanics because they provide results with limited effort and highlight the most important variables that determine the solution of the problem. Soil may not be isotropic or homogeneous, and the loading condition may not be static, or the geometry of the problem may be complex. In these conditions, solution can only be obtained numerically. For soil, it is often assumed that a continuum approach is appropriate.

Finite element method is by far the continuum method most used in geomechanics. There are many books which deal with the application of numerical methods – usually FEM to engineering problems or to geotechnical problems in particular (Britto and Gunn., 1987; Cook et al., 1989; Cook, 1995; Livesley, 1983; Potts and Zdravkovic, 2001; Smith and Griffiths, 1988; Zienkiewicz and Talylor, 2000). The method relies on the assumption that, through appropriately chosen interpolation functions, displacement at any point within the element can be accurately obtained from the displacements of the nodes (Bobet, 2010). The method is based on the principle of virtual displacement. Under the condition of any small virtual displacements applied to the body, the total internal work associated with the virtual displacement field must be equal to the total virtual external work.

Generally，pile loading and penetration is often tackled as the axi-symmetric structure. The elastoplastic tensor for constitutive model and zero-thickness joint element are conducted for the axi-symmetric finite element analysis and complied by Fortran code.

1.5 Structure of the thesis

This dissertation represents the numerical analysis of the sand behavior around pile tip incorporating the large deformation theory and the constitutive model for sand with particle crushing.

The dissertation is organized as follows:

In chapter 2, the one dimensional high compression test on three kinds of granular materials is described. The crushing occurrence of granular materials is confirmed by grain size distribution before and after test. The crushing ability of three kinds of granular material is examined. The relationship between the external loading and the plastic work for three kinds of granular materials are obtained.

In chapter 3, the sand dilatancy prediction theory of constitutive model with particle crushing is explained. To integrate this constitutive model with the finite element analysis, the tensor for the elastoplastic constitutive model with particle crushing is derived.

In chapter 4, the large deformation theory and the joint element for solving pile loading in sand is reviewed. The geometrical and material nonlinearity matrixes for the axi-symmetric are obtained for finite element analysis.

In chapter 5, the confining effects of the model tank is presented at first. The numerical analysis of soil behavior in surrounding of pile tip in the scope of small strain is discussed. The soil behavior is represented by the constitutive model for sand with particle crushing. The predicted values by the small and large strain theory are compared with the test results and discussed.

In chapter 6, the influences of pile tip shape on the sand behavior around pile tip is investigated. The distribution of stress and strain contours in surrounding of pile tip. The volumetric change of soil particle in different depths beneath pile tip is represented.

In chapter 7, the discussions of the conclusions and further works are provided.

To summarize the framework of the dissertation is shown in the following flow chart.

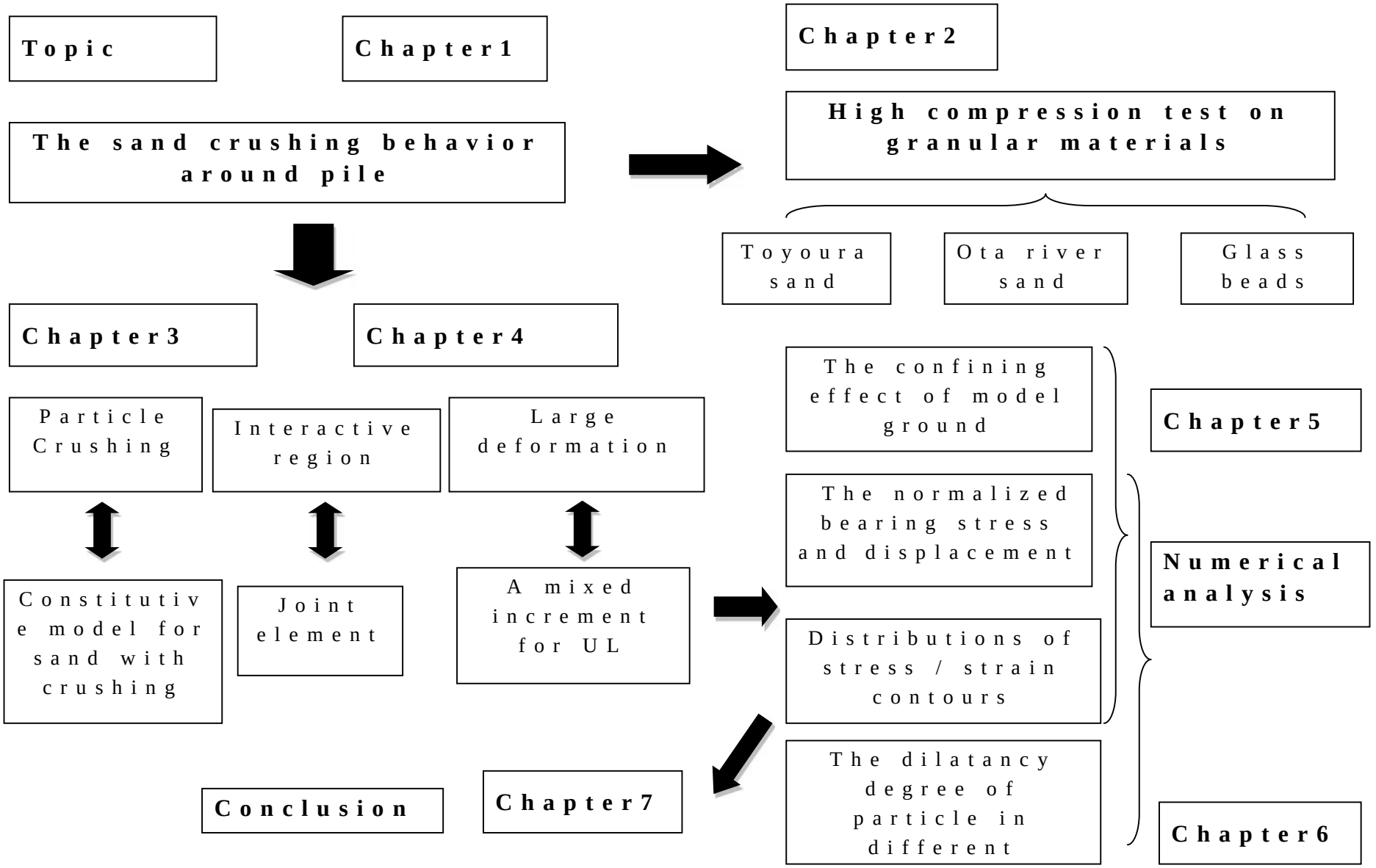
Topic
Chapter1
The sand crushing behavior around pile
Chapter2
High compression test on granular materials
Toyoura sand
Ota river sand
Glass beads
Chapter3
Chapter4
Particle Crushing
Interactive region
Large deformation
Constitutive model for sand with crushing
Joint element
A mixed increment for UL
The confining effect of model ground
Chapter5
The normalized bearing stress and displacement
Numerical analysis
Distributions of stress / strain contours
The dilatancy degree of particle in different
Chapter6
Conclusion
Chapter7

Reference

Bobet, A. (2010). “Numerical methods in geomechanics”. The Arabian journal for Science and Engineering, 35(1B), 27-48.

Britto, A. M. and Gunn, M. J. “Critical state soil mechanics via finite elements”. Chichester, Ellis Horwood, 1987.

Cater, J. P., Booker, J.R. and Davis, E. H. (1977) “Finite deformation of an elasto-plastic soil”. International Journal for Numerical and Analytical Methods in Geomechanics, 1, 25-43.

Cook, R.D., Malkus, D. S. and Plesha, M. E. “Concepts and applications of finite element analysis (3rd edition)”. New York, John Wiley, 1989.

Cook, R. D. “Finite element modeling for stress analysis”. New York, John Wiley, 1995.

Hibbitt, H. D., P. V. Marcal and Rice, J. R. (1970). “A finite element formulation for problems of large strain and large displacement”. International Journal of Solids and Structures, 6, 1069-1086.

Hu, Y. and Randolph, M. F. (1998). “A practical numerical approach for large deformation problems in soil”. International Journal for Numerical and Analytical Methods in Geomechanics, 22(5), 327-350.

Livesley, R. K. “Finite elements: an introduction for engineers”. Cambridge, Cambridge university press, 1983.

Mcmeeking, R. M. and Rice, J. R. (1975) “Finite element formulation for problems of large elastic-plastic deformtion”. International Journal of Solids and Structures, 11, 601-616.

Muir Wood, D. “Soil behavior and critical state soil mechanics”. Cambridge, Cambridge university press, 1991.

Potts, D.M. and Zdravkovic, L “Finite element analysis in geotechnical engineering: theory”. London, Thomas Telford, 1999.

Potts, D.M. and Zdravkovic, L “Finite element analysis in geotechnical engineering: application”.

London, Thomas Telford, 2001.

Poulos, H. G. (1989). “Pile behavior – Theory and application”. Geotechnique, 39(3), 365-415.

Poulos, H.G. (2005). “Pile behavior – Consequence of Geological and Construction Imperfections”. Journal of Geotechnical and Geoenvironmental Engineering, 131(5), 538-563.

Randolph, M.F. (2003). “Science and empiricism in pile foundation design”. Geotechnique, 53(3), 847-875.

Smith, I. M and Griffiths, D.V. “Programming the finite element method (2rd edition)”. Chichester, John Wiley, 1988.

Sheng, D. C., Nazem, M. and Carter, J. P. (2009). “Some computational aspects for solving deep penetration problems in geomechanics”. Computational Mechanics, 44(4), 549-561.

White, D.J. “An investigation into the behavior of pressed-in piles”. PhD dissertation, University of Cambridge, 2002.

Zienkiewicz, O.C. and Talylor, R.L. “The finite element method (5th edition)”. Butterworth-Heineman, Oxford, 2000.

CHAPTER 2

HIGH COMPRESSION TEST ON GRANULAR MATERIALS

2.1 Objective of the high compression test

Generally, sand is composed with the individual particles and regarded as the granular material. It is assumed that there is no cohesive stress among the granular particles. When sand particles are subject to the compressive or the shear stresses, the particles are liable to move another stable position and state. The particle stops to transmit and begins to be crushed once the outer force continues. It is well recognized that sand particle will be crushed when it is subject to significant complex stresses in many previous researches (Harbin, B.O., 1985; Lee and Seed, 1967; Marsal, E. J., 1967; Vesic and Clough; 1968). The positive dilatancy degree and strength of granular material will decrease once particle crushing occurs.

Particle crushing is negligible at very low confining pressures, its influence on the stress-strain and strength behavior increase with confining pressure and it becomes the dominant deformation mechanism at high confining pressures.

The study on the particle crushing has significant meaning in engineering practice such as the estimation of the bearing capacity of pile loading in sand. The mechanical behavior change of sand beneath pile tip is the typical problem to explain the particle crushing phenomena. To intensively understand the sand crushing behavior under high level compressive stress, an experimental study on particle crushing is conducted. A simple one dimensional high compression test is performed on different granular materials.

Many kinds of laboratory experiments were proposed to investigate sand crushing behavior under

high compression and shear stress. For example, the triaxial compression test, the one-dimension compression and the ring shear test are performed to understand the mechanical behavior change in the process of sand particle crushing. Moreover, one dimensional compression test is easy to conduct and is capable of simulating the stress loading condition in the region beneath pile tip. It is noted that the region beneath pile tip is heavily compressed but slightly sheared. Such stress condition can be simply simulated by the one dimension test. The vertical stress applied in test indicates the depth of the pile penetrated into the soil ground.

To understand the mechanical behavior and physical features of sand under high level stress, a simple devices providing high pressure is proposed to implement the high compression test on granular material. In this test, the granular material specimen is confined into a circular cylindrical. The vertical outer load is acted on the top surface of the specimen and the confining pressure increases with the vertical load increasing. The vertical pressure and horizontal confining pressure cannot be manipulated individually.

The failure pattern of particle crushing is dependent on the inherent structure and its composition. To confirm the particle crushing occurrence and observe the crushing failure patterns of different granular materials, high compression test on Toyoura sand, Ota river sand and glass beads are performed respectively. Besides, particle crushing is heavily affected by the presence or absence of water. In this study, all the specimen and experiment condition are absence of water.

Two methods are utilized to confirm the granular particle crushing occurrence. The first method is to observe the change of particle size and shape by high resolution digital microscope. Secondly, the grain size distribution curves of particle before and after test are compared.

Moreover, the relationships between the mean stress and volumetric strain, the deviatoric stress and

deviatoric strain of sand specimen are presented and analyzed. It is pointed by Yashima et al. (1987) that the energy consumption in accompany with the particles crushing and rearrangement. The energy input required to overcome the shear strength of sands has been found to consist of several components, including basic friction, dilation, and rearrangement and crushing of particles. To clarify the energy dissipation tendency with the outer force increasing, the relationship between the energy dissipation and the vertical stress acted on the specimen is shown.

2.2 Review of the experimental study on sand crushing

To investigate the influential factors of particle crushing, many high stress level tests have been performed. The amount of crushing that occurs in isotropic and K_o-compression as well as shear tests has been studied in several investigations. Recently, the attention has been paid to single particle crushing, both in numerical and experimental studies (Mcdowell and Bolton, 1998; Nakata et al., 1999, 2001a, 20101b; Bolton et al., 2008). The history of high level compressive or shear stress tests on sand is reviewed by the kinds of loading conditions method.

One dimensional test

Nakata et al. (2001a, 2001b) performed the one-dimensional compression test on silica sand and discussed the effects of initial grain size distribution on the compression characteristics. From the experimental results, the yield stress of sand in one dimensional compression test is related with the strength of single particle. Yamamuro et al. (1996b) developed a one-dimensional testing apparatus and tested soils with axial stresses up to 850 MPa. The time effect on the lateral coefficient was discussed

by Dejong and Christopg (2009) performed the one-dimensional test on Ottawa sand and explained the effects of particle crushing on the hydraulic conductivity.

Triaxial compression test

In triaxial compression test, the effects of shear stress on particle crushing can be examined. Miura and Yamamoto (1976) and Miura et al. (1984) carried out the triaxial compression test on Toyoura sand and described the yield curves of sand in particle crushing region. Miura and Yamanouchi (1975) performed the high pressure triaxial tests on the sand in both dry and saturated states. Fukumoto (1992) performed triaxial compression test and other kinds of compression test on sand and presented the particle comminution theory. Yamamuro and Lade (1996a), Lade and Yamamuro (1996) performed a lot of triaxial compression and extension test with drain and undrained conditions and proposed the particle breakage index B_{r10}. Mcdowell and Bolton (1998) presented a study of the micromechanical behavior of crushable soil and conducted the triaxial compression test on soils of equal relative density. Hyodo et al. (2002) implemented the high triaxial compression test on Aio sand and examined that the degree of sand crushing increases as the number of cyclic loading increasing under high compression.

Ring shear test

Particle crushing sometimes occurs under low compression and is heavily influenced by the shear stress level. Sadrekarimi and Olson (2010a, 2010b) performed the ring shear test and observed the process of shear localization and shear band formation and evolution. Arslan et al. (2009) performed the direct shear test on the manufactured granular material and discussed the effect of crushing on the bulk behavior of the granular materials.

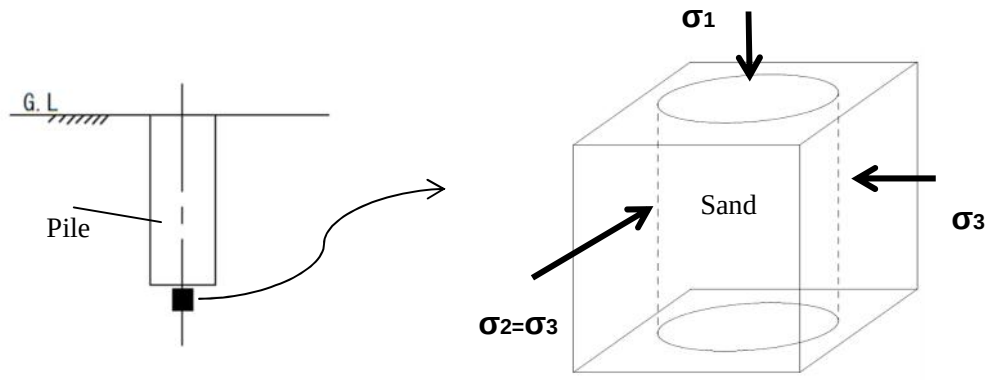

Figure 2.1 (a) The soil particle beneath pile tip (b) The stress state of high compression

2.3 Description of the test apparatus

In laboratory and outdoor experiment, it is observed that sand particles beneath pile tip are liable to be crushed. To simply represent the actual high level compression state beneath the pile tip in Figure 2.1 (a), a simple one dimension compression test is proposed to simulate the heavily compressive state just as beneath the pile tip. To satisfy the axi-symmetric condition like pile, the sand specimen in one dimensional test is made as the cylinder specimen. The vertical force is acted on the specimen by outer loading, while the confining stress is provided by the reaction of the steel container apparatus in Figure 2.1 (b). It is assumed that the larger the outer vertical loading is, the deeper the pile is penetrated into the sand ground. The circumferential stress is consistently equal to the radial stress during the loading.

2.3.1 Details of test apparatus

The test apparatus is composed of two similar half-container parts in Figure 2.2. These two parts are connected and fixed by four steel bars. The granular material for test is poured into the cylinder

specimen layer by layer. The circular head and base pedestals are placed at the top and the bottom of the specimen. The deformation of granular materials exits only in vertical direction and the horizontal and circumferential deformations are not permitted. Owing to the frictional stress on the interactive zone between the granular material and steel container, the vertical loading can't transmit to the bottom completely. Teflon sheets and silicon-grease are pasted on the interface between the ground tank container and Toyoura sand to eliminate the effect of fictional stress. To know the value of frictional stress, two load cells are installed on the top surface and bottom surface to measure the vertical force respectively.

Two displacement gages are adopted to measure the decrement of the sand specimen. Another two displacement gages are installed to record the expansive displacement of test apparatus in radial direction. Eight strain gages have been pasted on the four steel bars to measure the normal strain of steel bar. The front view of the high-compression test apparatus are shown in Figure 2.3 (a) and (b).

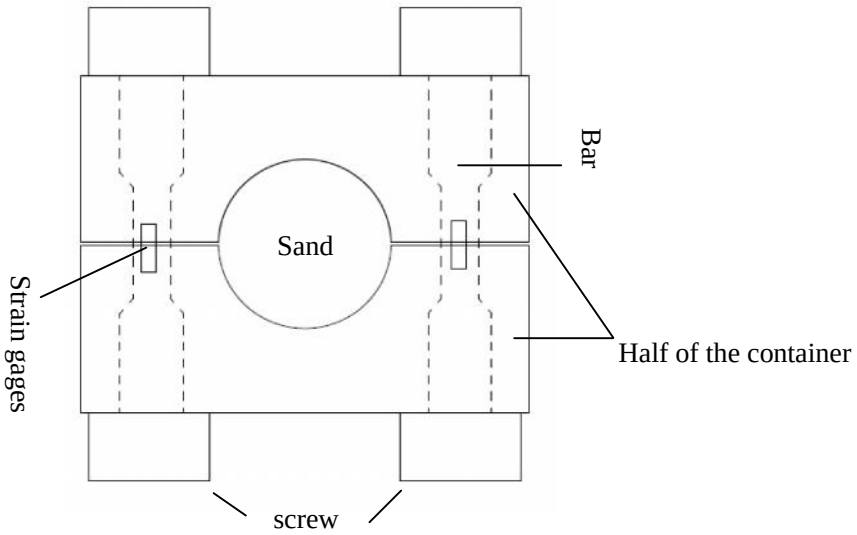

Figure 2.2 View of the top surface of one dimensional high-compression test apparatus

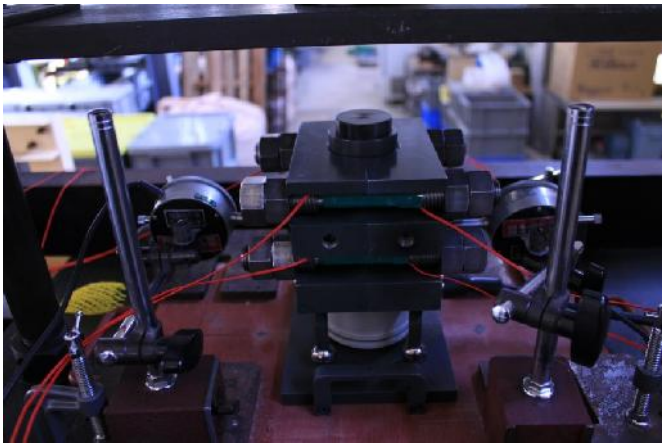

Figure 2.3 (a) Back view of the one dimensional high-compression test apparatus

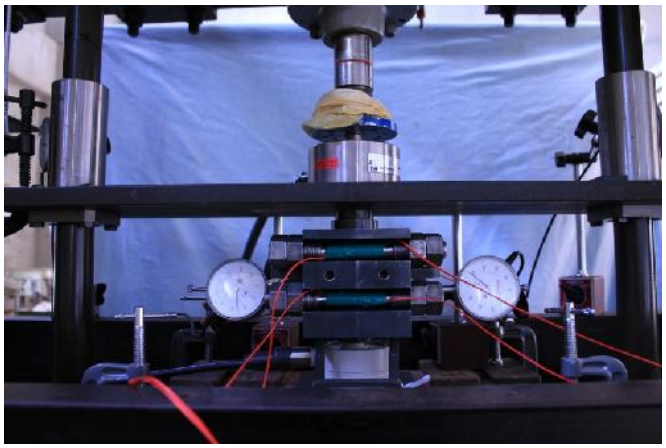

Figure 2.3 (b) Front view of the one dimensional high-compression test apparatus

The vertical stress $\pm_h$ and vertical strain $£_h$ are obtained as in Eq. (2.1) and Eq. (2.2). The total force acted on test apparatus in radial direction is the summation of the forces on the four steel bars. The radial force on the steel bar can be calculated with the aid of the elastic modulus of steel bar. The total force on test apparatus in radial direction is equal to that on sand specimen in the same direction. Therefore, the radial stress is obtained from Eq. (2.3).

The circumferential stress and circumferential strain are equal to the component in radial direction.

Therefore, all the six stress and strain quantities can be determined once the outer loading is applied on.

$$\pm_h = \frac{T}{A} \tag{2.1}$$

Where, T is the vertical loading, A is the area of the specimen in test.

$$£_h = \frac{¢}{H} \tag{2.2}$$

Where, $¢$ is the decrement of specimen, H is the height of the specimen.

$$\pm_r = \frac{(\pm_{*1} + \pm_{*2} + \pm_{*3} + \pm_{*4})a_*}{HD} \tag{2.3}$$

Where, $\pm_{*1}$, $\pm_{*2}$, $\pm_{*3}$ and $\pm_{*4}$ are the normal stress of the four steel bars. a_* is the area of steel bar. D is the diameter of specimen.

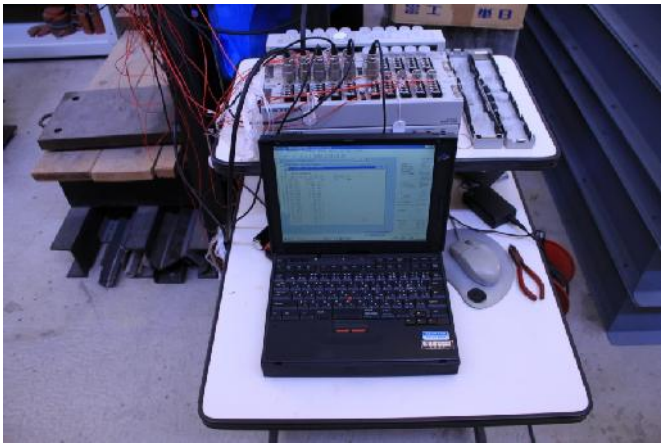

Figure 2.4 The computer for recording experimental data

2.3.2 The data record equipment

All the experimental results are recorded by the computer in Figure 2.4. The largest capacity of loading apparatus is 5.0 tf. Therefore, the maximum vertical loading on the sand specimen varies from 0.0 tf, 0.6 tf, 1.5 tf, 3.0 tf, 4.0 tf to 5.0 tf. The vertical loading, vertical displacement and horizontal displacement are correspondingly measured for each test.

2.3.3 Three kinds of granular material

To differentiate the particle crushing pattern of granular material, two kinds of natural sand and one kind of artificial sand are adopted in test. The properties of the three granular materials are shown in Table 2.1. The specimen is densely prepared with relative density as 90%. The sand is poured into cylinder specimen in the apparatus by ten layers, densely compacted each time.

(a) Toyoura sand

Toyoura sand is the standard sand for the Japanese Geotechnical Society. Toyoura sand in Figure 2.5

Table 2.1 Physical properties of the granular materials

	Specific Gravity (g/cm^3)	Maximum particle size D*max* (mm)	50% particle size (mm)	Maximum density ρ_{max}	Minimum density ρ_{min}
Toyoura sand	2.656	1.50	0.25	1.646	1.332
Ota river sand	2.648	2.92	0.66	1.641	1.347
Glass beads	2.595	0.72	0.60	1.608	1.428

Figure 2.5 (a) Toyoura sand

(a) is one kind of silica sand widely used in research and laboratory test. The chemical composition of Toyoura sand includes SiO_2, Al_2O_3, Fe_2O_3, CaO etc. The distribution range for Toyoura sand diameter is narrow. The mean diameter of Toyoura sand is relative fine.

(b) Ota river sand (Masado)

Masado is widespread in the western part of Japan. The properties of Masado vary in the different distributed region. The sample in Figure 2.5 (b) for test is taken from the Ota river, located in the northwest of Hiroshima prefecture. The distribution range for Ota river sand diameter is quite wide.

Figure 2.5 (b) Ota river sand

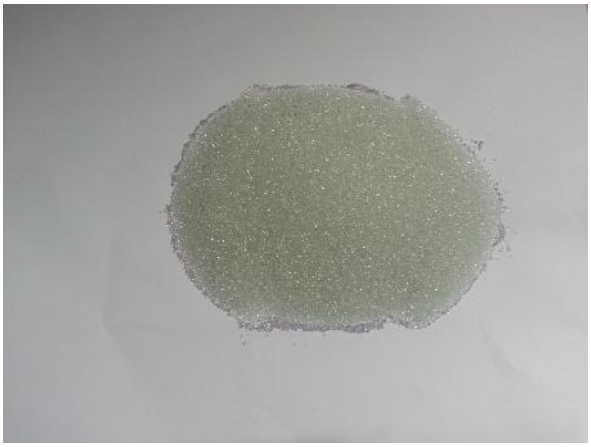

Figure 2.5 (c) Glass beads

(c) Glass beads

Glass beads shown in Figure 2.5 (c) are not the natural sand, but a artificial sand. Glass beads are composed with an amount of the same size glass balls. The ball is brittle material and display different failure pattern compared to natural sand. The mean diameter for all glass balls is 0.6 mm in this test.

2.4 Occurrence confirmation of particle crushing

The mean diameter of Toyoura sand is relative small, the mean diameter of glass beads is medium and the mean diameter of Ota river sand is large. The sieving tests for these three kinds of granular materials are performed before and after loading test as shown in Figure 2.6.

2.4.1 Grain size distribution before and after high compression test

To confirm the occurrence of particle crushing, grain size distribution for Toyoura sand, Ota river sand and glass beads before and after one dimensional high compression test are shown in Figure 2.7,

Figure 2.6 The scene for sieving test

Figure 2.8 and Figure 2.9. In each figure, sub-title (a) means the curves for the whole analysis region, while sub-title (b) is the enlarged portion of figure (a) to clearly understand the change of grain size distribution curves.

Figure 2.7 shows the grain size distribution of Toyoura sand. The vertical axis is from zero to 50 percent and the horizontal axis, diameter size for the particle, varies from 0.06 mm to 0.6 mm in Figure 2.7 (a). It is noticed that the diameter indicates 0.11 mm when the percent is 50 % from the grain size distribution curves. Moreover, three curves are drawn at the state of vertical loading as 0 MPa, 10.01 MPa and 16.67 MPa. It is observed that the mean particle diameter size become finer as vertical loading increases for three kinds of granular materials. In Figure 2.7 (a), the grain size distribution moves to left and up direction as vertical loading increases. The differences among the three curves become clear when the mean diameter is less than 0.08 mm. It is observed that the volume of sand particle with mean diameter less than 0.07 mm increases almost two times.

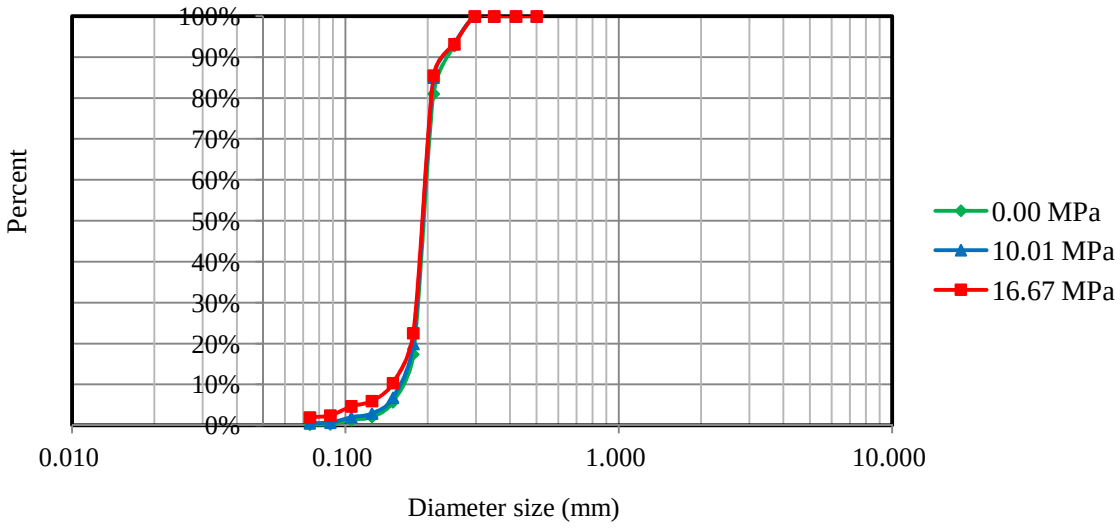

(a)

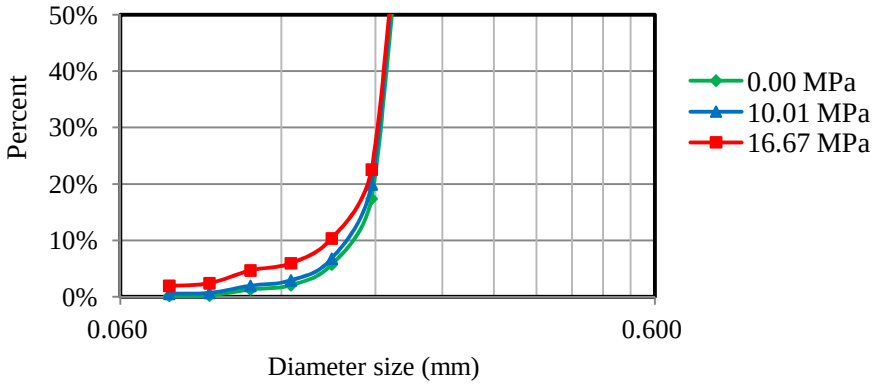

(b)

Figure 2.7 The grain size distribution of Toyoura sand under different vertical loading levels

In Figure 2.8 (a), range for the diameter size distribution of Ota river sand is wide. It is noticed that the diameter indicates 0.7 mm when the percent is 50 % from the grain size distribution curves. From comparing the curves in initial and final state, the phenomena of particle crushing for Ota river sand is quite obvious. From the Figure 2.8 (b), the mount of Ota river sand passing 0.1 mm increases nearly three times. It is concluded that the crushing ability of Ota river sand is higher than Toyoura sand and glass beads.

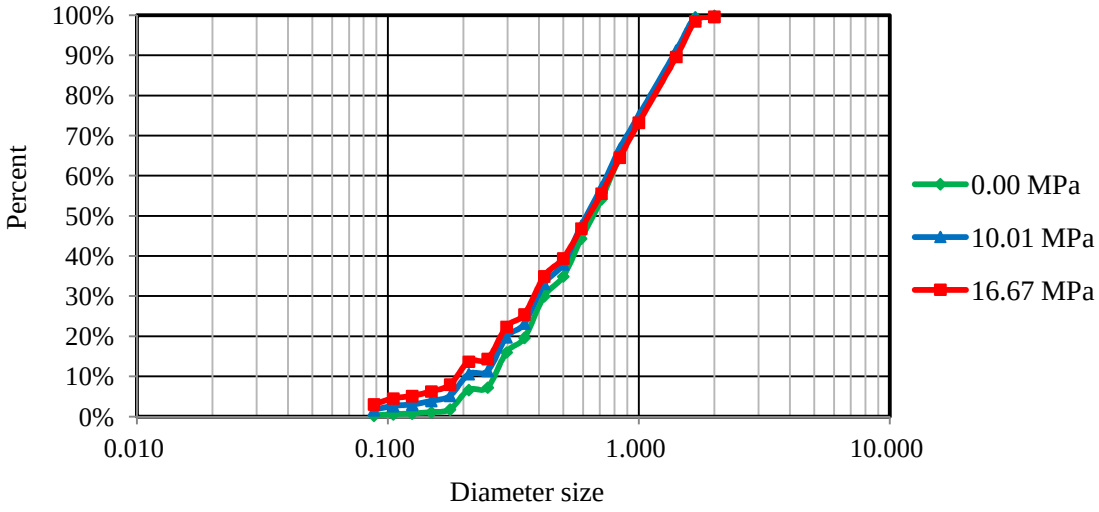

(a)

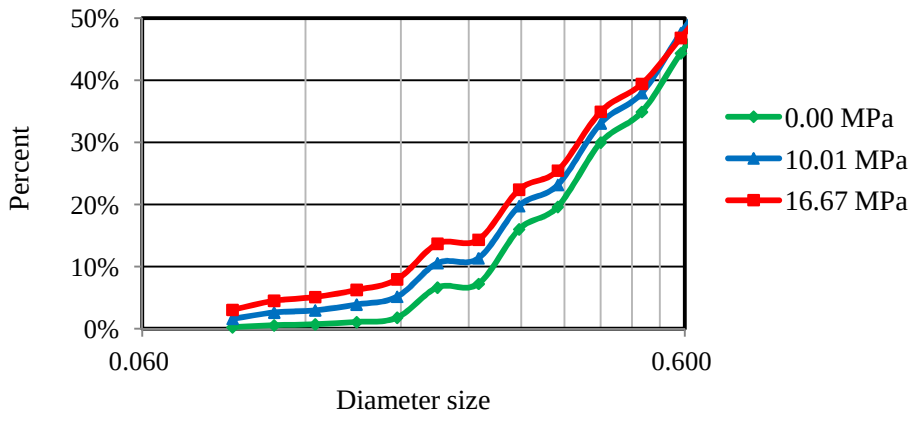

(b)

Figure 2.8 The grain size distribution of Ota river sand under different vertical loading levels

In Figure 2.9 (a), it represents that the particle diameter is mainly around the 0.6 mm. The three curves slightly change for different vertical loading. In Figure 2.9 (b), it is understandable that the glass beads become finer as vertical loading becomes large. The less difference among three diameter size distribution curves is attributed to the crushing patter of the glass beads. It will be explained in next.

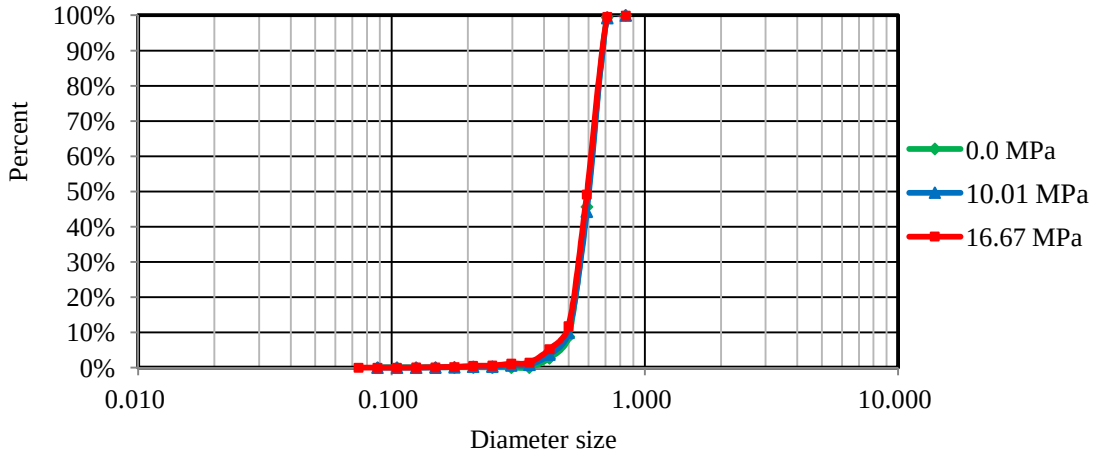

(a)

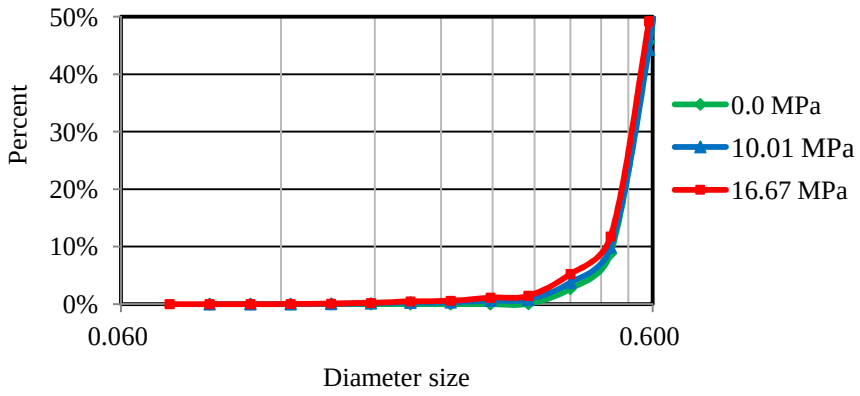

(b)

Figure 2.9 The grain size distribution of glass beads under different vertical loading levels

The grain size distribution curves for three granular materials at initial and final state during the one dimensional compression test are compared in Figure 2.7, Figure 2.8 and Figure 2.9. It is found that the change of the grain size distribution is not remarkable for Toyoura sand and glass beads. Except the reason for the composition of these two granular materials, it is attributed to that the particle crushing mainly comes from the compressive stress in one dimensional test. Shear stress also plays significant role in particle crushing under complex stresses.

2.4. 2 The particle size observation

Owing to the level of diameter size is minuteness; it can only observe the particle with the help of the digital microscope as shown in Figure 2.10. The digital microscope can measure the diameter of sand particle, amplified by two hundred times at most. For observation, the particles are taken from the specimen after the high compression test completion for each vertical loading level. The observation figures of the particle size level for Toyoura sand, Ota river sand and glass beads are displayed in Figure 2.11, Figure 2.12 and Figure 2.13. To under the change of particle diameter with increasing vertical loading, the observation figures show the state of particle diameter at vertical loading 0.0 tf (0.00 MPa), 0.3 tf (1.00 MPa), 3.0 tf (10.01 MPa)and 5tf (16.67 MPa) are shown in figure (a), (b), (c) and (d). In Figure 2.11 (a), it is found that the particle diameter for Toyoura sand is uniformity. The Figures 2.11 (b), (c) and (d) represent that the particle crushing becomes serves as vertical loading increases. Almost all the large particles are compressed to be crushed. The crushing failure is well displayed by the figures. It is noted that Toyoura sand transforms to small pieces in the process of crushing failure.

It is shown that the diameters of Ota river sand show quite different in Figure 2.12 (a). The diameter of some particle is very large. The occurrence of particle crushing is obviously displayed in Figure 2.12 (c). Ota river sand becomes much finer in Figure 2.12 (d) when the maximum vertical loading acting on. However, there still exits some large diameters particle compared with the case of Toyoura sand. The pattern of particle crushing for Ota river is similar to Toyoura sand.

The comparisons of particle crushing degree for glass beads can be obtained in Figure 2.13. Glass beads is regarded as one kind of reasonable soil. The crushing of glass beads is shown in Figure 2.13 (d). The crushing pattern for the glass beads is different from the natural soil. The glass beads breaks into

relative large part if the outer force overcomes its resistance. However, the maximum vertical loading is not large enough to cause the glass beads much smaller. The degree of particle crushing for glass beads is not quite remarkable as Toyoura sand and Ota river sand.

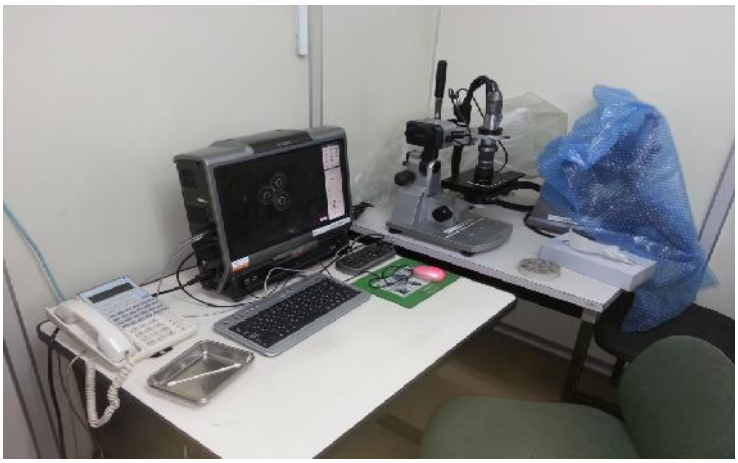

Figure 2.10 The digital microscope

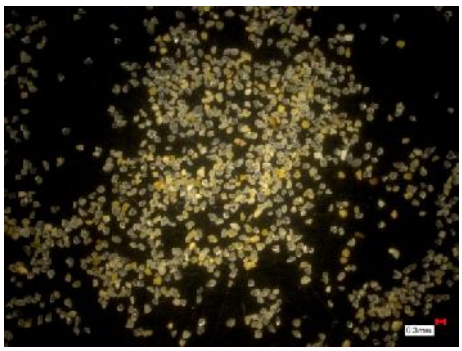

(a) 0.0 tf (0.00 MPa)

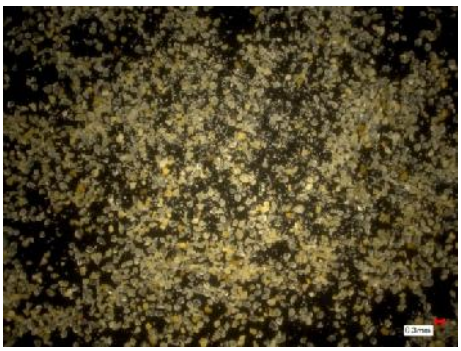

(b) 0.3 tf (1.00 MPa)

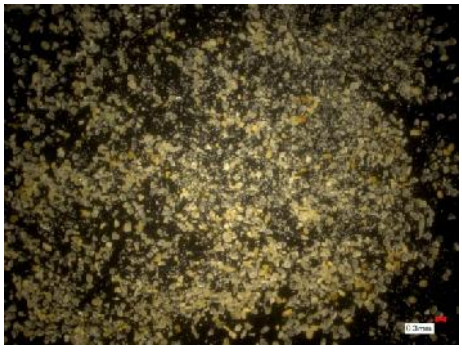

(c) 3.0 tf (10.01 MPa)

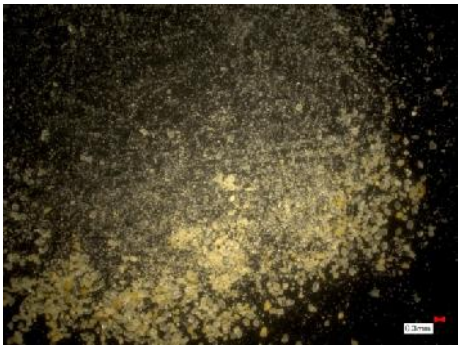

(d) 5.0 tf (16.67 MPa)

Figure 2.11 Crushing confirmation of Toyoura sand

(a) 0.0 tf (0.00 MPa)

(b) 0.3 tf (1.00 MPa)

(c) 3.0 tf (10.01 MPa)

(d) 5.0 tf (16.67 MPa)

Figure 2.12 Crushing confirmation of Ota river sand

(a) 0.0 tf (0.00 MPa)

(b) 0.3 tf (1.00 MPa)

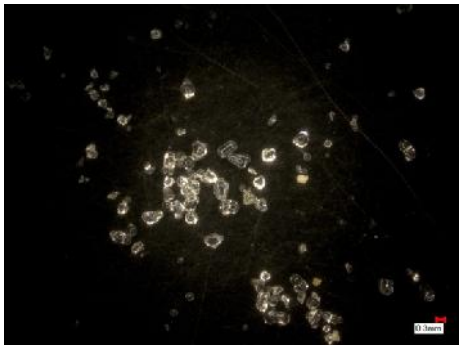

(c) 3.0 tf (10.01 MPa)

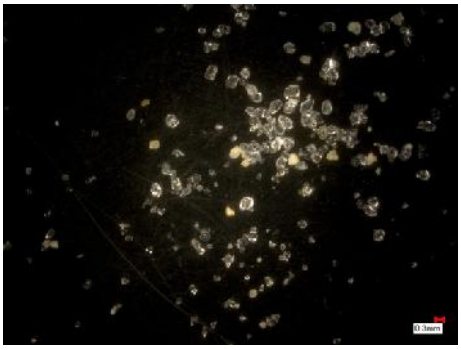

(d) 5.0 tf (16.67 MPa)

Figure 2.13 Crushing confirmation of glass beads

2.5 The results for the high compression test

To better understand and analyze the mechanical behavior of sand crushing before and after particle crushing process, the relationships among the mean stress, volumetric stress, deviatoric stress, deviatoric strain and plastic work are respectively investigated for three kind of granular materials. The crushability ability of each granular material is understandable. The subtitle (a), (b), (c) and (d) in each figure mean the vertical loading as 1.00 MPa, 5.01 MPa, 10.01 MPa and 16.67 MPa.

2.5.1 The relationship between the mean stress (p) and volumetric strain (ε_v)

The relationship between the mean stress and volumetric strain for Toyoura sand, Ota river and glass beads are displayed in Figure 2.14, Figure 2.15 and Figure 2.16 respectively. Here, the mean stress is the summation of vertical stress, radial stress and circumstance stress. The volumetric strain is the summation of vertical strain, radial strain and circumstance strain. It is exhibited that the curves under the four vertical loading levels shows the same pattern. The figures represent that the volumetric strain increase as the mean stress enhances for all three materials. The curves of the same material under different vertical loading express the same tendency in each figure group. For the same level of mean stress, the volumetric strain for Ota river sand is large than those of Toyoura sand and glass beads. It is represented that the maximum volumetric strain for Ota river sand in Figure 2.15 is almost three times of that for glass beads in Figure 2.16 and one and a half time for Toyoura sand in Figure 2.14. Therefore, it is concluded that the crushing ability of Ota river is high that the other two materials. From the analysis, glass beads is the most hardest to be crushed.

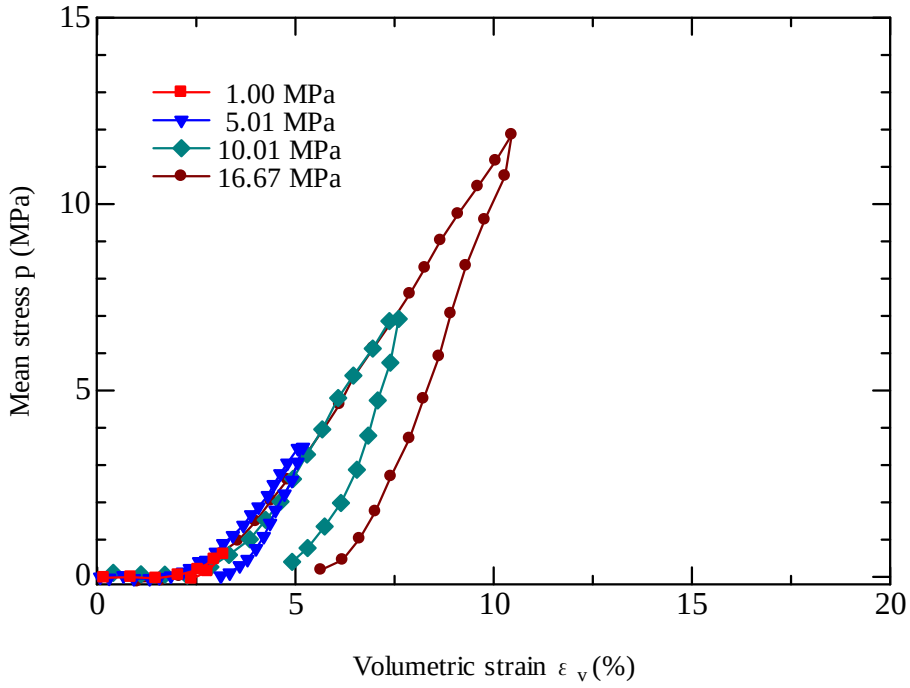

Figure 2.14 The relationship between the mean stress and the volumetric strain (Toyoura sand)

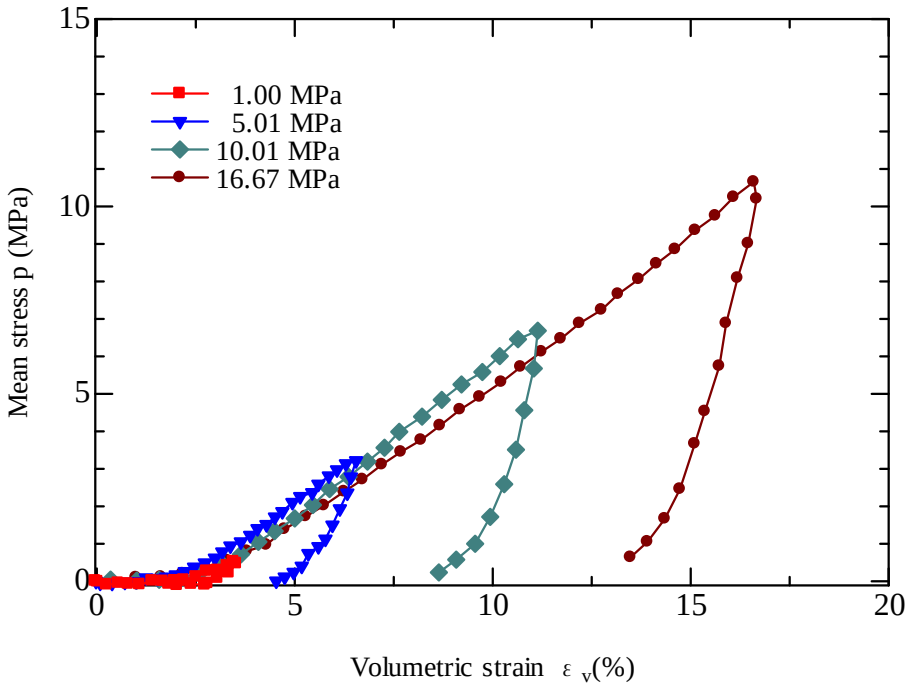

Figure 2.15 The relationship between the mean stress and the volumetric strain (Ota river sand)

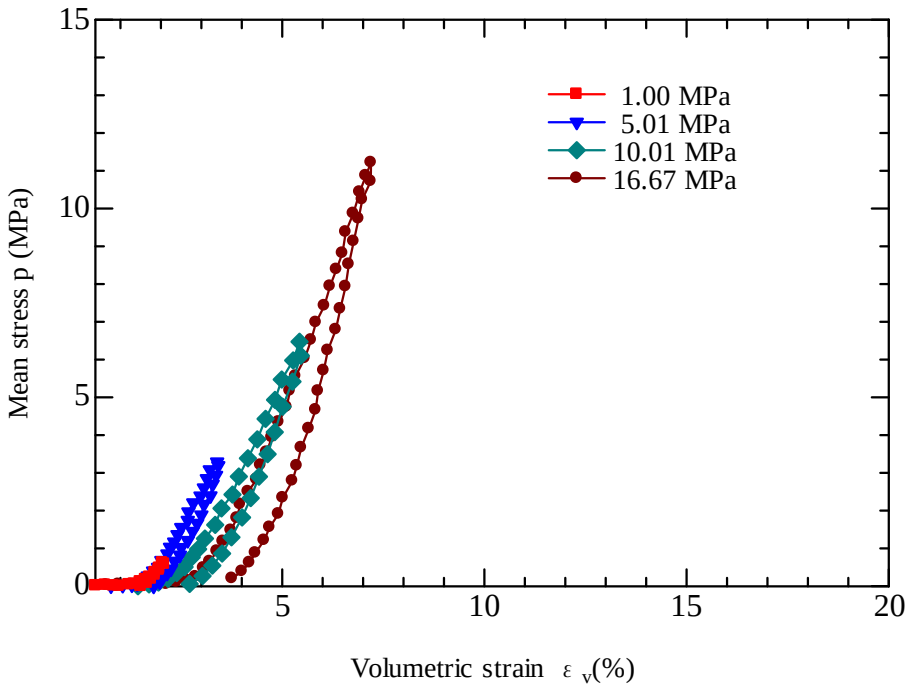

Figure 2.16 The relationship between the mean stress and the volumetric strain (Glass beads)

2.5.2 The relationship between the deviatoric stress (q) and deviatoric strain(ε_d)

The relationship between the deviatoric stress and deviatoric strain for Toyoura sand, Ota river sand and glass beads are displayed in Figure 2.17, Figure 2.18 and Figure 2.19 respectively. For the same level of deviatoric stress, the volumetric strain for Ota river sand is almost three times of that for glass beads and one and a half time for Toyoura sand. The relationship curves between the deviatoric stress and deviatoric strain express the same tendency to that between the mean stress and volumetric strain. The relationship curves of glass beads in Figure 2.18 under different vertical loading shows slightly different patterns.

Meanwhile, the maximum deviatoric stress reaches 16 MPa, higher that the mean stress 10 MPa. Because the limitations of high compression test loading condition, the vertical stress and horizontal

confining stress cannot be manipulated independently.

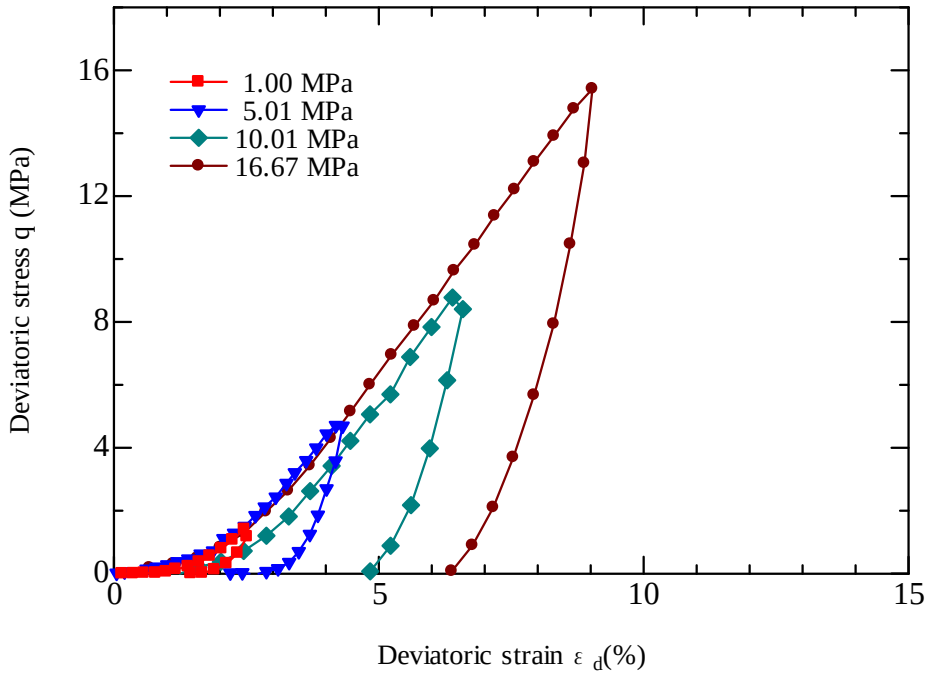

Figure 2.17 The relationship between the deviatoric stress and the deviatoric strain (Toyoura sand)

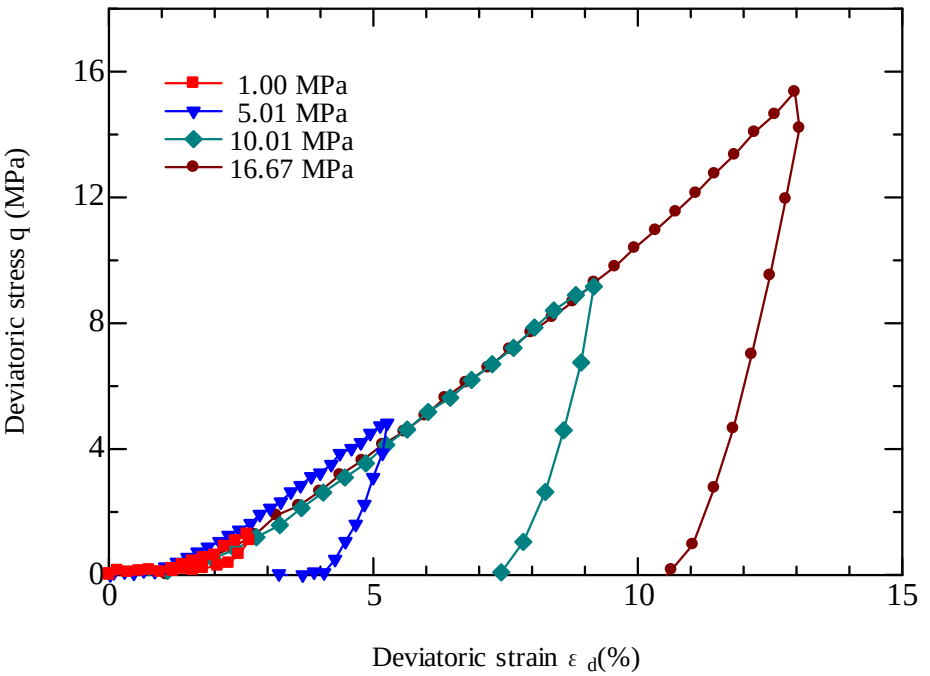

Figure 2.18 The relationship between the deviatoric stress and the deviatoric strain (Ota river sand)

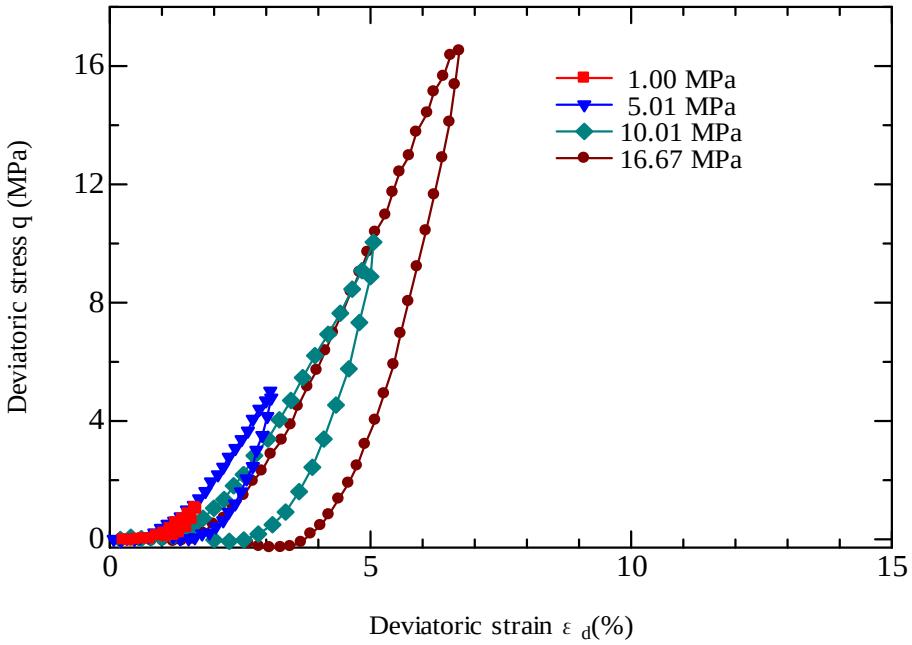

Figure 2.19 The relationship between the deviatoric stress and the deviatoric strain (Glass beads)

2.5.3 The ratio of deviatoric stress (q) to the mean stress (p)

The relationship between the deviatoric stress and mean stress for Toyoura sand, Ota river sand and glass beads are displayed in Figure 2.20, Figure 2.21 and Figure 2.22 respectively. Because the limitations of high compression test loading condition, the vertical stress and horizontal confining stress cannot be manipulated independently. The high compression test is conducted by four loading levels. In theoretical, the relationship between the deviatoric stress q and mean stress p should be linear. The experimental results are compatible with the assumption for the three granular materials. Herein, the coefficient K_o is defined as the ratio of radial stress and the axial stress in this one dimensional compression test in Eq. (2.4).

$$K_o = \frac{\pm_r}{\pm_a} \tag{2.4}$$

The ratio of the deviatoric stress *q* in Eq. (2.5) and the mean stress *p* in Eq. (2.6) ranges from 1.25 to 1.55 in Figure 2.20, Figure 2.21 and Figure 2.22. The ratio of deviatoric stress *q* and the mean stress *p* for glass beads is slightly larger than those of Toyoura sand and Ota river sand.

$$q = \pm_a - \pm_r \tag{2.5}$$

$$p = (\pm_a + 2\pm_r)/3 \tag{2.6}$$

where , σ_a is the axial stress and σ_r is the radial stress.

The stress ratio for Toyoura sand display slight difference at different loading level in Figure 2.20. The stress ratios for Ota river sand and Glass beads show the same value at different loading level in Figure 2.21 and Figure 2.22.

The stress ratio of deviatoric stress *q* by the mean stress *p* is written as in Eq. (2.7),

$$\frac{q}{p} = \frac{3(\sigma_a - \sigma_r)}{\sigma_a + 2\sigma_r} \tag{2.7}$$

When the minimum value of stress ratio $(q/p)_{min}$ is 1.25, the maximum value for K_o is 0.318. In contrast, the minimum value for K_o is 0.238 when the maximum value of stress ratio $(q/p)_{max}$ is 1.55. The K_o value is determined as 0.3 in this one dimensional compression test.

This one dimensional high compression test is also called K_o high compression test because that the radial stress and axial stress increase in proportional incremental value without lateral deformation.

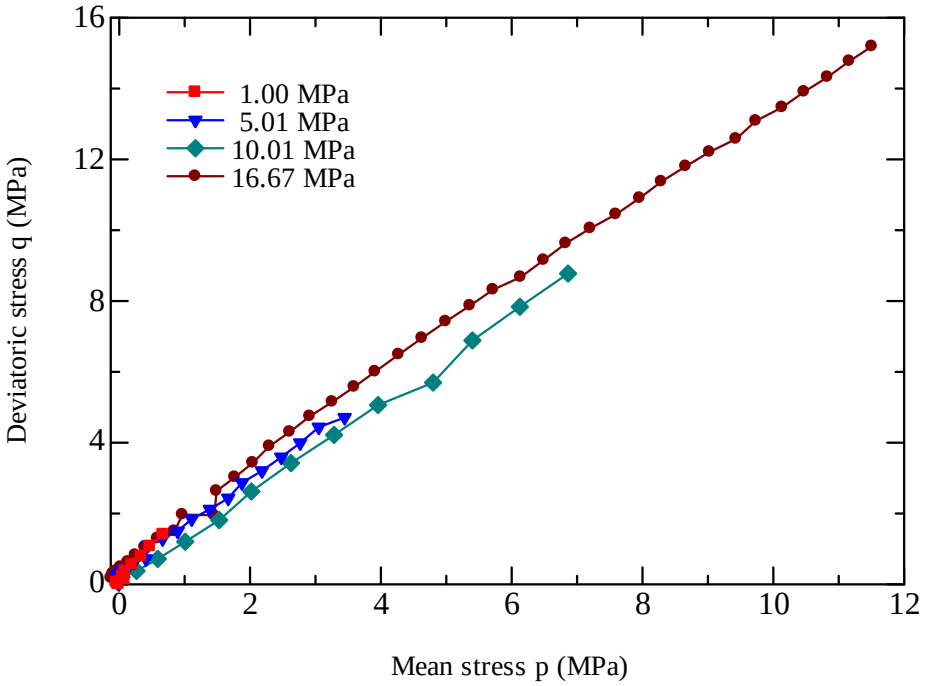

Figure 2.20 The relationship between the deviatoric stress and the mean stress (Toyoura sand)

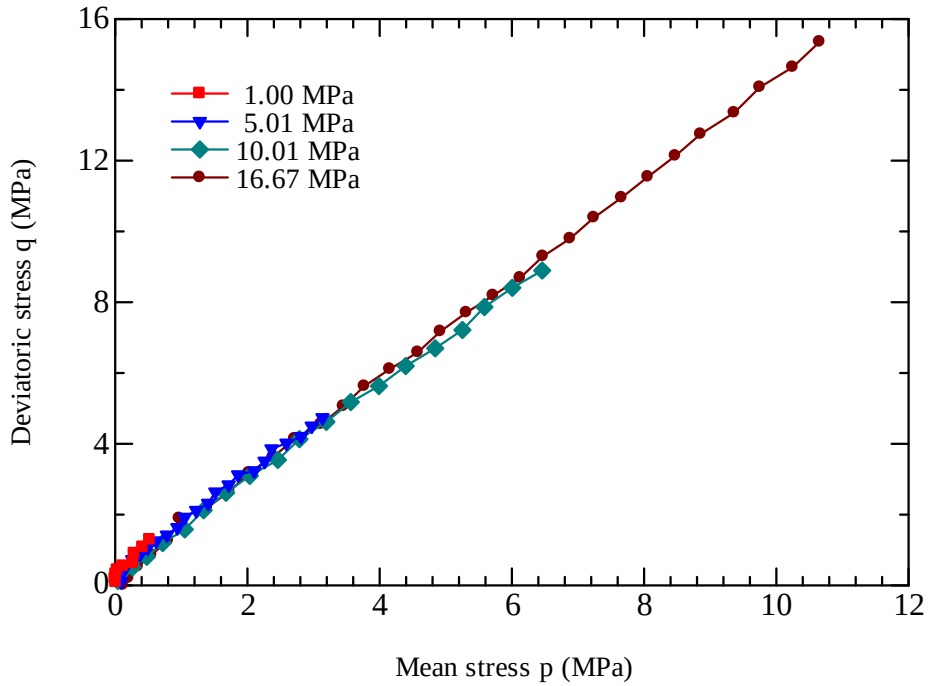

Figure 2.21 The relationship between the deviatoric stress and the mean stress (Ota river sand)

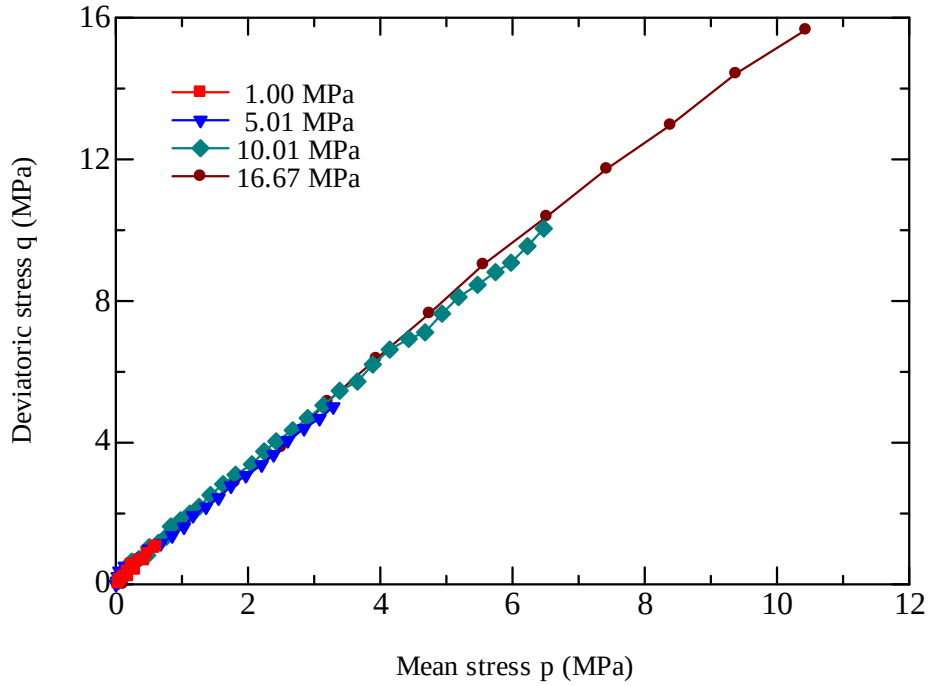

Figure 2.22 The relationship between the deviatoric stress and the mean stress (Glass beads)

2.5.4 The plastic work and vertical stress

The relationship between the plastic work per unit volume and vertical stress for Toyoura sand, Ota river sand and Glass beads are displayed in Figure 2.23, Figure 2.24 and Figure 2.25 respectively.

The occurrence of the plastic work accompany with the particle crushing in interior granular particle of the specimen. The consumption of the plastic work increases as the vertical stress increases. The figures show that the demand of plastic work for the Ota river sand is large than the other two granular materials under the same vertical stress level. The plastic work for the crushing of glass beads is minimum and almost half of that for Ota river sand.

From the analysis, it is concluded that the higher crushing ability the granular material owns, the more plastic work is needed for the particle being crushed.

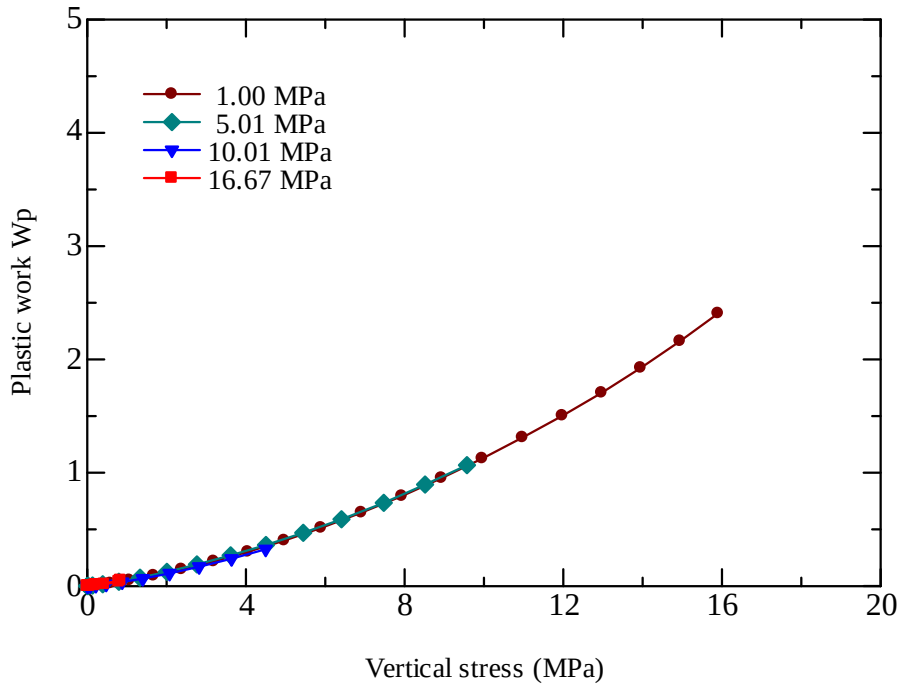

Figure 2.23 The relationship between the plastic work and the vertical stress (Toyoura sand)

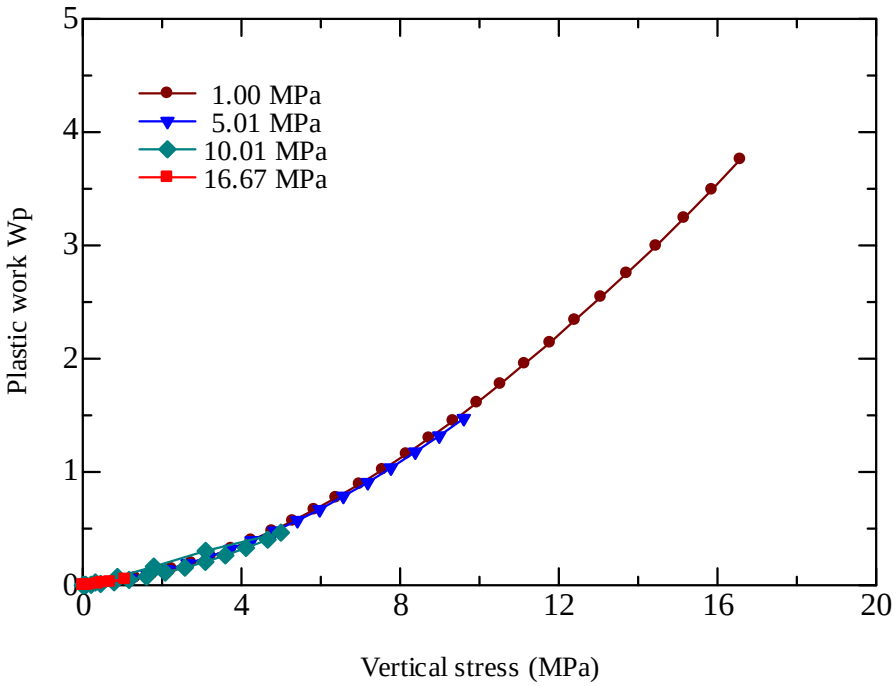

Figure 2.24 The relationship between the plastic work and the vertical stress (Ota river sand)

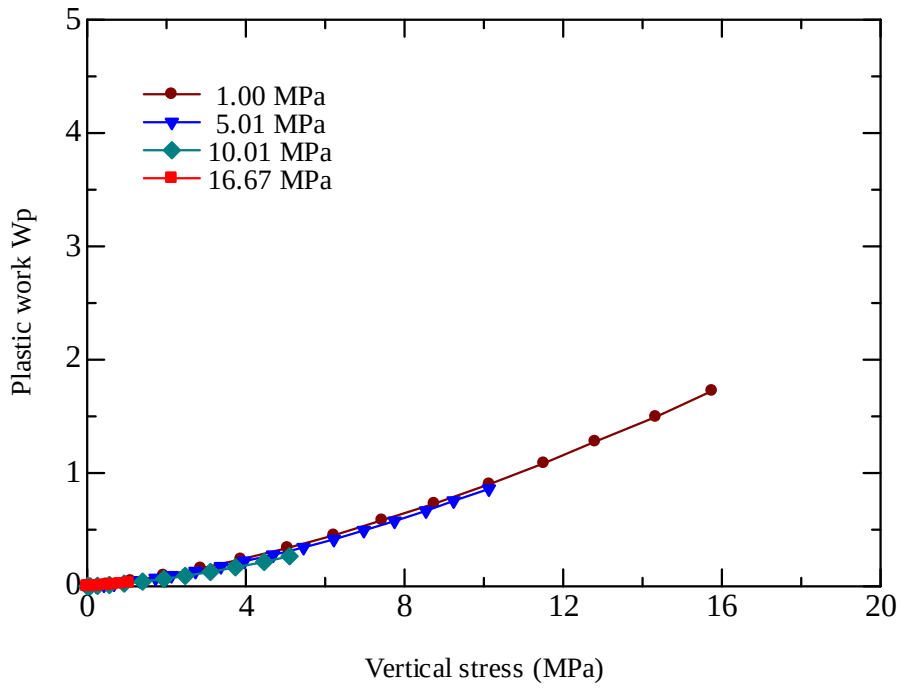

Figure 2.25 The relationship between the plastic work and the vertical stress (Glass beads)

2.6 Summary

1. A simple one dimensional high compression test apparatus is proposed. The one dimensional high compression test on three kinds of granular materials is performed. The occurrence of particle crushing is confirmed by two methods. One is to draw the grain size distribution curves before and after loading test. The curves move into left and up direction after test. The other is to observe the particle size by digital microscope. The particle becomes finer after high compression test.
2. From the comparison of the relationship between mean stress and volumetric strain for three kinds of granular materials. Under the same level of mean stress, it is found that the volumetric strain for Ota river sand is large than those of Toyoura sand and glass beads. Therefore, the crushing ability of Ota river sand is high. The glass beads is most difficult to be crushed.

3. In this one dimensional compression test, the radial stress increases as the outer vertical stress enhances. The ratio of deviatoric stress and mean stress keeps constant during the entire loading test. The value of coefficient K_o is determined as 0.3 in this high compression test.
4. The occurrence of the particle crushing accompany with the plastic work in interior granular particle of the specimen. From the relationship between the plastic work and vertical stress acting on the top surface of specimen are obtained for three kinds of granular materials. The results represent that more plastic work is needed for particle being crushed as the higher crushing ability the granular material owns.

Reference

Arslan, H., Baykal, G. and Sture, S. (2009). “Analysis of the influence of crushing on the behavior of granular materials under shear”. Granular Matter, 11(2), 87-97.

Bolton, M.D., Nakata, Y. and Cheng, Y.P. (2008). “Micro-and Macro-mechanical behavior of DEM crushable materials”. Geotechnique, 58(6), 471-480.

DeJong, J. and Christoph, G. (2009). “Influence of Particle Properties and Initial Specimen State on One-Dimensional Compression and Hydraulic Conductivity”. Journal of Geotechnical and Geoenvironmental Engineering, 135(3), 449–454.

Fukumoto, T. (1992). “Particle breakage characteristics of granular soils”. Soils and Foundations, 32(1), 26-40.

Hardin, B.O. (1985). “Crushing of soil particles”. Journal of Geotechnical Engineering, 111(10), 1177-1192.

Hyodo M., Hyde A.F.L., Aramaki N., Nakata Y. (2002). “Undrained monotonic and cyclic shear behaviour of sand under low and high confining stresses”, Soils and Foundations, 42(3), 63-76.

Lade, P. and Yamamuro, J. (1996). “Undrained Sand Behavior in Axisymmetric Tests at High Pressures”. Journal of Geotechnical Engineering, 122(2), 120–129.

Lee, K. L. and Seed, H. B. (1967). “Compressibility and Crushing of granular soil”. Canadian Geotechnical Journal, 4(1), 68-86.

Marsal, R. J. (1967). “Large scale Testing of Rockfill Materials”. Journal of soil mechanics and Foundation Division, ASCE, 93(SM2), 27-43.

Mcdowell, G. R. and Bolton, M.D. (1998). “On the micromechanics of crushable aggregates”.

Geotechnique, 48(5), 667-679.

Miura, N. and Yamanouchi, T. (1975). “Effect of water on the behavior of a quartz-rich sand under high stresses”. Soils and Foundations, 15(4), 23-34.

Miura, N. and Yamamoto, T. (1976). “Particle-crushing Properties of Sands under High Stresses”. Technology reports of the Yamaguchi University, 1(4), 439-447.

Miura, N., Murata, H. and Yasufuku, N. (1984). “Stress- strain characteristics of sand in a particle-crushing region”. Soils and Foundations, 24(1), 77-89.

Nakata, Y., Hyde, A.F.L., Hyodo, M. and Murata, H. (1999). “A probabllistic approach to sand particle crushing in the triaxial test”. Geotechnique, 49(5), 567-583.

Nakata, Y., Hyodo, M., Hyde, A.F.L., Kato, Y. and Murata, H. (2011a). “Microscopic particle crushing of sand subjected to high pressure one- dimensional compression”. Soils and Foundations, 41(1), 62-82.

Nakata, Y., Kato, Y., Hyodo, M., Hyde, A. F.L. and Murata, H. (2011b). “One-dimensional compression behavior of uniformly graded sand related to single particle crushing streength”. Soils and Foundations, 41(2), 39-51.

Sadrekarimi, A. and Olson S. M. (2010a). “Shear band formation observed in ring shear tests on Sandy Soils”. Journal of Geotechnical and Geoenvironmental Engineering, 136(2), 366-375.

Sadrekarimi, A. and Olson S. M. (2010b). “Particle damage observed in ring shear tests on sands”. Canadian Geotechnical Journal, 47(5), 497-515.

Vesic, A.S. and Clough, G. W. (1968). “Behavior of Granular Materials under Stresses”. Journal of soil mechanics and Foundation Division,.ASCE,94(SM3),661-688.

Yamamuro, J. and Lade, P. (1996a). “Drained Sand Behavior in Axisymmetric Tests at High Pressures”. Journal of Geotechnical Engineering, 122(2), 109–119.

Yamamuro, J., Bopp, P., and Lade, P. (1996b). “One-Dimensional Compression of Sands at High Pressures”. Journal of Geotechnical Engineering, 122(2), 147–154.

Yashima, S., Kanda, Y. and Sano, S. (1987). “Relationships between particle size and fracture energy or impact velocity required to fracture as estimated from single particle crushing”. Power Technology, 51(3), 277-282.

CHAPTER 3

CONSTITUTIVE MODEL FOR SAND WITH PARTICLE CRUSHING

Generally, dense sand dilates when it is subject to shear stress, while as, loose sand compacts under shear stress. It is understandable that sand particles become break when the high pressure overcomes their strength and resistance. The dilatancy of dense sand turns from positive to negative once the confining pressure is high to cause it to crush. The discussions of dilatancy behavior and particle crushing are confined in the monotonic scope in this study. The features of dilatancy and particle crushing for sand are reviewed. A simple constitutive model for sand with particle crushing is presented in this chapter. Its elasto-plastic tensor form is obtained to simply be integrated with finite element analysis.

3.1 Dilatancy and crushing phenomena of sand

3.1.1 Dilatancy of sand

Shear deformation of sand is often accompanied with volumetric change. Loose sand has tendency to contract to a smaller volume, and densely packed sand can practically deform only when the volume expand somewhat, making the sand looser. The process of volumetric change under the shear stress is called the dilatancy phenomena.

Dilatancy is one of the typical mechanical features of the granular material such as sand. Once the dilatancy occurs, the space among the particles will increase when the shear stress is over each other. The magnitude of dilation depends very strongly on the density of sand.

Here, the concept of soil dilatancy and review of the relationships between the friction angle and the dilatancy angle, density and pressure are introduced. The dilatancy angle and friction angle is specified

both theoretically and experimentally. The relationships between the dilatancy angle, the soil density and pressure are similarly important, but with weak established quantitatively. The dilatancy angle is regarded as the major role in explaining phenomena such the reduction of friction angle with increasing stress level.

From previous discussion by Bolton, M. D. (1986) and Houlsby, G. T. (1991), it is clear that the relationship between the friction angle and the dilatancy angle is firmly established both theoretically and experimentally. Although the analytical approaches may differ, the conclusion is the same. In his research, the dilatancy angle is estimated between 10 and 20 degree.

3.1.2 Crushing of sand

Sand particle crushing can be understood as a decrease in positive dilatancy effect caused by the breakage and rearrangement of particles. The strength and stress-strain behavior of sand particle are significantly affected by the degree of its interior crushing and particle breakage during the process of loading and deformation. Particle crushing is a progressively failure process and the soil particles will rearrange to another stable state again. The significance of crushing behavior on granular materials has been recognized for a long time. The considerable particle breakage is revealed by plenty of laboratory tests, such as the triaxial compression tests or simple shear tests.

Hardin (1985) discussed the influential factors on the particle crushing in aspect of the particle size distribution, effective stress, effective stress path, void ratio, particle hardness and presence and absence of water. Fukumoto (1990), Fukumoto (1992) performed the basic investigation on the particle crushing using the uniformly graded soil samples. Yamamuro and Lade (1996a) and Lade and Yamamuro (1996a) investigated the drained and undrained sand behaviour in axisymmetric test at high pressure. Yamamuro et al. (1996b) examined the sand behaviour under the one-dimensional high compression test. The

factors on particle crushing and the relationship between particle crushing and energy were deeply discussed by Lade et al. (1996b). The effect of time on the particle crushing was examined by Karimpour and Lade (2010).

The tests of sand crushing behavior under shear stress were performed and sand crushing behavior under large shear strain or displacement is investigated by Coop et al. (2004). The crushing behavior are discussed between the stress conditions under triaxial and purely shear test. Sadrekarimi and Olson (2010a) and Sadrekarimi and Olson (2010b) performed the multiple ring shear tests and analyzed the particle crushing and rearrangement.

The particle crushing phenomenon is classified according to three modes shown by Daouadji et al. (2001) in Figure 3.1.

(a) Fracture: a grain breaks into smaller grains of similar sizes.

(b) Attrition: a grain breaks into a single grain of a slightly smaller size and several much smaller ones.

(c) Abrasion: the grain asperities break, resulting in a production of fine particles.

The engineering mechanical properties of sand such as stress-strain, strength and volume variance experience significant change before and after crushing. A remarkable decrease in shear strength and rate of dilatancy occurs in accompany with the particle crushing. In the high stress range, the compressibility of sand becomes so great as a result of particle crushing.

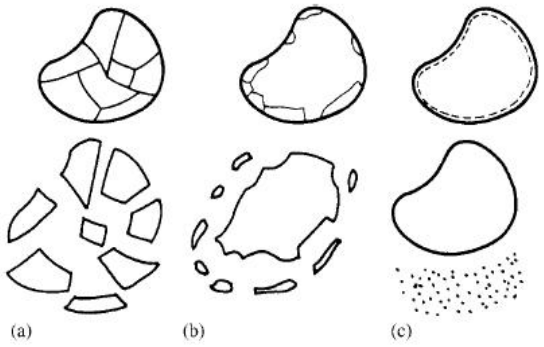

Figure 3.1 Three particle crushing modes (Daouadji et al. (2001))

Particle crushability, however, considerably depends on the physical properties of the component material such as grain size, shape and void ratio.

3.2 Particle crushing and bearing capacity of pile in sand

It is important to thoroughly understand the sand crushing behavior and its effect with regard to engineering structures. The high stress may occur in the situation such as pile end bearing region. Both the features of dilatancy and particle crushing have close relation to the soil behavior in surrounding of pile tip as well as the bearing capacity of pile foundation. The bearing capacity of pile loading into sand is greatly affected by the degree of sand crushing. Moreover, many theoretical estimation formulations are proposed and numerical methods are applied to estimate the bearing capacity of pile considering the factors for sand crushing phenomena.

(a) Theoretical estimation formulations

The cavity expansion method was employed and improved to estimate the end-bearing capacity of pile in crushable soil by Yasufuku et al. (1991), Yasufuku and Hyde (1995). The decrease of friction angle with increasing normal stress was considered in this method. The difficulty in modeling the sand behavior around pile tip was that the high compressibility and highly curved Mohr-Coloumb failure envelopes under the condition of high pressure.

Yang et al. (2006), Yang and Mu (2008), Yu and Yang (2012) investigated the end bearing capacity of pile in sand using the concept of state-dependent strength. To facilitate the state-dependent strength, the correlation between the effective friction angle of sand and the initial confining pressure and relative density was suggested.

(b) Finite element method

It was presented and concluded by Simonini (1996) about the behavior of dense sand around pile tip

in the particle-crushing region which was modeled by finite element method. Two important factors: relative density and mean effective stress level were revealed to influence sand particle crushing. Frictional angle was chosen as strength parameter in the model. The frictional angle decreases as consequence of the particle crushing. The distributions of frictional angle and relative breakage index that indicates the amount of particle crushing at failure around pile tip are reasonably predicted and displayed.

(c) Discrete element method

Lobo- Guerrero and Vallejo (2005), Lobo-Guerrero and Vallejo (2007) investigated the crushing behavior of particle around driven pile using the discrete element method (DEM). The bearing capacity of pile driven in crushable and uncrushable particles were predicted and compared. The effect of particle crushing was apprehended. It is significant to employ the suitable numerical method and constitutive model for describing the crushing behaviour of sand.

3.3 Constitutive model for sand with particle crushing

3.3.1 Review of constitutive model considering particle crushing

In the last thirty years, tremendous progress has been made in the numerical computational analysis. Finite element analysis can be a time-saving and flexible tool compared to traditional experienced-based methods. It is vital to employ a constitutive model to represent the mechanical behavior of sand particle crushing well. Many researchers attempted to propose the constitutive models with the capacity of representing the mechanical behavior of sand in previous research.

Miura et al. (1984) established and proposed a new excellent energy expression to improve the prediction correctness of the modified Cam-clay model for sand in a particle-crushing region. The yield

curve of the stress-strain relationship is modified on a basis of the compression and extension experimental data. However, the model had no capability of describing sand positive dilatancy under relative low confining pressure. In recent decade, Daouadji et al. (2001), Daouadji and Hicher (2010) proposed a constitutive model for sand and its enhanced version taking particle breakage into account in which the grain distribution was chosen as the parameter and proved its new theory on the basis of laboratory tests. Kikumoto et al. (2010) also discussed the behavior of sand crushing with the revised SEVERN-TRENT sand model choosing a grade state index to consider the changing particle size distribution. Hu et al. (2010) discussed the relationship among the breakage index, plastic work and position of the critical state line (CSL) and propose the constitutive model emphasizing the analysis of particle breakage.

The constitutive model proposed by Yao et al. (2008a) is simply computation application and its parameters are determined easily. This elasto-plastic constitutive model display the sand particle crushing behavior is micro viewpoint. The constitutive model revises the hardening parameter to response volumetric variance and affects the expression of yield function.

3.3.2 Prediction theory of the constitutive model for sand with particle crushing

A reasonable hardening parameter controlling plastic volume strain plays a significant role to in order to be appropriate for both clay and sand by Yao et al. (2008b). Yao et al. (2008a) continued to revise the hardening parameter to describe the characteristics of dilatancy. The modified Cam-clay model proposed by Roscoe and Burland (1968) chose the plastic volumetric strain as hardening parameter which is not suitable for dilatant sand. The unified hardening parameter H with the plastic work form is derived by Yao et al. unified hardening parameter by introducing the reference crushing stress p_c. Because of the hardening parameter is non-negative value, the sign of the plastic volumetric strain is

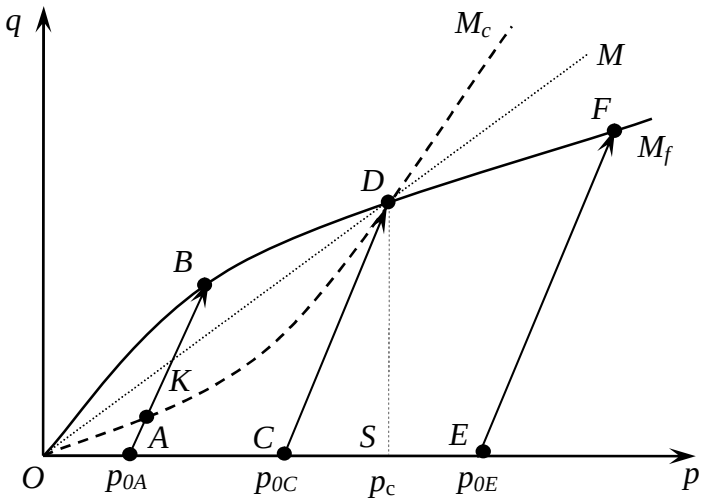

Figure 3.2 The curves of M_c and M_f and stress paths in *p*-*q* plane

determined by the Eq. (3.1).

$$dH = \frac{M_c^4}{M_f^4}\frac{M_f^4 - \eta^4}{M_c^4 - \eta^4} d\varepsilon_v^p \tag{3.1}$$

where, M_c is the stress ratio at characteristic state, M_f is the stress ratio at shear failure defined in Eq. (3.2) and Eq. (3.3) respectively. η means the ratio of deviatoric stress q and mean stress p .

$$M_c = M\left(\frac{p}{p_c}\right)^n \tag{3.2}$$

$$M_f = M\left(\frac{p}{p_c}\right)^{-n} \tag{3.3}$$

where, M and p_c are the stress ratio at critical state and the referenced crushing stress. *n* is the material parameter.

Combining the equation $M_c = q_c / p$ with Eq. (3.2) gives the concrete expression of q_c in Eq. (3.4) and combining the equation $M_f = q_f / p$ with Eq. (3.3) gives the expression of q_f in Eq. (3.5).

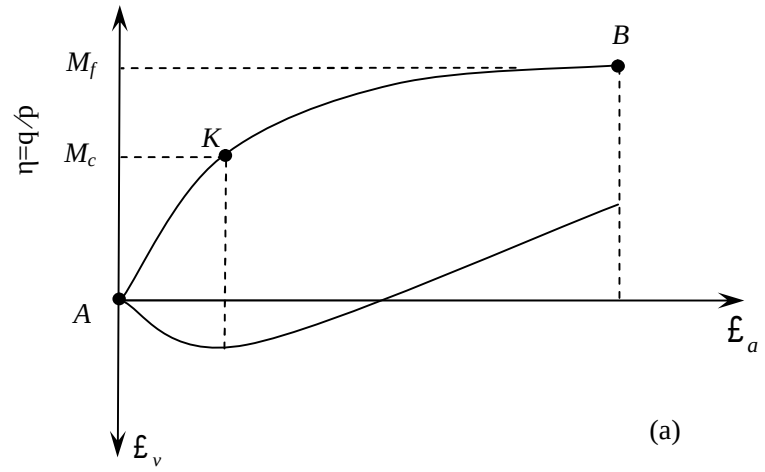

(a) Path *AB*

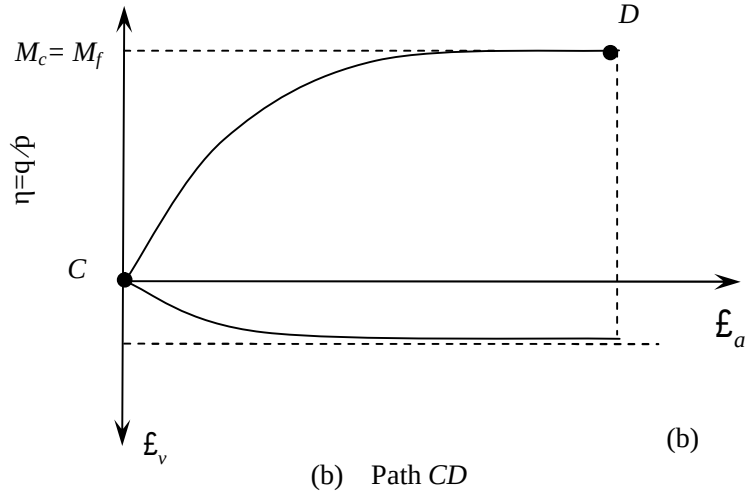

(b) Path *CD*

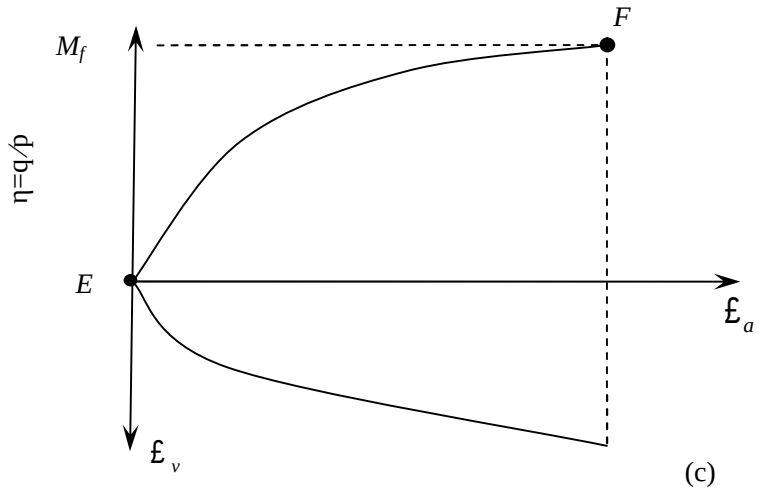

(c) Path *EF*

Figure 3.3 The curves of stress-strain relationship at different stress levels

In Figure 3.2, the horizontal axis stands for the mean stress and vertical axis stands for the devatoric stress. The capital letter *AB*, *CD* and *EF* standing for stress paths with different initial confining pressure level are correspondent to the curves in Figures 3.3 (a), (b) and (c) respectively. It follows the sign convention in soil mechanics; compression is ruled to be positive value.

$$q_c = Mp_c^{-n} p^{1+n} \tag{3.4}$$

$$q_f = Mp_c^{n} p^{1-n} \tag{3.5}$$

Path *AB*: Stress path begins from the point *A* (low confining pressure) in the Figure 3.3 (a). The characteristic state will not change until it reaches the point *K*. The plastic volume increment $d\varepsilon_v^p$ is positive in *AK* phase. The value of $d\varepsilon_v^p$ turns to negative because of it overcomes line in *KB* phase.

We observe the final stage is positive dilatancy $\left(d\varepsilon_v^p < 0\right)$. Although in the beginning stage, the curve shows the negative dilatancy $\left(d\varepsilon_v^p > 0\right)$.

Path *CD*: From Figure 3.3 (b), the loading begins from the point *C* (medium confining pressure). The characteristic state changes and failure happens at the same time. The $d\varepsilon_v^p$ is constantly positive during the entire loading process. The final stage is negative dilatancy $\left(d\varepsilon_v^p > 0\right)$. These three curves intersect at the point *D* ($M_c = M = M_f$) as shown in Figure 3.2.

Path *EF*: From Figure 3.3 (c), the loading begins from the point *E* (high confining pressure), failure happens before the characteristic state changes because that the stress path touches the failure line earlier. The final stage is negative dilatancy $\left(d\varepsilon_v^p > 0\right)$.

It is concluded that the revised hardening parameter is able to predict the sand behavior from negative dilatancy to positive dilatancy when the confining pressure is low, while only negative dilatancy when the confining pressure is high enough.

3.3.3 Yield function

In the modified Cam-clay model, the relationships between the elastic volumetric strain $£_v^e$, plastic volumetric strain $£_v^p$ and the logarithm of mean stress $\ln(p)$ are expressed in linearity. On the other hand, based on the experimental results on Toyoura sand, the relationships are derived by the following reasonable power exponential law of mean stress by Nakai (1989).

$$£_v^e = C_e\left[\left(\frac{p_x}{p_a}\right)^m - \left(\frac{p_o}{p_a}\right)^m\right] \tag{3.6}$$

$$£_v^p = (C_t - C_e)\left[\left(\frac{p_x}{p_a}\right)^m - \left(\frac{p_o}{p_a}\right)^m\right] \tag{3.7}$$

Where, p_o is the initial mean stress, p_a is the atmospheric pressure, C_t is the compression index, C_e is the swelling index and m is a coefficient for sand. p_a takes the value of 0.1 MPa. p_x is the mean stress in Eq. (3.6) and Eq. (3.7). The compression and swelling indexes and material parameter m of the Toyoura sand in a wide range of isotropic stress can be determined by Sun et al. (2007).

The stress-dilatacy equation can be expressed as follows in Eq. (3.8),

$$\frac{d£_v^p}{d£_d^p} = \frac{M_c^2 p^2 - q^2}{2pq} \tag{3.8}$$

The normality condition is shown in Eq. (3.9)

$$dp \cdot d£_v^p + dq d£_d^p = 0 \tag{3.9}$$

Where, $d£_v^p$ is the plastic volumetric stain increment and $d£_d^p$ the plastic deviatoric stain increment.

By combining Eq. (3.8) and Eq. (3.9), the yield locus of crushing model is obtained as follows,

$$f = (2n+1)\frac{p_c^{2n}}{M^2}\cdot\frac{q^2}{p} + p^{2n+1} - p_x^{2n+1} = 0 \tag{3.10}$$

In Eq. (3.10) when n is equal to 0, the yield function is reduced to that of the Modified Cam-clay model. The mean stress p_x at isotropic loading is linked to plastic volumetric strain ε_v^p by Eq. (3.7). The Eq. (3.10) can be transformed as Eq. (3.11)

$$p_x = \left[(2n+1)\frac{p_c^{2n}}{M^2}\cdot\frac{q^2}{p} + p^{2n+1}\right]^{\frac{1}{(2n+1)}} \tag{3.11}$$

By combining Eq. (3.7) and Eq. (3.11), rearranging the expression result and replacing the new revised hardening parameter H , we have

$$f = \frac{C_t - C_e}{p_a^m}\left\{\left[\frac{(2n+1)p_c^{2n}}{M^2}\times\frac{q^2}{p} + p^{2n+1}\right]^{\frac{m}{2n+1}} - p_o^m\right\} - H = 0 \tag{3.12}$$

Eq. (3.12) is the yield function of the crushing model. Crushing model takes the associated flow rule, so that plastic potential function g is identical to yield function f . The plastic strain increment $d\varepsilon_{ij}^p$ can be calculated using the flow rule in Eq. (3.13).

$$d\varepsilon_{ij}^p = \Lambda\frac{\partial g}{\partial \sigma_{ij}} \tag{3.13}$$

Where, Λ is a scalar.

The elastic modulus is not constant value when the outer force is enhanced. From the generalized

Hooke law, we can obtain the following relationship:

$$d\varepsilon_v^e = d\varepsilon_{11}^e + d\varepsilon_{22}^e + d\varepsilon_{33}^e = \frac{3(1-2\neg)}{E} dp \tag{3.14}$$

Make the differential calculation of Eq. (3.6), it finds,

$$d\varepsilon_v^e = \frac{mC_e}{p_a^m} p^{m-1} dp \tag{3.15}$$

Combine the Eq. (3.14) and Eq. (3.15), the elastic modulus E varies with the mean stress and is expressed as in Eq. (3.16),

$$E = \frac{3(1-2\neg)\, p_a^m}{m C_e\, p^{m-1}} \tag{3.16}$$

Where $\neg$ is the Poisson ratio and takes value of 0.3 in this study.

3.3.4 Determination of the parameters for the constitutive model (Toyoura sand)

Generally, there are seven parameters in this constitutive model for sand with crushing. Except the Poisson ratio $\neg$ which is assumed to be 0.3, the other six parameters can be determined via the conventional triaxial compression test. $C_e = 0.0016$, $C_t = 0.0044$ and material parameter m= 0.5 are from experiment performed by Sun et al. (2007). In Sun's conventional triaxial compression test, specimen of Toyoura sand also adopts the relative density as 90%. Drained triaxial compression test for Toyoura sand at the confining pressure of 0.2 MPa, 0.5 MPa, 1 MPa, 2 MPa, 4 MPa and 8 MPa each are performed. It was found that both the stress ratio q_f / p and the strain increment ratio $d\varepsilon_v / d\varepsilon_a$ becomes constant values when the Toyoura sand is in failure state under different confining pressures. Besides, connecting the points according to failure states in the $d\varepsilon_v / d\varepsilon_a$ and q_f / p plane

Table 3.1 The seven parameters of the constitutive model for Toyoura sand (D_r=90%)

Isotropic consolidation	Triaxial compression	Poisson ratio
$C_e = 0.0016$	$M = 1.35$	
$C_t = 0.0044$	$p_c = 5.85 MPa$	¬ = 0.3
$m = 0.5$	$n = 0.085$	

provides a straight line as shown in Figure 3.4. On the linear relation between these two ratio values, the elastic deformation part is ignored. The peak stress ratio is assumed to be equal to M when the volumetric strain increment is zero ($d£_v / d£_a = 0$). Utilizing the above linear relationship, we can determine M as 1.35 and then make rearrangement of Eq. (3.3), obtaining the Eq. (3.17).

$$\ln M_f = -n \ln p + n \ln p_c + \ln M \tag{3.17}$$

According to the relationship between the curve M_f and the mean stress p in test, we can draw the line on Figure 3.5 to express the relationship between $\ln(M_f)$ and $\ln(p)$, then we can get the value of $p_c = 5.85$ MPa and $n = 0.085$ respectively. The seven parameters are shown in the Table 3.1.

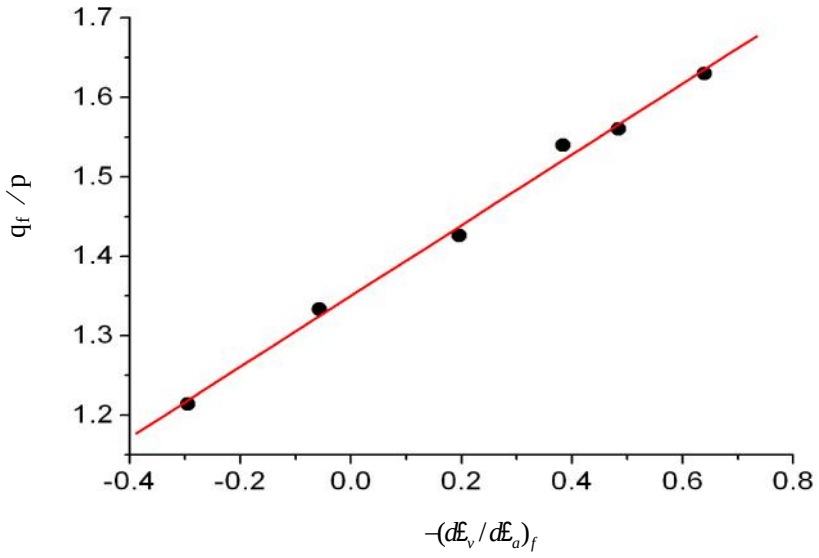

Figure 3.4 The relationship between q_f/p and $-(d£_v/d£_a)_f$ at failure state under different confining pressures

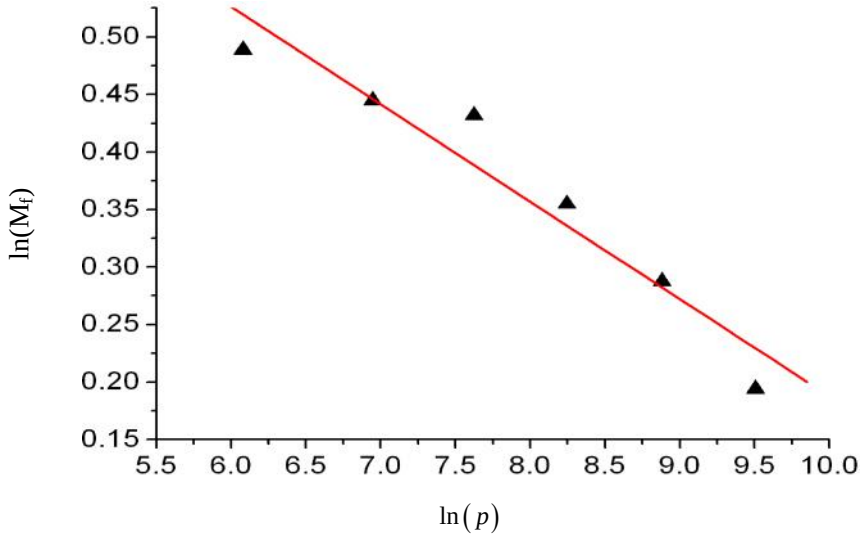

Figure 3.5 The relationship between $\ln(M_f)$ and $\ln(p)$

3.3.5 Validation of the constitutive model (Toyoura sand)

Sun et al. (2007) performed triaxial compression tests on Toyoura sand at different confining pressures as 0.2 MPa, 0.5 MPa, 1 MPa, 2 MPa , 4 MPa and 8 MPa. The size of the specimen was 100mm in height and 50mm in diameter. The relationships between the stress ratio and the axial strain, the volumetric strain and the axial strain, the stress ratio and the radial strain are shown in Figure 3.6, Figure 3.7 and Figure 3.8. From the Figure 3.6, we can confirm that stress ratio decreases when the confining pressure increases. The predicted values agree quite well with the experimental results when the confining pressure is low. In addition, it is observed that the stress ratio remains constant when sand specimen enters into failure with the accumulation of axial strain. The reduction of strength is resulted from the particle crushing. From the Figure 3.7, we can conclude that the constitutive model for sand with particle crushing can predict dilatancy behavior from negative to positive when the confining pressure is low, at the values of 0.2 MPa, 0.5 MPa, 1 MPa and 2 MPa. It predicts the negative dilatancy when the confining pressures are 4 MPa and 8 MPa. The sharp volumetric reduction of the specimen is attributed to particle crushing. The predicted volume of the sand specimen agrees with the test results

expect when confining pressure is 8 MPa. In Figure 3.8, the curves variation tendency is similar to these in Figure 3.6. Stress ratio becomes almost a constant value after failure state happens.

In summary, this simple constitutive model with particle crushing is capable of describing volumetric change of sand during shear before and after crushing occurrence. The different dilatancy behaviors of sand can be represented in this unified constitutive model. Meanwhile, the strength reduction with increasing confining pressure is well predicted. Besides, regardless of complicated mechanical process, some other complex features of particle crushing are not considered by this simple model.

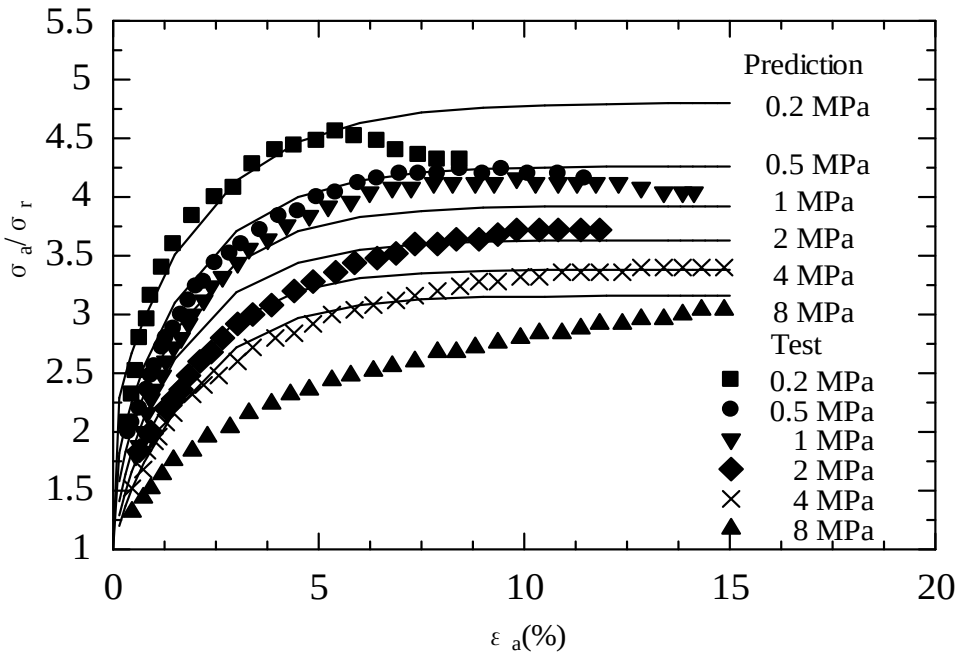

Figure 3.6 Relationship between stress ratio and axial strain for Toyoura sand

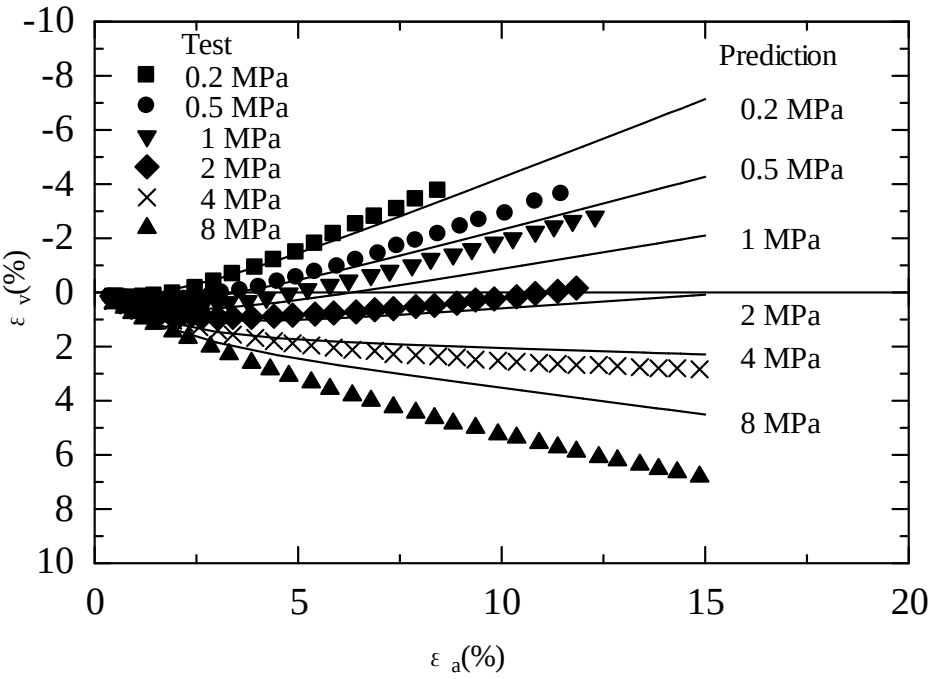

Figure 3.7 Relationship between volumetric strain and axial strain for Toyoura sand

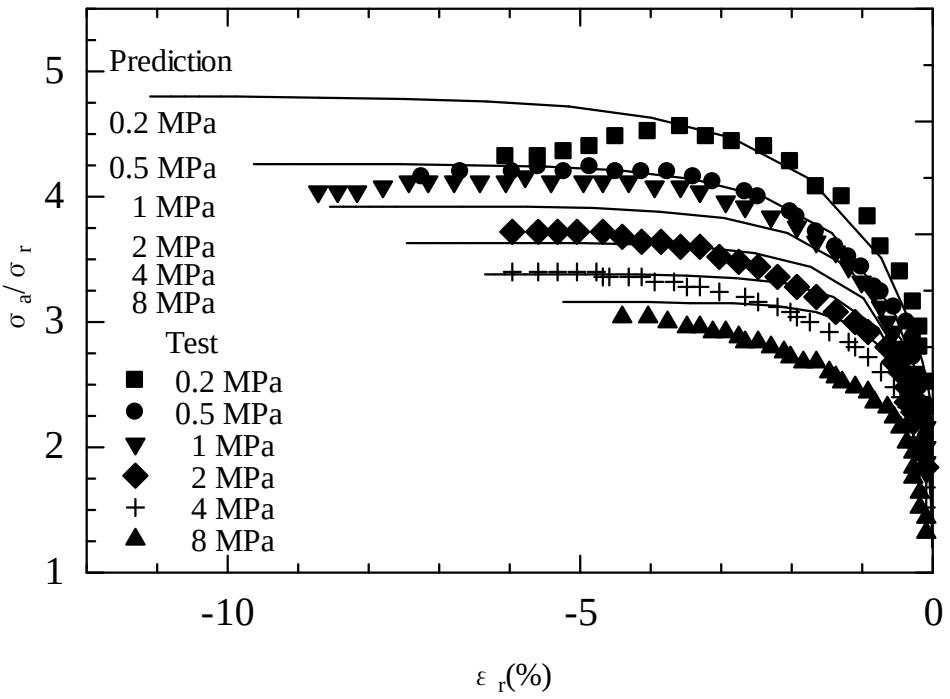

Figure 3.8 Relationship between stress ratio and radial strain for Toyoura sand

3.3.6 Determination of the parameters for the constitutive model (Masado)

To confirm the validity of constitutive model with particle crushing for other granular materials, the predicted values by constitutive model with particle crushing is compared with the results of triaxial compression test on Masado. Masado is one of unusual soils in Japan because of its collapsibility. Murata et al. (1988) performed a series of triaxial compression tests on Masado to investigate its mechanical properties. The specimen with different densities at various confining pressure were tested. The experimental results were obtained from the dense specimen with initial void ratio 0.78. The standard triaxial compression tests on the specimens were done under a consolidated – drained condition at confining pressure as 30 kPa, 60 kPa, 100 kPa, 200kPa and 400 kPa. The occurrence of particle crushing was manifested by measuring the increase of surface area in triaxial compression test.

The parameter determination method is examined previously. The experimental data show that the term q_f / p and $d\varepsilon_v / d\varepsilon_a$ displays the liner relationship. The parameter *M* is determined as 1.8 in Figure 3.9 when $d\varepsilon_v / d\varepsilon_a = 0$.

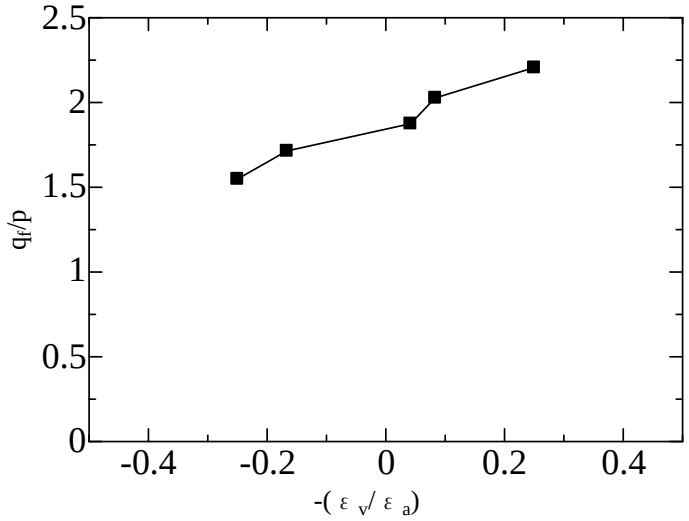

Figure 3.9 The relationship between q_f/p and $-(d\varepsilon_v/d\varepsilon_a)_f$ at failure state under different confining pressures for Masado

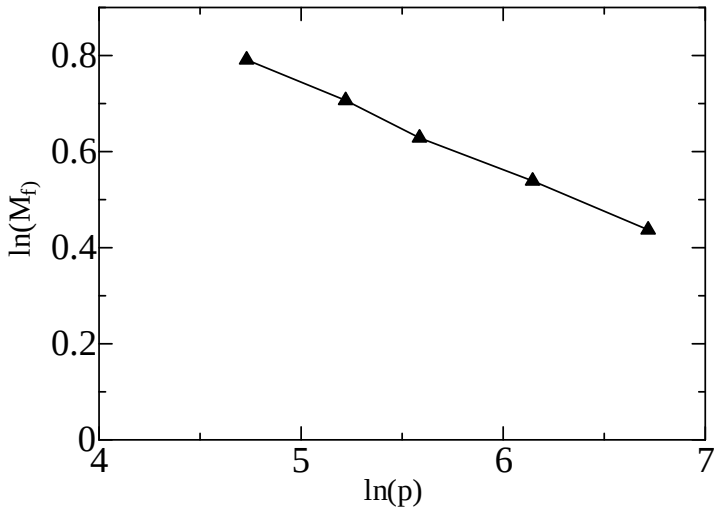

Figure 3.10 The relationship between ln(M_f) and ln(p) for Masado

On Figure 3.10, it express the relationship between $\ln(M_f)$ and $\ln(p)$. Then we can get the value of $p_c = 412$ kPa and $n = 0.1782$ respectively for Masado. The reference crushing stress is smaller than and about a tenth of that for Toyoura sand.

From the isotropic loading and unloading test on Masado by Murata et al. (1988), the compression index C_t is obtained as 0.01494 , swelling index C_e is 0.00637 and material parameter m= 0.8.

3.3.7 Validation of the constitutive model (Masado)

The predicted values are compared with the experimental results at different confining pressures. The predicted and experimental relationship between the deviatoric stress and the axial strain of Masado is represented in Figure 3.11. It is observed that the deviatoric stress increases as the confining pressure is improved. The predicted values are agreeable with the experimental results at confining pressure as 30 kPa, 60 kPa and 100 kPa. However, the relationship is overestimated by predicted values when confining pressure is 200 kPa and 400 kPa.

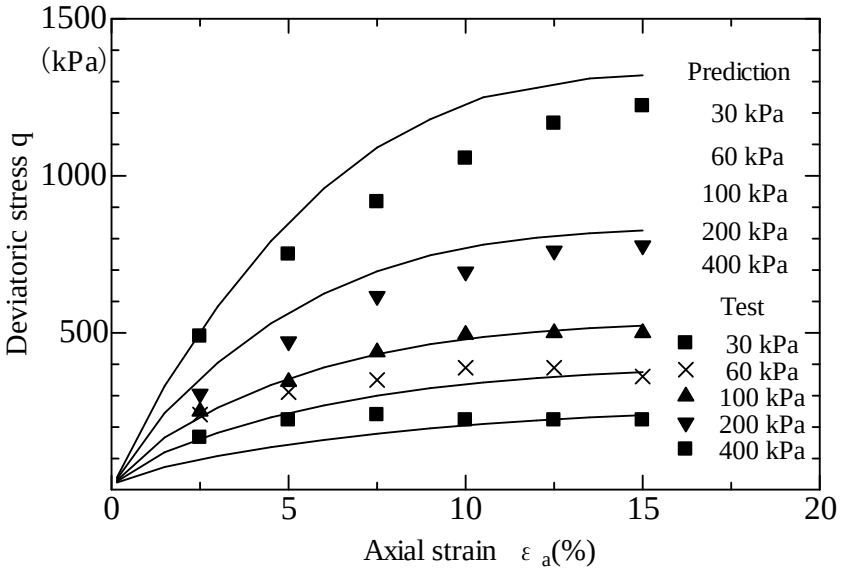

Figure 3.11 Relationship between deviatoric stress and axial strain for Masado

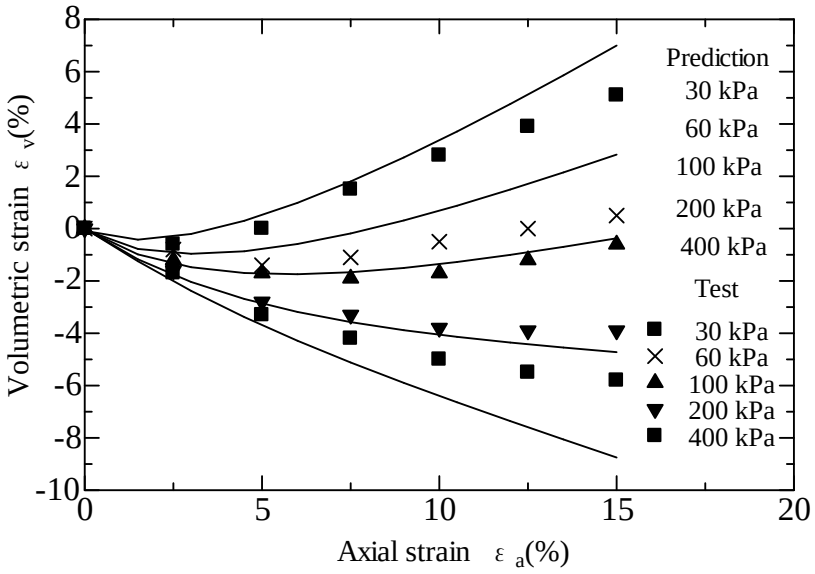

Figure 3.12 Relationship between volumetric strain and axial strain for Masado

The relationship between the volumetric strain and axial strain is represented in Figure 3.12. The predicted values can predict the dilatancy from negative to positive at confining pressure as 30 kPa and 60 kPa, showing agreement with test results. And only the negative dilatancy when confining pressure is 100 kPa, 200 kPa and 400 kPa. The predicted values overestimate the positive dilatancy at low confining pressure as 30 kPa and the negative dilatancy at high confining pressure as 400 kPa.

3.4 Parametric study of the reference crushing stress p_c

The value of reference crushing stress pc plays a significant role in predicting the dilatancy behavior of granular materials in the constitutive model for sand with particle crushing. Therefore, the parametric study is conducted to understand the influence of reference crushing stress p_c on the predicted mechanical behavior.

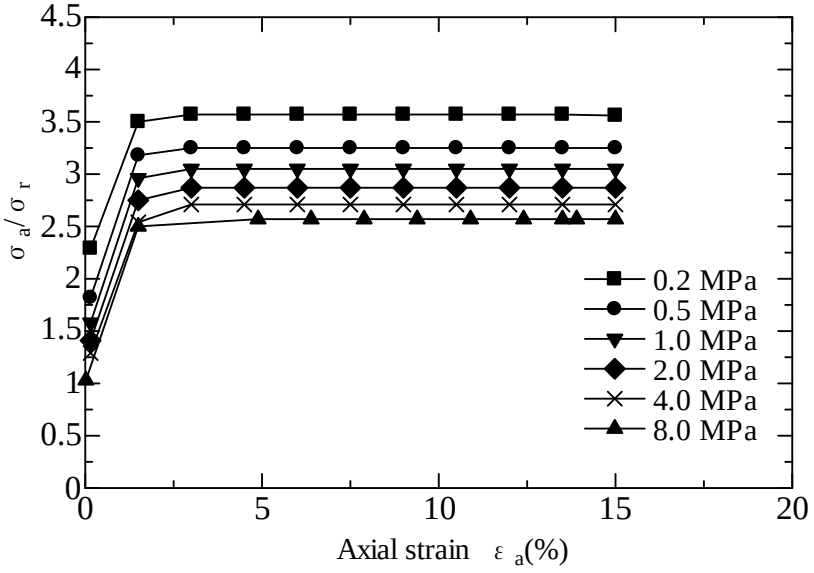

Figure 3.13 Relationship between stress ratio and axial strain (p_c =0.5 MPa)

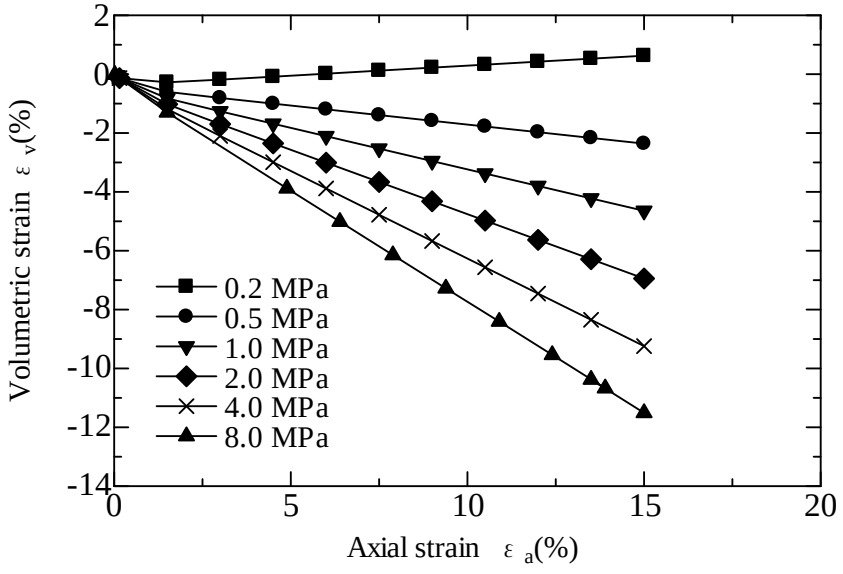

Figure 3.14 Relationship between volumetric strain and axial strain (p_c =0.5 MPa)

The parametric study of reference crushing stress pc is implemented by changing the value of pc. The reference crushing stress pc are selected as 0.5 MPa, 2 MPa and 4 MPa respectively. The other parameters for Toyoura sand is keep the same. The numerical results adopting different pc are represented from Figure 3.13 to Figure 3.18. It is concluded that the stress ratio increase as the reference crushing stress pc is improved. The stress ratio is around 3.5 at confining pressure 30 kPa with pc as 0.5 MPa in Figure 3.13, while it reaches 4.5 at confining pressure 30 kPa with p_c as 4 MPa in Figure 3.17.

The numerical relationship adopting different reference crushing stress p_c between the volumetric strain and axial stain are shown in Figure 3.14, Figure 3.16 and Figure 3.18. The predicted results represent remarkable negative dilatancy as reference crushing stress p_c decreases. The maximum volumetric strain is 12% when the reference crushing stress pc is 0.5 MPa in Figure 3.14. The maximum volumetric strain reduces to half when the reference crushing stress pc is raised to 4 MPa in Figure 3.18. Besides, the positive dilatancy appears only at confining pressure 30 kPa when the reference crushing stress p_c is 0.5 MPa. As the reference crushing stress pc increases, the constitutive model display the tendency of predicting obvious positive dilatancy.

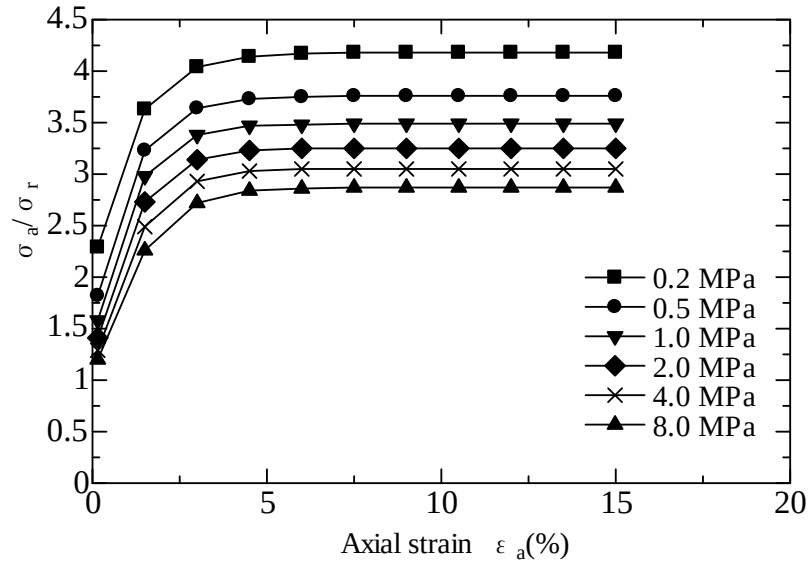

Figure 3.15 Relationship between stress ratio and axial strain (p_c =2.0 MPa)

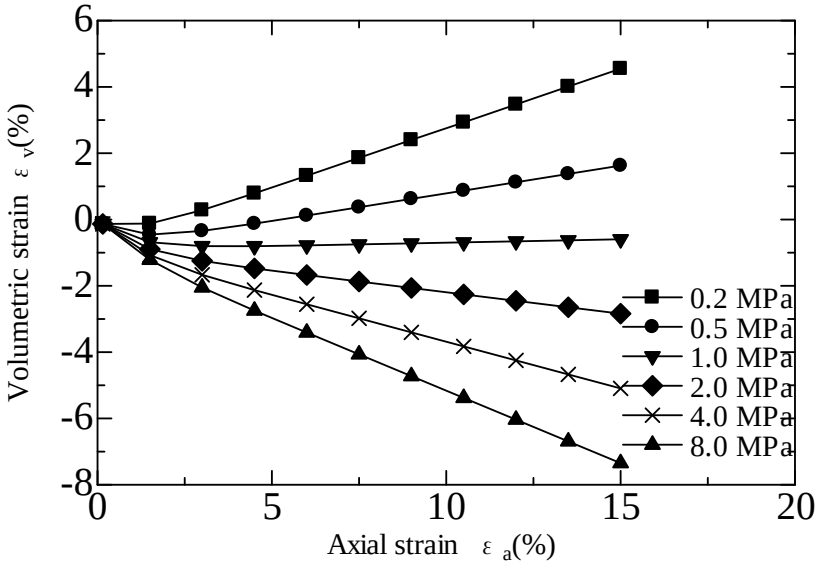

Figure 3.16 Relationship between volumetric strain and axial strain (p_c =2.0 MPa)

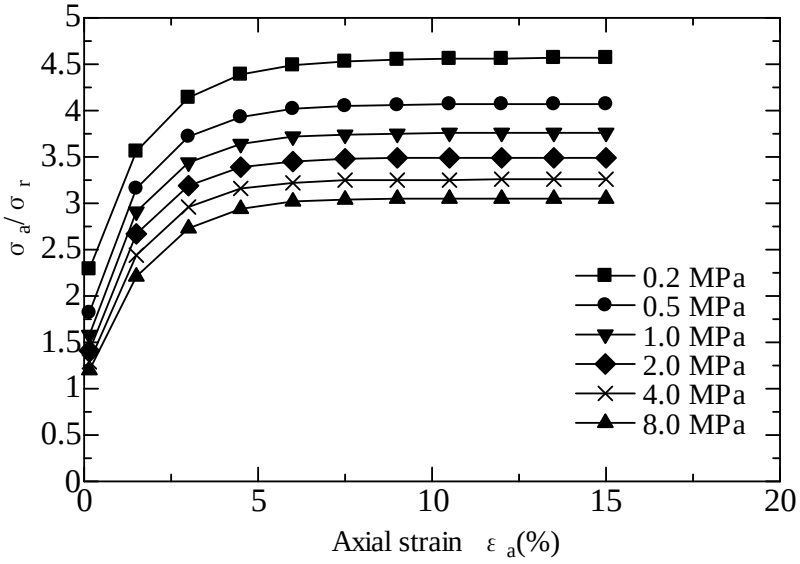

Figure 3.17 Relationship between stress ratio and axial strain (p_c=4.0 MPa)

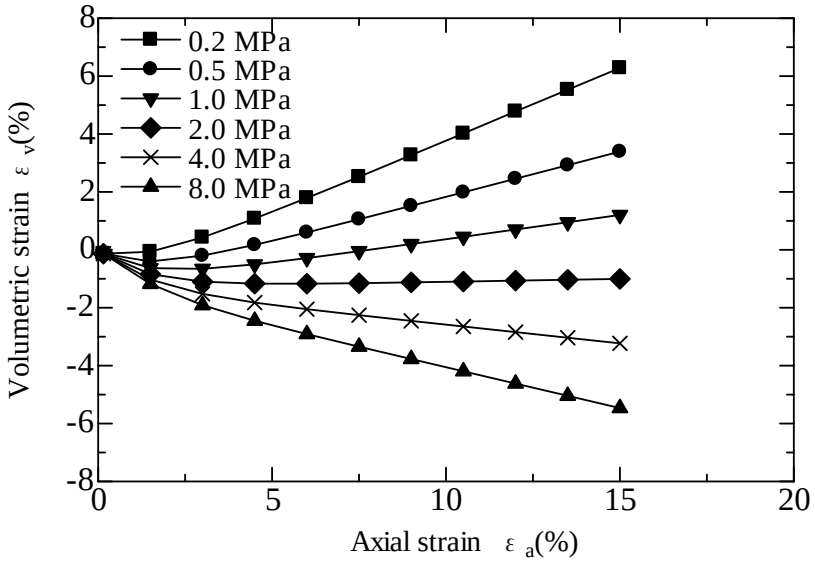

Figure 3.18 Relationship between volumetric strain and axial strain (p_c =4.0 MPa)

Based on the above analysis, it is understandable that the reference crushing stress p_c in constitutive model is the inherent features of sand and determined by the composition of micro-structure. p_c is not the specific ultimate strength of the particle when crushing occurs but is dependent on the ultimate strength of particle to some degree. For the mixture soil composed with multiple kinds of sand, the reference crushing stress pc of mixture soil is related to the reference crushing stress p_c for each kind of sand and can be decided by the experimental results on mixture soil.

3.5 Tensor of the constitutive model

To integrate this constitutive model with the finite element analysis, the elastoplastic constitutive tensor for the proposed model is derived here. The relationship between the elastic stress and strain is expressed in the incrementally linear form as Eq. (3.18).

$$d\sigma_{ij} = D^{e}_{ijkl}(d\varepsilon_{kl} - d\varepsilon^{p}_{kl}) \tag{3.18}$$

Where, D^{e}_{ijkl} is the elastic constitutive tensor. ε_{kl} and ε^{p}_{kl} are the total strain tensor and its plastic component. The yield function f is the function of the stress tensor and the hardening parameter H shown in Eq. (3.12). The consistency condition can be expressed by

$$\frac{\partial f}{\partial \sigma_{ij}} d\sigma_{ij} + \frac{\partial f}{\partial H} dH = 0 \tag{3.19}$$

Substituting Eqs. (3.1), (3.13) and (3.18) into Eq. (3.19) gives Eq. (3.20)

$$\Lambda = \frac{\dfrac{\partial f}{\partial \sigma_{ij}} D^{e}_{ijkl} d\varepsilon_{kl}}{X} \tag{3.20}$$

where

$$X = \frac{M_c^4}{M_f^4}\frac{M_f^4 - \eta^4}{M_c^4 - \eta^4}\frac{\partial f}{\partial \sigma_{ij}}\delta_{ij} + \frac{\partial f}{\partial \sigma_{ij}} D_{ijkl}^e \frac{\partial f}{\partial \sigma_{kl}} \tag{3.21}$$

Substituting Eqs. (3.13) and (3.20) into Eq. (3.18), we get a general form of the proposed model as Eq. (3.22)

$$d\sigma_{ij} = D_{ijkl} d\varepsilon_{kl} \tag{3.22}$$

Where the elastoplastic constitutive tensor D_{ijkl} is expressed as Eq. (3.23)

$$D_{ijkl} = D_{ijkl}^e - D_{ijpq}^e \frac{\partial f}{\partial \sigma_{pq}} \frac{\partial f}{\partial \sigma_{st}} D_{stkl}^e / X \tag{3.23}$$

The elastic and elastoplastic constitutive tensor of Hooke's law for isotropic elasticity can be written as follows in Eq. (3.24) and Eq. (3.25)

$$D_{ijkl}^e = L\delta_{ij}\delta_{kl} + G(\delta_{ik}\delta_{jl} + \delta_{il}\delta_{jk}) \tag{3.24}$$

$$D_{ijkl} = L\delta_{ij}\delta_{kl} + G(\delta_{ik}\delta_{jl} + \delta_{il}\delta_{jk}) - \left(L\frac{\partial f}{\partial \sigma_{pp}}\delta_{ij} + 2G\frac{\partial f}{\partial \sigma_{ij}}\right)\left(L\frac{\partial f}{\partial \sigma_{qq}}\delta_{kl} + 2G\frac{\partial f}{\partial \sigma_{kl}}\right) / X \tag{3.25}$$

Where G and L are Lame's constants. And substitute the expression of elastic modulus in Eq. (3.16) into G and L in Eq. (3.26) and Eq. (3.27).

$$G = \frac{E}{2(1+\nu)} = \frac{3(1-2\nu)p_a^m}{2mC_e p^{m-1}(1+\nu)} \tag{3.26}$$

$$L = \frac{E}{3(1-2\nu)} - \frac{2}{3}G = \frac{p_a^m}{mC_e p^{m-1}} - \frac{2}{3}G \tag{3.27}$$

3.6 Summary

In this chapter, the effects of the dilatancy and particle crushing on the sand behaviors are reviewed. It is necessary to consider the mechanical features change of particle crushing to estimate the bearing capacity of pile loading into sand.

The constitutive model for sand with particle crushing is reviewed in detail. The constitutive model is adopted in the finite element analysis to represent the sand behavior. The constitutive model is capable of predicting the dilatancy behavior of sand from positive to negative under low confining pressure, and only the negative dilatancy under high confining pressure. This model could response the strength reduction of sand with increasing confining pressure. The constitutive model is simply computation application and its seven parameters are determined easily. To directly integrate this constitutive model with the finite element analysis, the elastoplastic constitutive tensor for the model is obtained and given.

The parameters of constitutive model with particle crushing for Masado are also determined on basis of triaxial compression test. The parametric study of reference crushing stress pc on dilatancy behavior is conducted as well. The parametric study on the reference crushing stress pc is numerically conducted. The predicted results represent remarkable negative dilatancy as the reference crushing stress pc decreases. Meanwhile, the constitutive model display the tendency of predicting obvious positive dilatancy as the reference crushing stress pc increases.

Reference

Bolton, M. D. (1986). “The strength and dilatancy of sand”. Geotechnique, 36(1), 65-78.

Coop, M. R., Sorensen, K. K., Bodas Freitas, T. and Georgoutsos, G. (2004). “Particle breakage during shearing of a carbonate sand”. Geotechnique, 54(3), 157-163.

Daouadji, A., Hicher, P. Y. and Rahma, A. (2001). “An elastoplastic model for granular materials taking into account grain breakage”. European Journal of Mechanics a-Solids, 20(1), 113-137.

Daouadji, A. and Hicher, P. Y. (2010). “An enhanced constitutive model for crushable granular materials”. International Journal for Numerical and Analytical Methods in Geomechanics, 34(6), 555-580.

Fukumoto, T. (1990). “A grading equation for decomposed granite soil”. Soils and Foundations, 30(1), 27-34.

Fukumoto, T. (1992). “Particle Breakage Characteristics of Granular Soils”. Soils and Foundations, 32(1), 26-40.

Hardin, B. (1985). “Crushing of Soil Particles”. Journal of Geotechnical Engineering. ASCE, 111(10), 1177–1192.

Hu, W., Yin, Z. Y. and Dano, C. and Hicher, P. Y. (2011). “A constitutive model for granular materials considering grain breakage”. Science China Technological Sciences, 54(8), 2188-2196.

Houlsby, G. T. (1991). “How the dilatancy of soils affects their behaviour”. The proceeding of the Tenth European Conference on Soil Mechanics and Foundation Engineering, Florence, Italy, Vol 4,1189-1202.

Kikumoto, M., Wood, D. M. and Russell, A. (2010). “Particle crushing and deformation behaviour”. Soils and Foundations, 50(4), 547-563.

Lade, P. and Yamamuro, J. (1996a). “Undrained Sand Behavior in Axisymmetric Tests at High Pressures”. Journal of Geotechnical Engineering. ASCE, 122(2), 120–129.

Lade, P., Yamamuro, J., and Bopp, P. (1996b). “Significance of Particle Crushing in Granular Materials”. Journal of Geotechnical Engineering. ASCE, 122(4), 309–316.

Lobo- Guerrero and Vallejo (2005). “DEM analysis of crushing around driven piles in granular materials”. Geotechnique, 55(8), 617-623.

Lobo- Guerrero and Vallejo (2007). “Influence of pile shape and pile interaction on the crushable behavior of granular materials around driven piles: DEM analyses,” Granular matter, 9(3-4), 241-250.

Miura, N., Murata, H. and Yasufuku, N. (1984). “Stress-strain characteristics of sand in a particle-crushing region”. Soils and Foundations, 24(1), 77-89.

Murata, H., Hyodo, M. and Yasufuku, N. (1988) “Prediction of Stress-Strain Behaviour of Undisturbed Masado”. Technology reports of the Yamaguchi University, 4(2), 161-170.

Nakai, T. (1989). “An isotropic hardening elastoplastic model considering the stress path dependency in three-dimensional stresses”. Soils and Foundations, 29(1), 119-139.

Roscoe, K. H. and Burland, J.B. (1968) “On the Generalised Stress-Strain Behavior of “Wet” Clay”. Engineering Plasticity, Cambridge University Press, Cambridge, UK, 535-609.

Sadrekarimi, A. and Olson, S. (2010a). “Particle damage observed in ring shear tests on sands”. Canadian Geotechnical Journal, 47(5), 497-515

Sadrekarimi, A. and Olson, S. (2010b). “Shear Band Formation Observed in Ring Shear Tests on Sandy Soils”. Journal of Geotechnical and Geoenvironmental Engineering, 136(2), 366–375.

Simonini, P. (1996). “Analysis of Behavior of Sand Surrounding Pile Tips”. Journal of Geotechnical Engineering, 122(11), 897–905.

Sun, D. A., Huang, W. X., Sheng, D.C. and Yamamoto, H. (2007). “An elastoplastic model for granular materials exhibiting particle crushing”. Key Engineering Materials, 41, 1273-1278.

Yamamuro, J. and Lade, P. (1996a). “Drained Sand Behavior in Axisymmetric Tests at High Pressures”. Journal of Geotechnical Engineering. ASCE, 122(2), 109–119.

Yamamuro, J., Bopp, P., and Lade, P. (1996b). “One-Dimensional Compression of Sands at High Pressures”. Journal of Geotechnical Engineering. ASCE, 122(2), 147–154.

Yang, J., Tham, L. G., Lee, P. K. K., Chan, S. T. and Yu, F. (2006). “Behavior of jacked and driven piles in sandy soil”. Geotechnique, 56(4), 245-259.

Yang, J., and Mu, F. (2008) “Use of State-Dependent Strength in Estimating End Bearing Capacity of Piles in Sand”. Journal of Geotechnical and Geoenvironmental Engineering, 134(7), 1010-1014.

Yao, Y. P., Sun, D. A. and Matsuoka, H. (2008a). “A unified constitutive model for both clay and sand with hardening parameter independent on stress path”. Computers and Geotechnics, 35(2), 210-222.

Yao, Y. P., Yamamoto, H. and Wang, N. D. (2008b). “Constitutive model considering sand crushing”. Soils and Foundations, 48(4), 603-608.

Yasufuku, N., Mirata, H. and Hyodo, M. (1991). “Yield Characteristics of anisotropically Consolidated Sand under Low and High Stress”. Soils and Foundations, 31(1), 95-109.

Yasufuku, N and Hyde, A. F. L. (1995). “Pile end-bearing capacity in crushable sands”. Geotechnique, 45(4), 663-676.

Yu, F., and Yang, J. (2012). “Base Capacity of Open-ended Steel Pipe Piles in Sand”. Journal of Geotechnical and Geoenvironmental Engineering, 138(9), 1116-1128.

CHAPTER 4

LARGE DEFORMATION THEORY AND JOINT ELEMENT USED FOR THE ANALYSIS OF PILE LOADING TEST

The deformation of geo-structure involves strong nonlinearities. One is from the mechanical characteristics from the material. Another is due to the effect of deformation on the overall geometry change of the structure. It is well recognized that deformation can become large during the loading process. It is important to consider the geometrical nonlinearity caused by the large deformation to establish a model of the actual behavior of the structure.

It is well known that interfaces usually play a major role in the definition of the mechanical behavior of structure having interaction with the soil. Consequently, it is significant to employ a suited constitutive relationship for modeling the heavily loaded interactive region. The zero-thickness joint element simulating soil-pile interaction is employed in the finite element analysis.

4.1 Review of large deformation theory in geomechanics

The deformation of soil under complex stresses in the soil surrounding the pile tip exhibits typical large deformation behavior in geotechnical engineering. To obtain more accurate and reliable numerical solutions and insightfully capture the essence of the problem, it is necessary to employ the finite element analysis using large deformation theory to tackle the pile loading and penetrating problem.

In the past thirty years, tremendous progress has been made in the numerical analysis of pile foundations. For example, Finite element method is a time-saving and flexible tool compared to traditional experience-based methods. However, the numerical analysis of pile loading is generally

challenging because the soil-structure interaction system involving large deformations is complicated. To solve this complicated problem and describe the actual behavior of the structure, the large deformation theory is incorporated with the finite element analysis.

Many researchers have attempted to solve the pile loading and penetration problem using large deformation theory. Kiousis et al. (1986) and Kiousis et al. (1988) have proposed the large deformation theory and the application of cone penetration. Hu and Randolph (1998a) and Hu and Randolph (1998b) have presented a practical approach, the arbitrary Lagrangian Eulerian (ALE) method, to solve large deformation problems, such as the bearing capacity of footing using the well-established small-strain finite element code. Sheng et al. (2005), Sheng et al.(2008) and Sheng et al. (2009) had initially adopted the friction slip method and frictional element method to tackle deep penetration and the soil-pile contact problem. Nazem et al. (2006), Nazem et al. (2008), Nazem et al. (2009) and Nazem et al. (2010) have presented the arbitrary Lagrangian Eulerian method combined with adaptive computation technology to analyze large deformations in geomechanics, extending these strategies to consolidation and dynamic problems. Recently, Qiu et al. (2011a), Qiu and Henke (2011b) and Qiu and Grade (2012) have employed the coupled Eulerian-Lagrangian (CEL) method to investigate the spudcan pile foundation penetration in loose sand overlaid on weak clay. Vavourakis et al. (2013) have discussed remeshing and remapping technologies for large deformation analysis. In recent years, ALE and CEL methods have been positively adopted and popularized in succession. However, these two methods are complicated because of the intricate nature of the remeshing and adaptive process.

4.1.1 Basic theory for large deformation

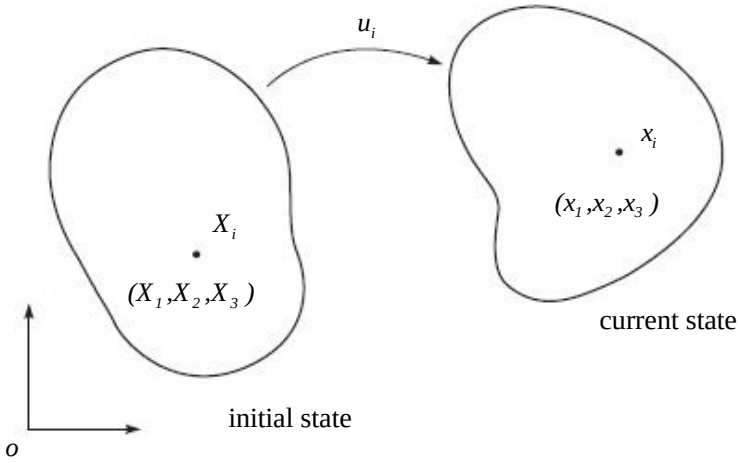

Figure 4.1 Reference and deformed configuration for finite deformation problems

In the theory of large deformation, the strain in a structure can't be expressed in the liner relation. The exact expression of the stress and strain adopted in large deformation is shortly reviewed here.

Surface traction or body force gives rise to movements and deformations in the body in Figure 4.1. When the position of any two points in continuous body is changed, it is called "deformed". The old coordinate X_i is linked to the new one x_i by Eq. (4.1),

$$x_i = X_i + u_i \tag{4.1}$$

Here displacement is written as u_i .

$$\text{£}_{ij} = \frac{1}{2}(u_{i,j} + u_{j,i}) \tag{4.2}$$

When displacement gradient components at a point are large, their symmetrical and skew-symmetric parts will not respectively represent pure deformation and rigid rotation of the point. Cauchy's strain in Eq. (4.2) should be replaced by more accurate and strict measurement with respect to both the initially

unreformed configuration X_i and the current deformed configuration x_i . The former is known as the Lagrangian strain formulation in Eq. (4.3), the latter is called Eulerian strain formulation in Eq. (4.4).

$$E_{ij} = \frac{1}{2}\left(\frac{\partial u_i}{\partial X_j} + \frac{\partial u_j}{\partial X_i} + \frac{\partial u_k}{\partial X_i}\frac{\partial u_k}{\partial X_j}\right) \tag{4.3}$$

$$e_{ij} = \frac{1}{2}\left(\frac{\partial u_i}{\partial x_j} + \frac{\partial u_j}{\partial x_i} - \frac{\partial u_k}{\partial x_i}\frac{\partial u_k}{\partial x_j}\right) \tag{4.4}$$

Thus, both the Lagrangian and Eulerian strains can return to Eq. (4.2) once the displacement gradient is small or can be negligible.

The term directly used in finite element formulation is not strain but the strain increment. Based on the analysis in Chen and Mizuno (1990), the Lagrangian strain incremental form directly obtained from deformation ratio part is usually preferable. The Lagrangian strain increment is also guaranteed to vanish when neighborhood particles rotate.

The definitions of stress and stress ratio for large deformation are reviewed here. The definition of stress as well as stress ratio changes in the large deformation formulation. In elastic mechanics, Eulerian stress dP_j in Eq. (4.5) is the infinitesimal force acting on the current surface element $dA_i = dAn_i$, n_i is the unit normal vector on the current surface dA .

$$dP_j = \pm_{ij} dAn_i \tag{4.5}$$

The first Piold-Kirchhoff stress tensor (Lagraingian stress tensor) is defined by referring to the reference surface element $d\overset{o}{A}_i = d\overset{o}{A}N_i$ in Eq. (4.6). Where, N_i is the unit normal vector on the reference surface.

$$dP_j = T_{ij} d \overset{o}{A} N_i \tag{4.6}$$

The second Piola-Kirchhoff stress tensor S_{ij} in Eq. (4.7) is defined to be the force per unit area of the deformed surface of a parallelepiped.

$$S_{ij} = \mathrm{J} \pm_{kl} \frac{\partial X_i}{\partial \pm_k} \frac{\partial X_j}{\partial \pm_l} \tag{4.7}$$

Since $\pm_{ij}$ is symmetric, S_{ij} is also a symmetric tensor. S_{ij} can be expressed in term of T_{ij} in Eq.(4.8), that is ,

$$T_{ij} = S_{ik} \frac{\partial x_j}{\partial X_k} \tag{4.8}$$

Generally, total Lagrangian (TL) and updated Lagrangian (UL) methods are regarded as the two primary technologies for solving large deformation problems in geomechanics. The major difference between these two methods is the reference configuration employed. The TL method refers to the initial configuration, while the UL method chooses to refer to the current configuration. The two methods are not two different solutions to the problem but rather two different approaches to the equilibrium equations.

The difficulties in defining the appropriate constitutive relation for use in large deformation analysis are attributed to the changing configuration of the body and the need for an appropriate objective stress rate. The stress rate used for a constitutive law must be invariant with respect to the rigid-body rotation. The material derivative $d\pm_{ij} / dt$ does not in general satisfy the invariance by a rigid-body rotation. The stress ratio such as Jaumann stress rate and Truesdell stress rate which are invariant with the rigid-body will be briefly introduced.

For the finite motion during time *dt*, the Jaumann stress increment $d\sigma_{ij}^{J}$ can be denoted as Eq. (4.9):

$$d\sigma_{ij}^{J} = d\sigma_{ij} - \sigma_{ik} d\Omega_{jk} - \sigma_{jk} d\Omega_{ik} \tag{4.9}$$

where $d\Omega_{jk}$ is the increment of the rotation tensor, the Jaumann stress increment $d\sigma_{ij}^{J}$ is related to the Eulerian stress $d\sigma_{ij}$.

The Truesdell stress incremental $d\sigma_{kl}^{T}$ for the finite deformation during the time *dt* can be written as:

$$d\sigma_{kl}^{T} = d\sigma_{kl}^{J} + d\varepsilon_{mm}\sigma_{kl} - d\varepsilon_{lm}\sigma_{km} - d\varepsilon_{km}\sigma_{lm} \tag{4.10}$$

The $d\sigma_{kl}^{T}$ in Eq. (4.10) becomes approximately equal to the increment of second Piola-Kirchhoff stress dS_{kl} when the displacement gradient $\partial u_i / \partial x_j$ is small compared with the unit.

The importance of stress rate chosen in the virtual work expression will be discussed later.

The state variables are assumed to satisfy the equilibrium condition from the initial time 0 to time t. The general expression of the virtual work at some intermediate time t is written in Eq. (4.11) as follows:

$$\int_A T_i^t \cent(du_i) dA^t + \int_V \circ^t F_i^t(x_j) \cent(du_i) dV^t = \int_V \pm_{ij}^t \cent(d\pounds_{ij}) dV^t \tag{4.11}$$

where T is the traction force, u is the displacement, F is the body force per unit mass, $\circ$ is the mass density of the initial state, $\cent$ is a virtual value, $\pm_{ij}$ is the Cauchy stress tensor and $\pounds_{ij}$ is the infinitesimal strain tensor. The state variables with superscript t denote the variables at intermediate time t.

$$\cent W_{ext} = \int_V \pm_{ij}^{t+\Delta t} \cent \pounds_{ij}^{t+\Delta t} dV = \int_{\overset{o}{V}} S_{ij}^{t+\Delta t} \cent E_{ij}^{t+\Delta t} d\overset{o}{V} \tag{4.12}$$

where $¢W_{ext}$ is the external work by the body force and traction force. The major difficulty in solving the large deformation and strain problem is determining the configuration in time $t+\Delta t$. To solve Eq. (4.12), all state variables must be linked to a known configuration at time t . It is concluded that the external work can be expressed in terms of either the cauchy stress tensor $\pm_{ij}$ and the virtual change $¢£_{ij}$ in infinitesimal strain tensor, or the second Piola-Kichhoff stress tensor S_{ij} and the virtual change $¢E_{ij}$ of the Lagrangian strain tensor. The TL method refers to the initial configuration at time 0,while the UL method employs the current configuration at time $t+\Delta t$. The difference is dependent on the specific forms of S_{ij} and $¢E_{ij}$ at time $t+\Delta t$.

4.1.2 Total Lagrangian method

The total Lagrangian formulation refers all measurements of forces, stresses, strains to the reference (undeformed) configuration.

$$dE_{ij} = E_{ij}^{t+dt} - E_{ij}^{t} \tag{4.13}$$

The expression of the Lagrangian strain in Eq. (4.13) is with respect to the reference coordinate system X_i in the initial configuration.

$$S_{ij}^{t+dt} = S_{ij}^{t} + dS_{ij} \tag{4.14}$$

The second Piola-Kichhoff stress tensor at time $t+\Delta t$ is written as Eq. (4.14).

Where dS_{ij} is the increment of second Piola-Kirchhoff stress which is related to the increments of Lagrangian strain dE_{ij} through in Eq. (4.15):

$$dS_{ij} = C^{*}_{ijkl} dE_{kl} \tag{4.15}$$

Where, C^{*}_{ijkl} is not the same constitutive relationship as used for small displacement analysis. Put Eq. (4.13), Eq. (4.14) and Eq. (4.15) into Eq. (4.12), the external work by the TL method is obtained.

4.1.3 Updated Lagrangian method

In practice, it is convenient to refer to either the initial or the most recent equilibrium configuration. The latter results in what is commonly referred to as the updated Lagrangian formulation. The updated Lagrangian formulation provides a choice of several stress rates, i.e., the Jaumann stress rate $d\sigma^{J}_{ij}$ in Eq. (4.16) is the most widely employed.

$$d\sigma^{J}_{ij} = d\sigma_{ij} - \sigma^{t}_{ik} d\Omega_{jk} - \sigma^{t}_{jk} d\Omega_{ik} \tag{4.16}$$

The relationship between the increments of deformation tensor $d\varepsilon_{kl}$ and the Jaumann stress increments $d\sigma^{J}_{ij}$ is commonly assumed to be as Eq. (4.17):

$$d\sigma^{J}_{ij} = C^{UL}_{ijkl} d\varepsilon_{kl} \tag{4.17}$$

where C^{UL}_{ijkl} may be taken the same as that for small strain analysis.

The updated Lagrangian formulation makes use of the incremental decomposition f the stresses in the form, the second Piola-Kirchhoff stress at time $t + \Delta t$ is expressed as Eq. (4.18):

$$S^{t+dt}_{ij} = S^{t}_{ij} + dS_{ij} = \sigma^{t}_{ij} + dS_{ij} \tag{4.18}$$

where the second Piola-Kirchhoff stresses S^{t}_{ij} at time t are identical to the Eulerian stresses σ^{t}_{ij}, and

the second Piola-Kichhoff stress increment dS_{ij} becomes the Truesdell stress increments $d\sigma_{ij}^{T}$ expressed by Eq. (4.19), that is:

$$\begin{aligned} dS_{ij} &= d\pm_{ij}^{J} + d\pounds_{kk}\pm_{ij}^{t} - d\pounds_{jk}\pm_{ik}^{t} - d\pounds_{ik}\pm_{jk}^{t} \\ &= C_{ijkl}^{**} dE_{kl} \end{aligned} \tag{4.19}$$

The relationship between the dS_{ij} and dE_{ij} is rewritten in Eq. (4.19). Where C_{ijkl}^{**} is not the same constitutive relationship as for small displacement analysis. The second Piola-Kichhoff stress S_{ij}^{t+dt} which are measured with respect to the configuration at time $t+\Delta t$ must be transformed to obtain true Eulerian stress $\pm_{ij}^{t+dt}$ in Eq. (4.20)

$$\pm_{ij}^{t+dt} = \pm_{ij}^{t} + dS_{ij} \tag{4.20}$$

Put Eq. (4.13), Eq. (4.19) and Eq. (4.20) into Eq. (4.12), the external work by the UL method is obtained.

4.2 A mixed method for the UL method

It is noted that the equations of continuum mechanics can be posed in Eulerian or Lagrangian form. Briefly, in a Lagrangian formulation all quantities are referred to coordinates associated with some reference configuration, the undeformed configuration of the body. In an Eulerian coordinates are referred to coordinates associated with the current configuration of the body. Lagrangian and Eulerian coordinates are sometimes referred to as material and spatial coordinates respectively.

We differentiate now between a Lagrangian incremental formulation, an Eulerian incremental

formulation and a mixed incremental formulation. Both the Lagrangian and mixed incremental equations employ a known material reference state. The reference state used in the Largrangian incremental approach is the same for all increments and is usually the undeformed, unstressed state of the body. The reference state employed in the mixed formulation is the current spatial configuration of the body, and this reference state is updated following each incremental step. A pure Eulerian equations is obtained by taking the first variation of the nonlinear Eulerian equations.

When presenting an incremental formulation, one must first of all be careful to differentiate between Eulerian, Lagrangian and mixed approaches. Secondly, in the context of large rotations and deformations, “stress” and “strain” must be precisely defined. Finally, an incremental formulation is not complete until one has described fully the procedures for progressing from increment to increment.

To formulate the equations governing an increment of deformation we consider two different configurations of the body, an initial configuration and a subsequent configuration. The stresses, strains and displacements in the initial configuration are presumed known and have been determined through a sequence of incremental steps. The subsequent configuration is reached through a further increment of deformation, and it is the incremental stresses, strains and displacements that we wish to determine.

To directly employ the constitutive relationship of small strain theory and make the integration of stress and strain for small strain and displacement, a mixed incremental formulation for the UL method is proposed. The Lagrangian strain incremental employs the same expression in Eq. (4.13), but with more specific form in Eq. (4.16).

$$dE_{ij} = \frac{1}{2}(du_{i,j} + du_{j,i} + du_{k,i}du_{k,j}) \tag{4.21}$$

$$du_{i,j} = d\varepsilon_{ij} + d\Omega_{ij} \tag{4.22}$$

$$d\Omega_{ij} = (u_{i,j} - u_{j,i})/2 \tag{4.23}$$

where $du_{i,j}$ in Eq. (4.22) is composed of the Cauchy strain tensor and spin tensor, $d\varepsilon_{ij}$ is the Cauchy strain tensor for infinitesimal strain and $d\Omega_{ij}$ is the spin tensor from Eq. (4.23). Inserting Eq. (4.22) and Eq. (4.23) into Eq. (4.21) results in Eq. (4.24) as follows:

$$dE_{ij} = d\varepsilon_{ij} + \frac{1}{2}(d\varepsilon_{ki} + d\Omega_{ki})(d\varepsilon_{kj} + d\Omega_{kj}) \tag{4.24}$$

In the external work equation, the stress and strain tensors always appear in pairs. It is noted that $d\sigma_{ij}$ is equal to the Jaumann stress increment $d\tau_{ij}^{J}$. $d\sigma_{ij}$ is obtained from the following general form by Davidson and Chen (1974) in Eq. (4.25).

$$d\sigma_{ij} = D_{ijkl}^{ep} d\varepsilon_{kl} \tag{4.25}$$

where, D_{ijkl}^{ep} is the elastic-plastic constitutive tensor expressed in terms of the Cauchy stress tensor.

It is necessary to express the increments of the second Piola-Kichhoff stress dS_{ij} in terms of $d\tau_{ij}$, σ_{ij} and $d\varepsilon_{ij}$ so that it can be linearized to the equation for large strain and deformation. The second Piola-Kichhoff stress increment dS_{ij} related to the Jaumann stress increment $d\tau_{ij}$ to the first order is generally writen as:

$$dS_{ij} = d\sigma_{ij} + \cdot_{ijkl} d\varepsilon_{kl} \tag{4.26}$$

It is necessary to express the increments of the second Piola-Kichhoff stress dS_{ij} in Eq. (4.26). The second Piola-Kirchhoff stress increment $d\sigma_{ij}$ related to the Jaumann stress increment dS_{ij} is generally written in Eq. (4.26)

Combining Eq. (4.20), Eq. (4.25) and Eq. (4.26) yields Eq. (4.27), an expression for the second Piola-Kirchhoff stress S_{ij} at time $t+\Delta t$, as follows:

$$S_{ij}^{t+dt} = \pm_{ij}^{t} + (C_{ijkl}^{ep} + \cdot_{ijkl}) d\pounds_{kl} \tag{4.27}$$

Inserting Eq. (4.27) and the incremental form of Eq. (4.24) into Eq. (4.12), the external virtual work expression in terms of the Cauchy stress and strain tensor is obtained in Eq. (4.28) as follows:

$$\begin{aligned} &\int_V \pm_{ij} \left\{ d\pounds_{ki} ¢ \left(d\pounds_{kj} \right) + d\pounds_{ki} ¢ \left(d\Omega_{kj} \right) + d\Omega_{ki} ¢ \left(d\pounds_{kj} \right) + d\Omega_{ki} ¢ \left(d\Omega_{kj} \right) \right\} dV \\ &+ \int (d^2_{ij} + \cdot_{ijkl} d\pounds_{kl}) ¢ (d\pounds_{ij}) dV \\ &= \int_A (T_i + dT_i) ¢ u_i dA + \int_V °_o \left\{ F_i (x_j + dF_i) \right\} ¢ \left(du_i \right) dV - \int_V \pm_{ij} ¢ \pounds_{ij} dV \end{aligned} \tag{4.28}$$

The large deformation theory is integrated with the finite element analysis of pile loading test. The pile is generally treated as the axis-symmetric structure. For convenient integration using the finite element method, Eq. (4.28) has been transformed into the matrix formulation as Eq. (4.29).

$$\left(\sum \left[k_g \right] \right) \{ dU \} + \left(\sum \left[k_m \right] \right) \{ dU \} = \{ dR \} \tag{4.29}$$

In which the matrices $\left[k_g \right]$ and $\left[k_m \right]$ are the geometrical nonlinearity and material nonlinearity element matrix stiffness. The specific expressions are given by Eq. (4.30) and Eq. (4.31) respectively. Where $\{ dR \}$ is the external force vector, $\{ dU \}$ is the displacement vector.

$$\left[k_g \right] = \int_V \left[B_L^* \right]^T [A] \left[B_L^* \right] dV \tag{4.30}$$

$$[k_m] = \int_V [B_L]^T ([D] + [\cdot]) [B_L] dV \tag{4.31}$$

The transformation relationship in Eq. (4.30) between the $\{d\varepsilon^*\}$ and displacement vector $\{dU\}$ is written in Eq. (4.32). The expression of the matrix $[B_L^*]$ is shown in Eq. (4.33).

$$\{d\varepsilon^*\} = \lfloor d\varepsilon_{11} \quad d\varepsilon_{22} \quad d\varepsilon_{33} \quad d\gamma_{12} \quad d\Omega_{12} \rfloor^T = [B_L^*]\{dU\} \tag{4.32}$$

$$[B_L^*] = \frac{1}{2A}\begin{bmatrix} b_1 & 0 & b_2 & 0 & b_3 & 0 \\ 0 & c_1 & 0 & c_2 & 0 & c_3 \\ L_1/x & 0 & L_2/x & 0 & L_3/x & 0 \\ c_1 & b_1 & c_2 & b_2 & c_3 & b_3 \\ \frac{1}{2}c_1 & -\frac{1}{2}b_1 & \frac{1}{2}c_2 & -\frac{1}{2}b_2 & \frac{1}{2}c_3 & -\frac{1}{2}b_3 \end{bmatrix} \tag{4.33}$$

Where the coordinate $L_1 = A_1 / A$ and $L_2 = A_2 / A$. A , A_1 and A_2 the area of triangular element and subareas. The transformation relationship in Eq. (4.31) between the $[B_L]$ and displacement vector $\{dU\}$ is written in Eq. (4.34). The expression of the matrix $\{d\varepsilon\}$ is shown in Eq. (4.30)

$$\{d\varepsilon\} = \lfloor d\varepsilon_{11} \quad d\varepsilon_{22} \quad d\varepsilon_{33} \quad d\gamma_{12} \rfloor^T = [B]\{dU\} \tag{4.34}$$

$$[B_L] = \frac{1}{2A}\begin{bmatrix} b_1 & 0 & b_2 & 0 & b_3 & 0 \\ 0 & c_1 & 0 & c_2 & 0 & c_3 \\ L_1/x & 0 & L_2/x & 0 & L_3/x & 0 \\ c_1 & b_1 & c_2 & b_2 & c_3 & b_3 \end{bmatrix} \tag{4.35}$$

$[\cdot]$ and $[A]$ are the matrixes used in the composition of the Cauchy stress, σ_{ij} , shown in Eq. (4.36) and Eq. (4.37) for the axially symmetric stress field. The terms for rigid body motion are included in Eq. (4.31). The constitutive matrix, $[D]$, is determined from the constitutive model for sand with particle crushing described in the Chapter 3.

$$[\cdot] = \begin{bmatrix} -\sigma_{rr} & \sigma_{rr} & \sigma_{rr} & -\sigma_{rz} \\ \sigma_{zz} & -\sigma_{zz} & \sigma_{zz} & -\sigma_{rz} \\ \sigma_{\theta\theta} & \sigma_{\theta\theta} & -\sigma_{\theta\theta} & 0 \\ 0 & 0 & \sigma_{rz} & -\frac{1}{2}(\sigma_{rr}+\sigma_{zz}) \end{bmatrix} \tag{4.36}$$

$$[A]=\begin{bmatrix} \pm_{rr} & 0 & 0 & \frac{1}{2}\pm_{rz} & \pm_{rz} \\ 0 & \pm_{zz} & 0 & \frac{1}{2}\pm_{rz} & -\pm_{rz} \\ 0 & 0 & \pm- & 0 & 0 \\ \frac{1}{2}\pm_{rz} & \frac{1}{2}\pm_{rz} & 0 & \frac{1}{4}(\pm_{rr}+\pm_{zz}) & \frac{1}{2}(\pm_{zz}-\pm_{rr}) \\ \pm_{rz} & -\pm_{rz} & 0 & \frac{1}{2}(\pm_{zz}-\pm_{rr}) & \pm_{rr}+\pm_{zz} \end{bmatrix} \tag{4.37}$$

Consequently, in this mixed incremental method, the stress and strain integrations can be performed in a manner similar to that used for the small deformation problem. Because the soil around pile experience large deformation and rotation, the general incremental finite-element equations with large deformation and rotation for the analysis of soil response is derived.

4.3 Joint element model

It is well known that interfaces often play a major role in the mechanical behavior of structures interacting with soil. The soil-pile interaction is typical in that the soil is in contact with the engineered structure. In this study, the emphasis is on the contact behavior between the sand and the pile. Consequently, it is necessary to employ a suitable constitutive relationship to model the heavily loaded interacting region.

A number of models have been presented to describe the interface behavior between the soil and a rigid structure. Among them, Goodman et al. (1968) was the pioneer in establishing the constitutive modeling at the interface or at the rock joints. The model for the joint element is shown in Figure 4.2. The four-node joint element with zero-thickness assumes a linear relationship between the stress and the relative displacement at the interface in Eq. (4.38) as follows:

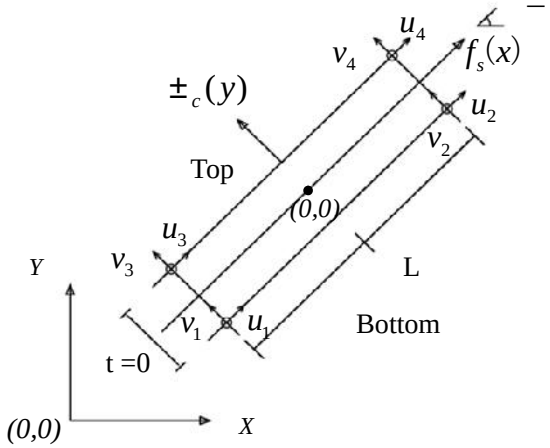

Figure 4.2 Concept of joint element

$$\begin{Bmatrix} f_s \\ \sigma_c \end{Bmatrix} = \begin{bmatrix} k_s & 0 \\ 0 & k_c \end{bmatrix} \begin{Bmatrix} \Delta u \\ \Delta v \end{Bmatrix} \qquad (4.38)$$

In Eq. (4.38), f_s is the shear stress, $\pm_c$ is the compression stress, k_s and k_c are the tangential and normal stiffness per unit length along the interface, respectively, Δv and Δu represent tangential and normal relative displacement, respectively. The line 1-3 and line 2-4 are straight lines. The nodes 1 and 3, 2 and 4 are in coincident position before deformation. In the finite element analysis, node 1 and 3, 2 and 4 employ the same coordinates. They can be approximated using linear interpolation functions N_1 and N_2 in Eq. (4.39), where $N_1=1-2x/L$ and $N_2=1+2x/L$. Horizontal and vertical nodal displacements are expressed in matrix form as $\{u\}=\{u_1 \;\; 0 \;\; u_2 \;\; 0 \;\; u_3 \;\; 0 \;\; u_4 \;\; 0\}^T$ and $\{v\}=\{0 \;\; v_1 \;\; 0 \;\; v_2 \;\; 0 \;\; v_3 \;\; 0 \;\; v_4\}^T$.

$$\{w\} = \begin{Bmatrix} \Delta u \\ \Delta v \end{Bmatrix} = \begin{Bmatrix} w_s^{top} - w_s^{bottom} \\ w_n^{top} - w_n^{bottom} \end{Bmatrix} = \frac{1}{2} \begin{bmatrix} -N_1 & 0 & -N_2 & 0 & N_2 & 0 & N_1 & 0 \\ 0 & -N_1 & 0 & -N_2 & 0 & N_2 & 0 & N_1 \end{bmatrix} \begin{Bmatrix} u \\ v \end{Bmatrix} \qquad (4.39)$$

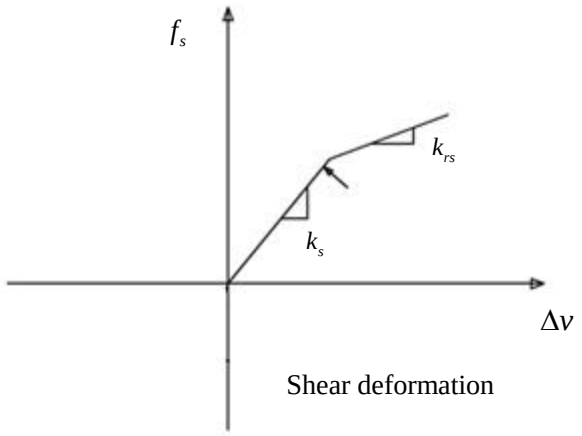

Figure 4.3 Constitutive laws for shear deformation of joint element

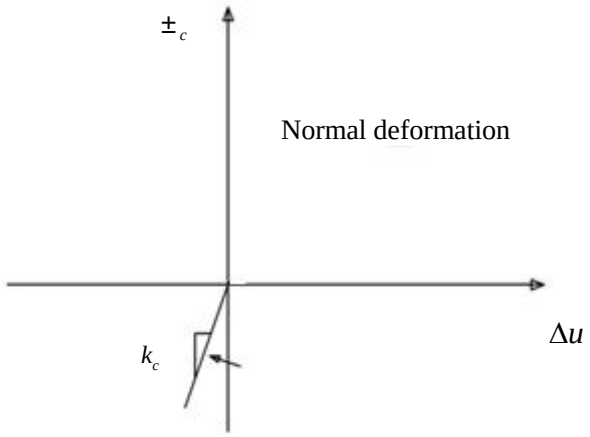

Figure 4.4 Constitutive laws for compressive deformation of joint element

The special rule, shown in Figure 4.3 and Figure 4.4, is needed to identify the four modes of joint element deformation, i.e., contact, slip, de-bonding and re-bonding, described by Li (1993). In the contact mode, if the shear stress, k_s , reaches the yield stress, k_{rs} , the sliding condition is assumed to be controlled by the Mohr-Coulomb failure criterion and slip occurs. The value of k_s is equal to k_{rs}

if slip occurs. For simplicity, the relationship of the joint element can be assumed to be perfect elasto-plastic (σ_c is equal to 0). In the mode of de-bonding and re-bonding, if the normal stress, k_{rs} , is tensile, the coefficients k_c and k_s are equal to zero. The parameters of the joint element are adapted from the experiments performed by Uesugi and Kishida (1986) and Uesugi and Kishida (1987). The three parameters are given in Table 4.1, where « is the friction coefficient.

The local coordinate system, (x,y), can be directly converted into the global coordinate system, (X,Y) , using a transformation matrix consisting of the rotation angle ¯ , shown in Eq. (4.40). The joint elements are placed at the interface between soil and the pile.

$$\begin{bmatrix} x \\ y \end{bmatrix} = \begin{bmatrix} \cos\theta & \sin\theta \\ -\sin\theta & \cos\theta \end{bmatrix} \begin{bmatrix} X \\ Y \end{bmatrix} \tag{4.40}$$

Table 4.1 The parameters of the joint element

Joint element	Shear coefficient	Compression coefficient	Friction Coefficient
Parameter	$K_s=300N/cm^3$	$K_c=10^5N/cm^3$	«= 0.45

4.4 Summary

The finite element analysis using large deformation theory is an effective method to predict the pile penetration and loading problem. A mixed incremental method for UL method is reviewed and detailed explained in this chapter. The constitutive model for small deformation theory is directly employed in

this mixed incremental method and the integration process of stress and strain is equal to that of small deformation theory. This theory system is suitable for the behavior of structure with large deformation and large rotation. The axis-symmetric finite element formulation is obtained and convenient to implement the numerical analysis.

The zero-thickness joint element is adopted to simulate the interactive behavior between the granular sand and the pile. The joint element is capable of describing the compression, sliding and crack behavior.

Reference

Chen, W. F. and Mizuno, E. “Nonlinear analysis in soil mechanics: Theory and Implementation”. Nertherlands, ELSEVIER ,1990.

Davidson, H. L. and Chen, W. F. (1974). “Elastic-Plastic large deformation response of clay to footing loads”. 355.18, Fritz Eng. Lab. Leihigh university, PA,181.

Goodman, R.E., and Taylor, R. L. (1968). “A model for the mechanics of jointed rock”. Journal of the Soil Mechanics and Foundation Division, 94(SM3), 637-659.

Hu, Y., and Randolph, M. F. (1998a). “A practical numerical approach for large deformation problems in soil”. International Journal for Numerical and Analytical Methods in Geomechanics, 22(5), 327-350.

Hu, Y., and Randolph, M. F. (1998b). “H-adaptive FE analysis of elasto-plastic non-homogeneous soil with large deformation”. Computers and Geotechnics, 23(1), 61-83.

Kiousis, P. D., Voyiadjis, G.Z. and Tumay, M.T. (1986). “A Large Strain Theory for the Two Dimensional Problems in Geomechanics”. International Journal for Numerical and Analytical Methods in Geomechanics, 10(1), 17-39.

Kiousis, P. D., Voyiadjis, G.Z. and Tumay, M.T. (1988). “A Large Strain Theory and its Application in the Analysis of the Cone Penetration Mechanism”. International Journal for Numerical and Analytical Methods in Geomechanics, 12(1), 45-60.

Li, J. C. (1993). “Numerical Simulation of Interfaces in Geomaterials: Development of New Zero-Thickness Interface Elements”. Doctor thesis, University of Delaware, 15-27.

Nazem, M., Sheng, D. C. and Carter, J. P. (2006). “Stress integration and mesh refinement for large deformation in geomechanics”. International Journal for Numerical Method in Engineering, 65(7),

1002-1027.

Nazem, M., Sheng, D. C., Carter, J. P. and Sloan, S. W. (2008). “Atbitrary Lagrangian-Eulerian method for large-strain consolidation problems”. International Journal for numerical and methods in geomechanics, 32(9), 1023-1050.

Nazem, M., Carter, J.P. and Airey, D. (2009). “Arbitrary lagrangian-Eulerian method for dynamic analysis of geomechnical problems”. Computers and Geotechnics, 36(4), 579-557.

Nazem, M., Cater, J. P. and Airey, D. W. (2010). “Arbitrary lagrangian-Eulerian method for non-linear problem of geomechanics”. Proceeding of the 9th World Congress on Computational Mechanics and 4th Asian Pacific Congress on Computational Mechanics, Sydney, 10, 1-10.

Qiu, G., Henke, S. and Grabe, J. (2011a). “Application of a coupled Eulerian-Lagrangian approach on geomechanical problems involving large deformations”, Computers and Geotechnics, 38(1), 30-39.

Qiu, G. and Henke, S. (2011b). “Controlled installation of spudcan foundations on loose sand overlying weak clay”. Marine Structures, 24, 528-550.

Qiu, G. and Grade, J. (2012). “Numerical investigation of bearing capacity due to spudcan penetration in sand overlying clay”. Canadian Geotechnical Journal, 49(12), 1393-1407.

Sheng, D. C., Eigenbrod, K. D. and Wriggers, P. (2005). “Finite element analysis of pile installation using large-slip frictional contact”. Computers and Geotechnics, 32(1), 17-26.

Sheng, D. C., Yamamoto, H. and Wriggers, P. (2008). “Finite element analysis of englarged end piles using frictional contact”. Soils and Foundations, 48(1), 1-14.

Sheng, D. C., Nazem, M. and Carter, J. P. (2009). “Some computational aspects for solving deep penetration problems in geomechanics”. Computational Mechanics, 44(4), 549-561.

Uesugi, M., and Kishida H. (1986). “Influential Factors of friction between Steel and Dry sands”. Soils

and Foundations, 26(2), 33-46.

Uesugi, M., and Kishida, H. (1998). “Behavior of sand particles in sand-steel friction”. Soils and Foundations, 28(1), 107-118.

Vavourakis, V., Loukidis, D., Charmpis, D. C. and Papanastasiou, P. (2013). “Assessment of remeshing and remapping strategies for large deformation elastoplastic Finite element analysis”. Computers and Structures, 144, 133-146.

CHAPTER 5

NUMERICAL ANALYSIS OF SOIL BEHAVIOUR AROUND PILE TIP

The features of the material and geometrical nonlinearities are introduced in Chapters 3 and 4 respectively. This study presents the numerical analysis of the model pile loading in sand under three levels of surcharge pressure. The confined effect of the model ground size on the bearing stress of model pile is discussed. The distributions of the stress and strain contours are beneficial of understanding the soil deformation and behavior around pile tip. In this chapter, the former discussion portion is confined in small strain theory in this chapter. The latter portion represents the numerical results from both small and large deformation theory respectively and the deformed meshing elements at different penetration depths.

5.1 Outline of the pile loading test

5.1.1 Description of test

In the model pile loading tests conducted by Yamamoto et al. (2003), the model piles were jacked into the ground tank container which is filled with Toyoura sand in order to demonstrate the effects of pile tip shape and surcharge pressure level on the bearing capacity, and to study the movement of sand particles around the pile tip area. The testing apparatus is shown in Figure 5.1 which consists of the ground tank container, loading installation and measurement part.

The model ground tank container is 550 mm in height and 584.2 mm in radius. The diameters of steel model pile are employed as 30 mm and 54 mm in respective in Figure 5.2. The diameter ratio of ground

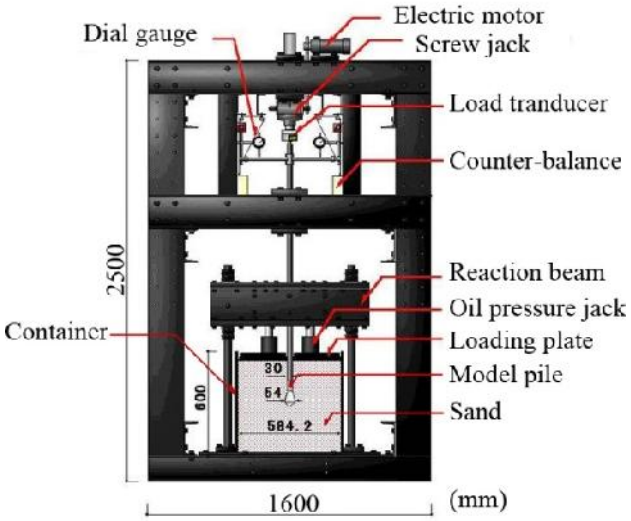

Figure 5.1 The testing apparatus

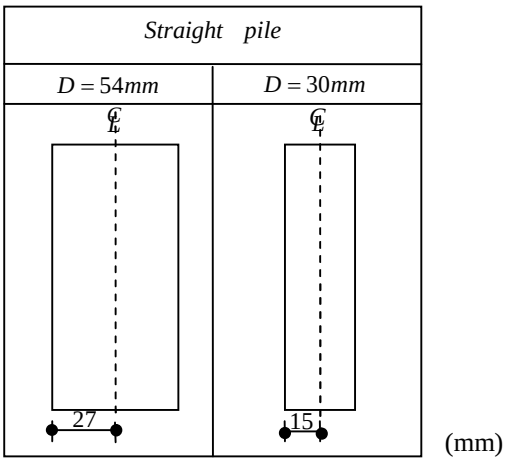

Figure 5.2 The model piles

tank container to steel model pile is deliberately adjusted to weaken the reaction from the interior surface of the ground tank container. Toyoura sand is poured into the ground tank container layer by layer to be well-distributed and homogeneous after model pile is installed in previous. The relative density of the dense uniform Toyoura sand is approximately 90%. The physical and material parameters of Toyoura sand are listed in detail in Table 5.1. In addition, the influence of pile installation on bearing capacity is neglected. Teflon sheets and silicon-grease are pasted onto the interface between the ground

Table 5.1 Properties of Toyoura sand for testing

Mean grain size (mm)	0.20
Coefficient of uniformity	1.21
Specific gravity	2.656
Minimum density (g/cm^3)	1.332
Maximum density (g/cm^3)	1.646
Relative density (%)	90
Internal friction angle	44.0°

tank container and Toyoura sand to eliminate the effect of fictional stress.

The model pile loading test is performed with displacement-controlled method. The descending speed of the model pile into sand layer is 0.5 mm/min. The final displacement of the model pile is equal to its diameter. The loading transforms into the sand layer and simulates the actual soil stress underground. Three levels of surcharge pressure 200 kPa, 400 kPa and 600 kPa simulate the actual soil stresses at different depths the model pile embedded into.

In order to confirm the occurrence of particle crushing in the test, the grain size distribution curves for the Toyoura sand before and after model pile loading test are measured by Li and Yamamoto (2005) in Figure 5.3. The part of sand ground for sieve analysis test is a cube column with a pile diameter equal to the side length just beneath the pile tip. The intact sample of sand block is carefully taken off after test completion. The characteristics of the model ground material and the axi-symmetric loading conditions of Li's experiment are identical to the current study. As of the above reasons, the figure is directly cited to prove particle crushing occurrence. As shown in Figure 5.3, sand particle become finer with larger surcharge pressure. Before test, the sand particle passing sieve diameter 0.1mm is less than 5%, however, the percent of sand particle passing 0.1 mm is nearly 15% after tests at the surcharge

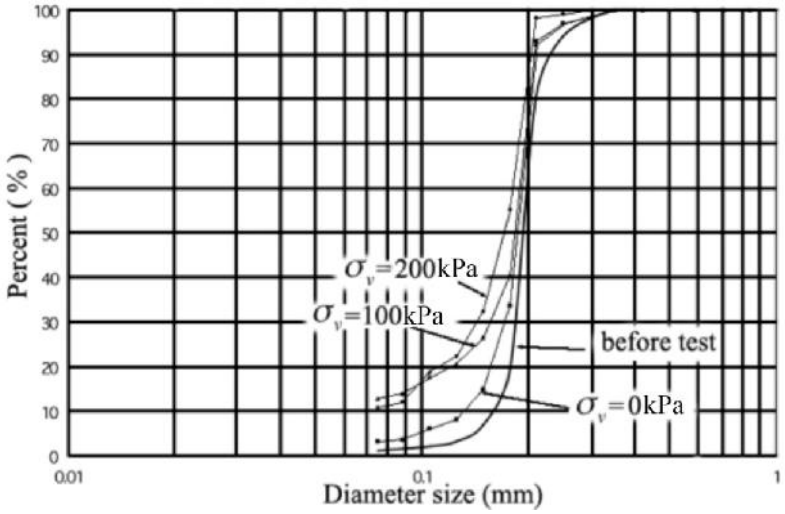

Figure 5.3 Distribution curves of sand grain size

pressure of 100 kPa and 200 kPa. Particle crushing of soil definitely occurs at the area surrounding the pile tip.

5.1.2 Meshing

Pile is generally modelled as axi-symmetric structure for analytical convenience. The whole analysis area is the model ground tank container, 300 mm in radial and 550 mm in height in Figure 5.4 (a). The surcharge pressures acting on the upper surface of model ground simulate the actual soil stress in different depths. The boundary constrained condition for model ground is set in corresponding to the model pile loading test setup. The basic physical features of Toyoura sand in triaxial compression test and the ground material in the model pile loading tests are the same as the specimen material of test performed by Sun et al. (2007). Therefore, it is believed that values of the seven parameters are reliable for the numerical analysis of model pile loading test. The meshing in the case of model pile with flat base is shown in Figure 5.4 (b). The behaviour of sand ground is represented by the constitutive model

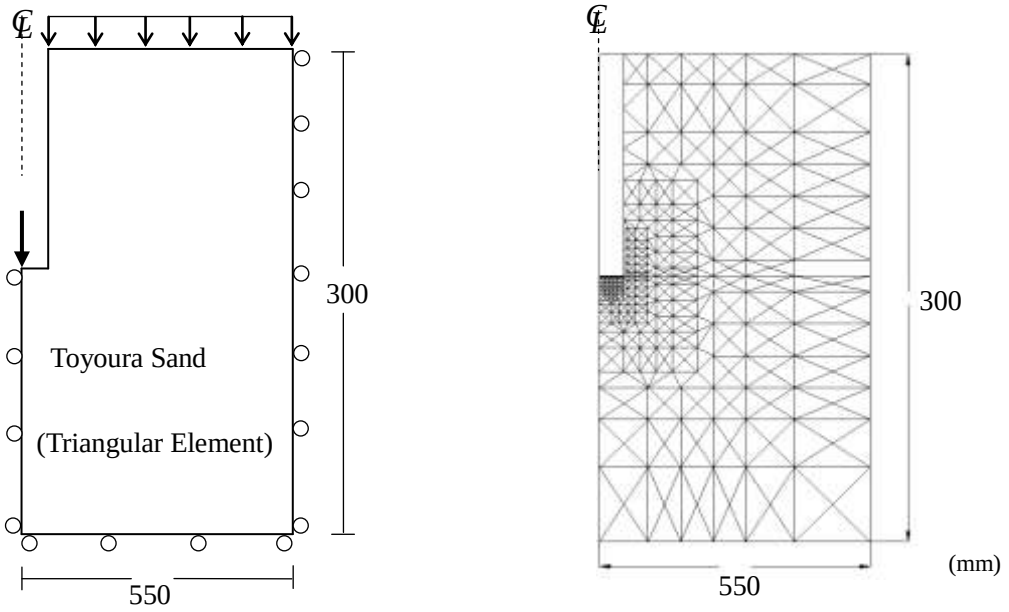

(a) Area of modelling (b) Meshing

Figure 5.4 Element meshing

considering particle crushing. Joint element is applied to simulate the interface behaviour during pile loading process. The joint elements are placed on the pile shaft and pile tip. For calculation simplicity, the meshing work was finished by using three nodal triangular elements. The numerical calculations have been conducted by the displacement-controlled method. The displacement control points are at the bottom of the pile tip and all control points descend simultaneously. The displacement is added by equivalent increment. The final displacement is equal to the shaft diameter of pile in each calculation step.

5.1.3 The confining effect of the model ground

The bearing capaity of model pile in laboratory test is affected by the confining pressure from the model tank container. In reference to model pile embedded into tank ground, the confined effect can be

deal with adjusting the diameter ratio of tank and pile. The theoretical computation is conducted to investigate the confined effect. In such test installation, the confined effect is reacted by ground tank interior surface. *d* is the diameter of model ground tank, while *D* is the pile diameter. In order to comprehend confined effect of model test, the scale ratio is defined as R=d/D. The height of the model ground H_e is 550 mm, and the diameter d is 600 mm. When the diameter ratio of tank to pile R is small, the confined effects become heavier. It is believed that there exists a critical diameter ratio value even the diameter ratio increases; the confined effect can be ignored. The normalized bearing stress is given as $\pm_b / \pm_{sur}$. $\pm_b$ is the bearing stress of soil element beneath pile tip and $\pm_{sur}$ is the surcharge pressure stress acted on the top surface of model ground in Figure 5.5. In this parametric study, *d* is fixed as 600 mm and D varies from 7.5 mm, 15 mm, 30 mm, 60 mm, 120 mm. here, S means pile tip settlement. All the five cases standing for different displacements are computed with the same method. Moreover, in one curve, five concrete spots mean various scale ratio cases. Constrain the analysis to the small deformation so as to ensure computation accuracy; the final displacement is set to

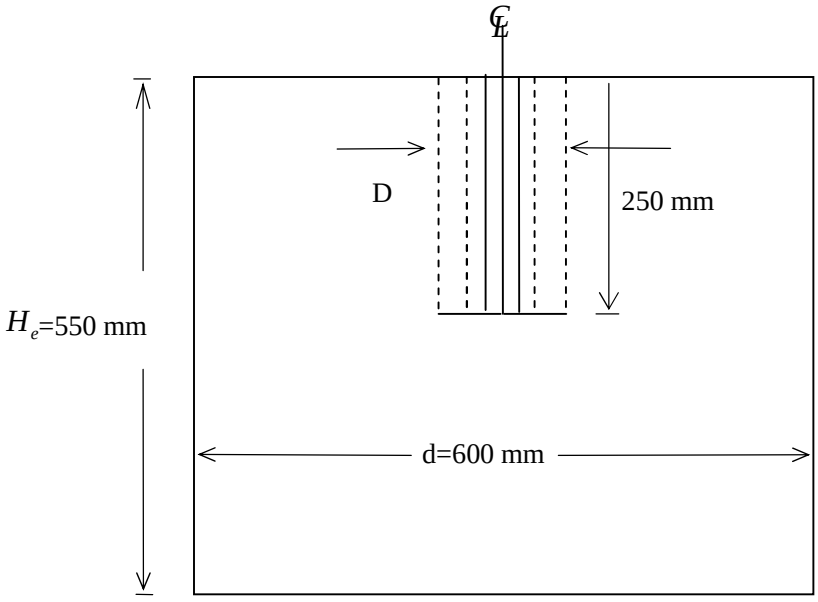

Figure 5.5 Model pile with different diameters

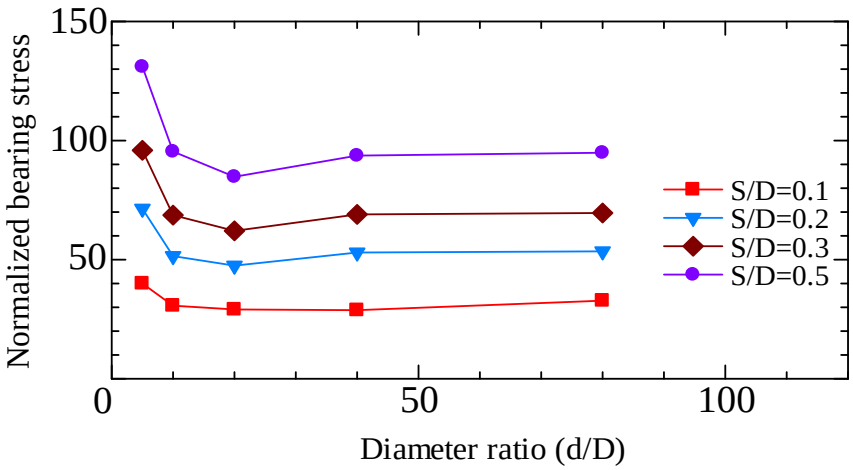

(a) The surcharge pressure is 200 kPa

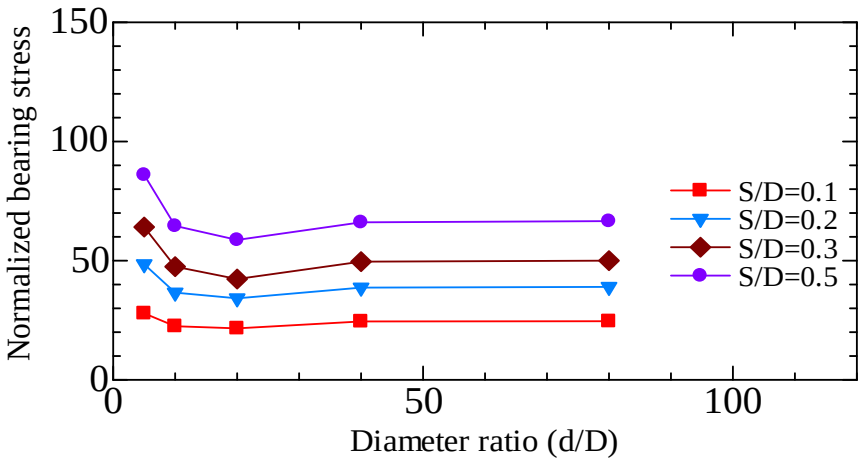

(b) The surcharge pressure is 400 kPa

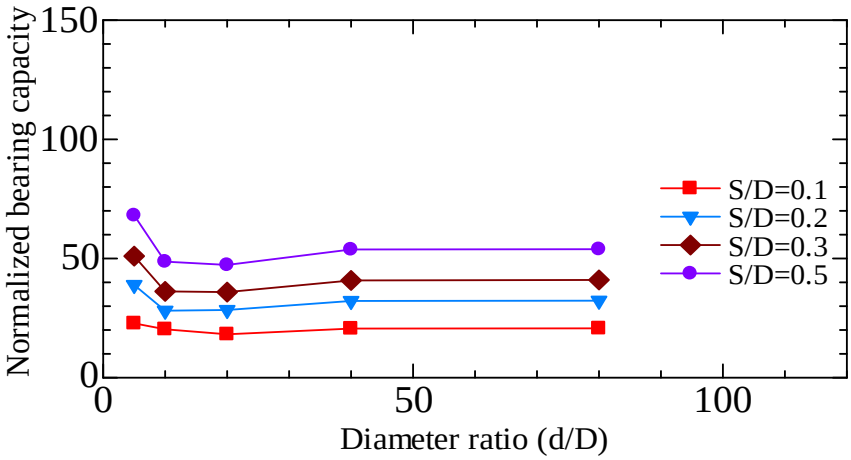

(c) The surcharge pressure is 600 kPa

Figure 5.6 The relationship between the normalized bearing stress and diameter ratio

be pile semidiameter. From the curves in Figure 5.6 (a), (b) and (c), when diameter ratio is less than 10, the confined effect is serious and calculation is incredible. Inversely, once diameter ratio R is larger than 20, prediction curves will slightly fluctuate.

Three surcharge stresses test figures almost shows he same tendency in Wu and Yamamoto (2011a, 2011b). It is found that the reasonable scale ratio R should be confined between 10 and 15 to restrain confined effects under the same surcharge pressure stress.

5.2 Relationship between the normalized bearing stress and displacement

The numerical and experimental results of the normalized bearing stress and displacement are compared in this study. Herein, the normalized bearing stress is defined by a ratio of current bearing stress of the element beneath pile tip to surcharge pressure acted on the upper surface of model ground. While the normalized displacement is often adopted in analysis, it is defined as the ratio of current displacement (S) to pile diameter (D). Predicted values by numerical analysis of pile with diameters 30 mm and 54 mm are compared with experimental results in Figure 5.6 and Figure 5.7, respectively. It indicates that the predictions are agreeable with experimental results during the entire loading process under each surcharge pressure. Li and Yamamoto (2005) also attempted to predict the relationship between the normalized bearing stress and displacement of model piles. The predicted result was only agreeable with test results when the normalized displacement was smaller than 0.5. The prediction largely overestimated test result once displacement of pile was larger. The accuracy of prediction is improved by the numerical results incorporating the mechanical characteristics of particle crushing into the constitutive model.

It is interesting to observe that the normalized bearing stress decreases oppositely when the surcharge pressure increase. It can be explained that the amount of sand particles are forced to be crushed under higher surcharge pressure. The reduction of sand strength is attributed to the particle crushing occurrence. It is noted that the predicted values slightly overestimate the actual experimental results as

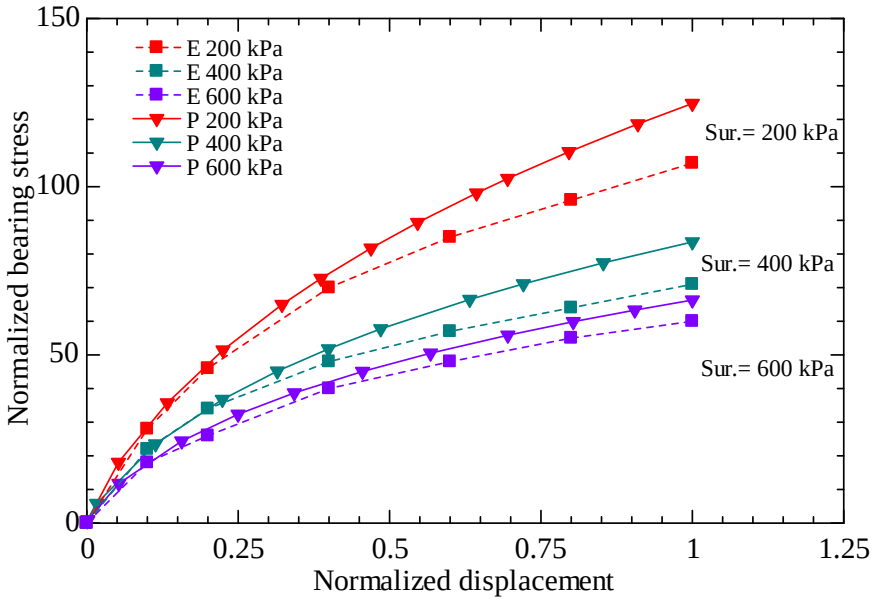

Figure 5.7 Relationship between normalized bearing stress and normalized displacement for pile diameter of 30 mm

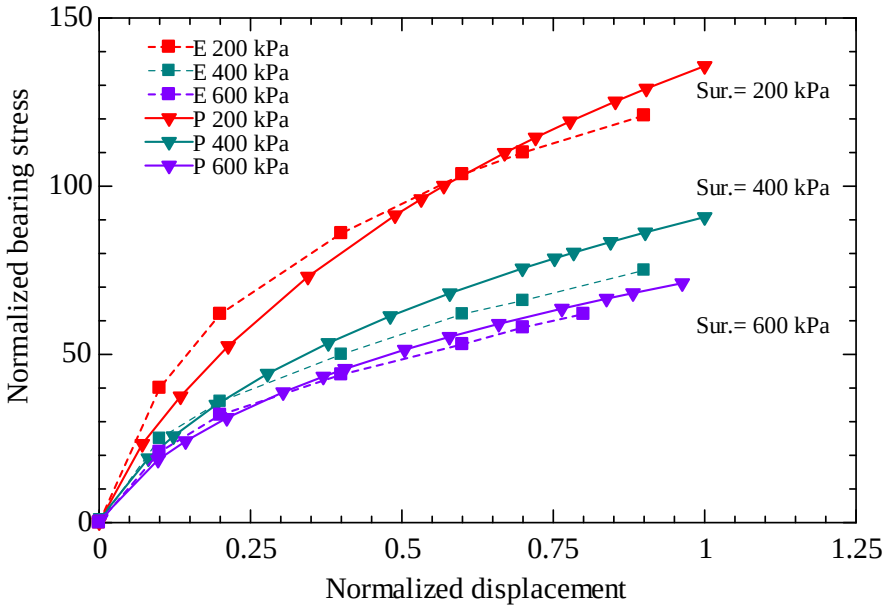

Figure 5.8 Relationship between normalized bearing stress and normalized displacement for pile diameter of 54 mm

shown in Figure 5.7 and Figure 5.8. The predicted discrepancy when the surcharge pressure as 200 kPa is owing to the unremarkable particle crushing. The constitutive model for sand with particle crushing overestimates the strength of sand in low level stress region.

From the comparison of curves between Figure 3.6 and Figure 5.7 or Figure 5.8, the same kind of relationship of the normalized bearing stress-displacement can be observed and some further relationship should be researched. In Figure 3.4, the vertical axis means the stress ratio of vertical stress to radius stress. The horizontal axis means the axial strain. Similarly in Figure 5.7 or Figure 5.8, the vertical axis stands for the normalized bearing stress in Figure 5.7. The horizontal axis means the normalized displacement with the same expression of axial strain. These two normalized bearing stress-displacement curves are identical in nature. Once the confining stress increases, the normalized bearing stress decreases on the contrary. The deceasing tendency of the normalized bearing stress is related to the particle crushing. It is satisfactory that the predicted values are close to the experiential results during the entire loading process. It is obvious that the pile with larger diameter 54mm owns much larger bearing stress. It is clear that the interior surface of the ground tank whose size is fixed will provide higher resistance when the diameter of pile becomes larger.

Apart from the numerical calculation method of the pile tip bearing capacity, a common approach of theoretical nature to determination of the ultimate end bearing capacity of pile in sand, shown in Eq. (5.1)

$$q_b = N_q \sigma_{vo}^{'} \tag{5.1}$$

Where $\sigma_{vo}^{'}$ is the vertical effective stress at the level of the pile tip and N_q is known as the bearing capacity factor, which is a function of the effective friction angle of the sand. Various bearing capacity theories have been proposed for determination of N_q. The influential zone around pile tip is pointed

out by Yang (2006).

The theoretical expression of the bearing capacity factor N_q is correlated with some important factors such as the effective friction angle of sand and its initial confining pressure and relative density by Yang (2008).

In current numerical analysis of pile incorporating constitutive model for sand with crushing, the influence of the relative density is considered in process of parameter determination. The influence of confining pressure and the invariant of effective friction angle of sand is also considered in elasto-plastic constitutive relationship. Basically, the theoretical expression method and numerical method above are the same approach to estimate the pile tip bearing capacity.

5.3 Distribution of the stress and strain around pile tip

Sometimes, the bearing capacity of the pile is not enough to understand soil behavior surrounding pile tip. The distributions and developments of stress and strain quantities around pile tip are significant to achieve such goal. The visualized distributions of stress and strain are beneficial to comprehend soil behavior around pile intuitively. To display the distribution clearly, distributed region is defined not the whole analytical area but only the area in surrounding of the pile tip 216 mm in height and 108 mm in radius corresponding to the model pile loading tests.

Developments of stress and stain quantity variant tendency with surcharge pressure level are discussed from Figure 5.9 to Figure 5.12. In which, each figure is composed of four sub-titles. The mean stress and deviatoric stress are shown in figure (a) and (b). Plastic volumetric and deviatoric strain indicating the crushing and sliding of particles are vividly depicted in figure (c) and (d). It is estimated

that the mean stress *p* is derived to enhance by model pile embedded deeper in the model ground container and larger surcharge pressure. The distributions of the mean stress under three kinds of surcharge pressures are compared among Figure 5.9 (a), Figure 5.10 (a) and Figure 5.11 (a). It clearly shows that high mean stress is concentrated in the soil element beneath pile tip. The distributed areas of the high mean stress *p* and deviatoric stress *q* expand as surcharge pressure increases. The distribution of mean stress becomes wider in radial and downward direction. The value of the mean stress decreases with the larger distance between the position of element and pile tip. The distributed shape seems as ellipses and accords with the analytical results from Dijkstra *et al*. (2011). In the successive figures of Figure 5.9 (b), Figure 5.10 (b) and Figure 5.11 (b), distribution of the deviatoric stress under pile tip also amplifies with surcharge pressure's increasing. High-level deviatoric stress firstly appears at the edge of pile tip and shear band is formed. The area of high-level deviatoric stress becomes wider with surcharge pressure's enhancing. It is concluded that the area surrounding the pile tip is subject to significantly complex compression and shear stress.

The predicted vertical stress of element beneath the model pile tip is approximately 20 MPa which is enough to cause Toyoura sand to be crushed. The predicted stress agrees well with the results of model pile loading test performed by Kuwajima *et al*. (2009).

Plastic deformation can be regarded as the total deformation for sand around pile tip because elastic part is negligible compared with plastic part when the deformation of sand is large enough. Among the comparisons of distributions in Figure 5.9 (c), Figure 5.10 (c) and Figure 5.11 (c), it is predicted that the distributed area of compression is beneath the pile tip. The distributed area of compression forms the wedge. The distributed area and scale of the compression expand with the increasing surcharge pressure and displacement in down direction. The length of the distributed wedge in Figure 5.12 (c) is almost

twice of that in Figure 5.10 (c) in down direction. The volume contraction of soil beneath pile tip is resulted from the particles crushing and arrangement. Lobo-Guerrero *et al*. (2005, 2007) also predicted that particles crushing are mainly concentrated just beneath pile tip by discrete element method.

In addition, the area of the predicted volumetric expansion appears near the pile shaft because the sand particles are highly rotated and sheared. It is observed that the area of distributed expansion slightly contracts with larger surcharge pressure from the Figure 5.9 (c), Figure 5.10 (c) and Figure 5.11 (c). The disappearance of the expansion should be attributed into the crushing and rearrangement of particles. However, the amount of particle crushing cannot be estimated quantitatively. Under the same surcharge pressure, the distributed shape of expansion shows almost no diffidence when the displacement is large among Figure 5.10 (c) and Figure 5.12 (c). It is also found by Dijkstra *et al.* (2006) in the similar numerical analysis. The shape of the volumetric expansion amplifies when the surcharge pressure increases from 200 kPa to 400 kPa due to positive dilatancy under the shear stress. But it shrinks when the surcharge pressure is enhanced to 600 kPa.

All the distributions of the plastic deviatoric strain in figure (d) share the same tendency with these of deviatoric stress. The remarkable band indicating high-level shear stress is also formed. The dilatancy behavior of soil around model pile is reasonably predicted and clarified.

The change of the distribution tendency with the displacement of model pile is discussed in Figure 5.10 and Figure 5.12. In Figure 5.10, the displacement ratio is set as S/D= 0.5. While it is equal to 1.0 in Figure 5.12, the distributions of the mean and deviatoric stresses together with volumetric and deviatoric strain expand with larger displacement. The characteristics of the distribution figures are almost the same.

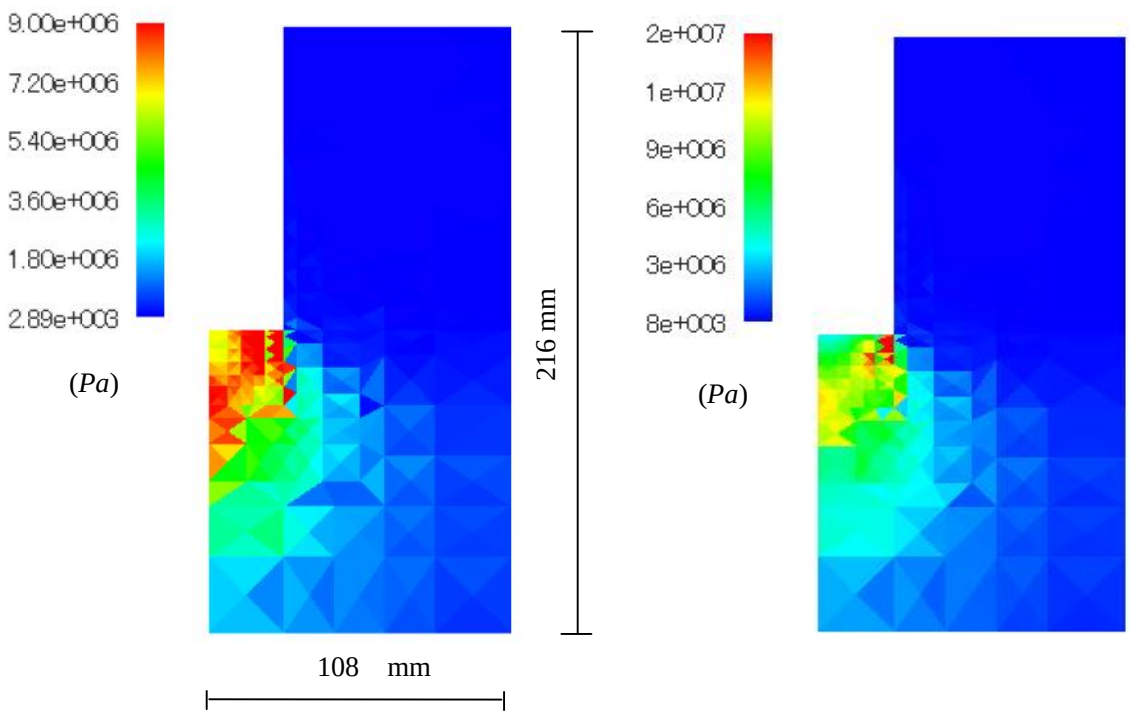

(a) Mean stress p

(b) Deviatoric stress q

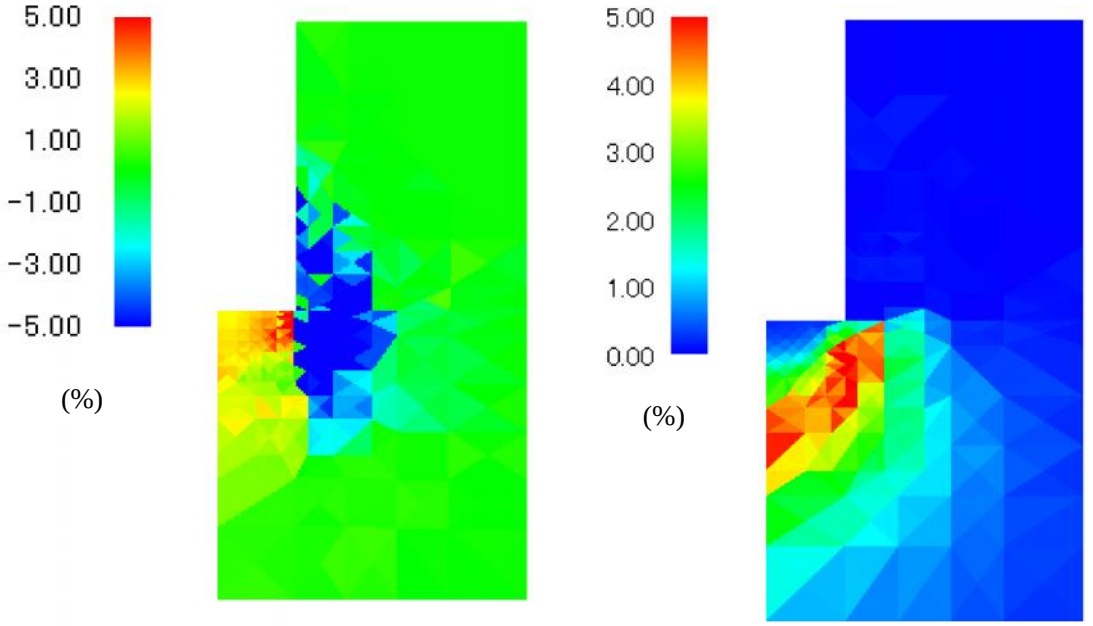

(c) Plastic volumetric strain ε_v^p

(d) Plastic deviatoric strain ε_d^p

Figure 5.9 Distributions of stress and strain around pile tip with 30 mm diameter (Surcharge pressure =200 kPa, S/D= 0.5)

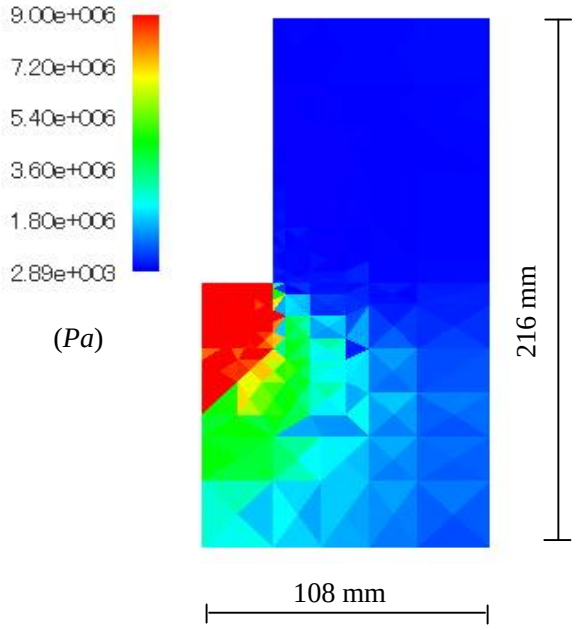

(a) Mean stress p

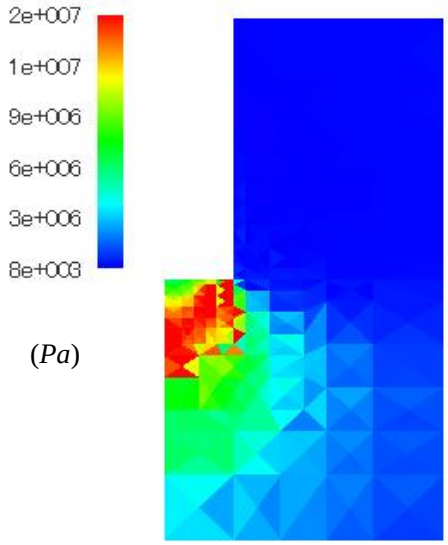

(b) Deviatoric stress q

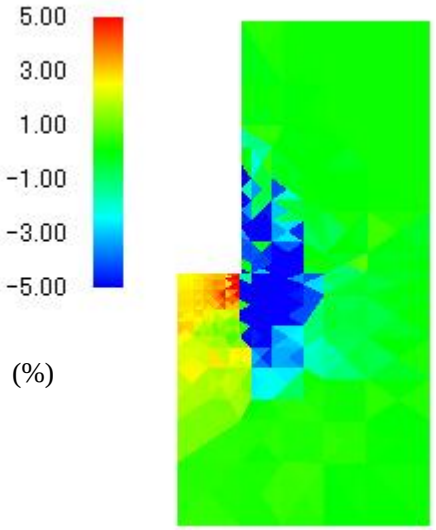

(c) Plastic volumetric strain $\pounds_v^p$

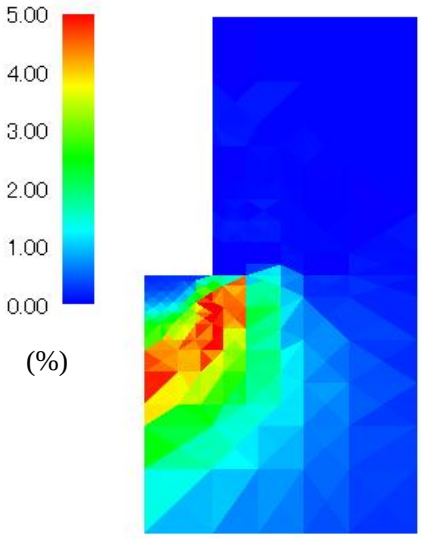

(d) Plastic deviatoric strain $\pounds_d^p$

Figure 5.10 Distributions of stress and strain around pile tip with 30 mm diameter (Surcharge pressure =400 kPa, S/D= 0.5)

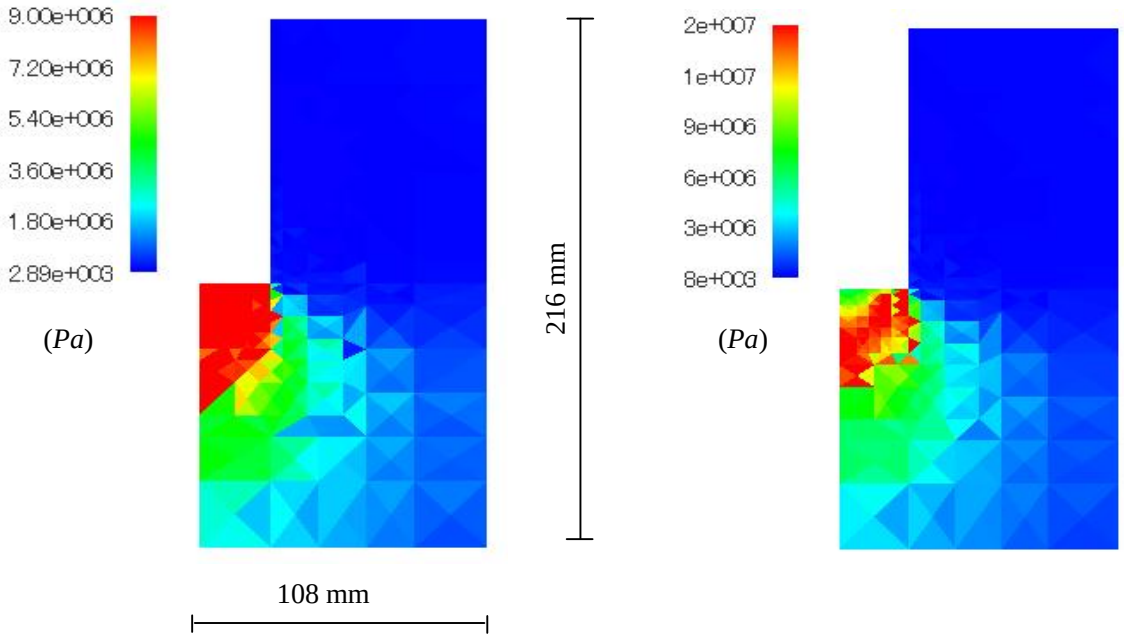

(a) Mean stress p (b) Deviatoric stress q

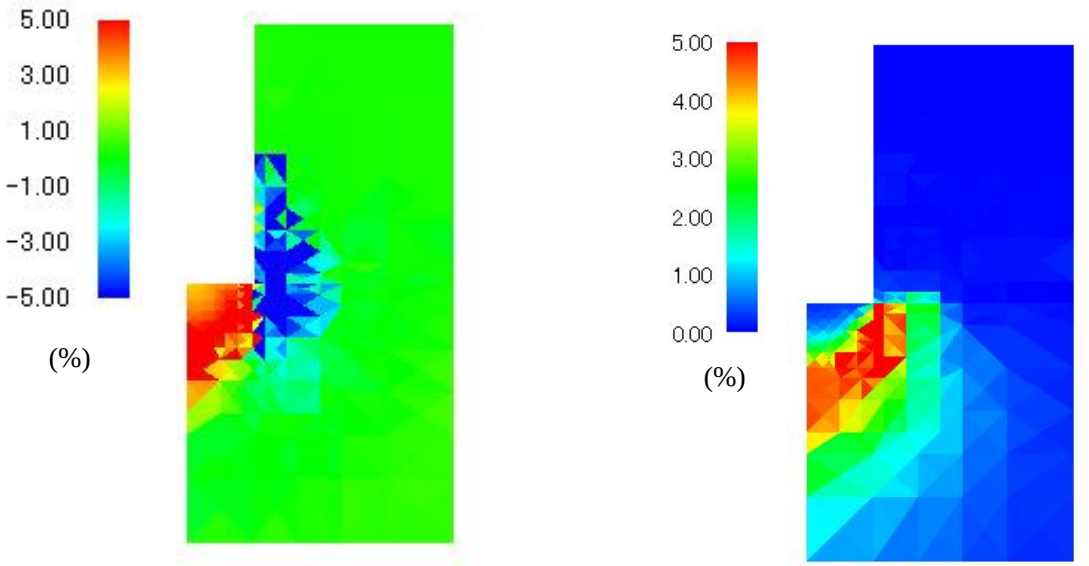

(c) Plastic volumetric strain ε_v^p (d) Plastic deviatoric strain ε_d^p

Figure 5.11 Distributions of stress and strain around pile tip with 30 mm diameter (Surcharge pressure=600 kPa, S/D= 0.5)

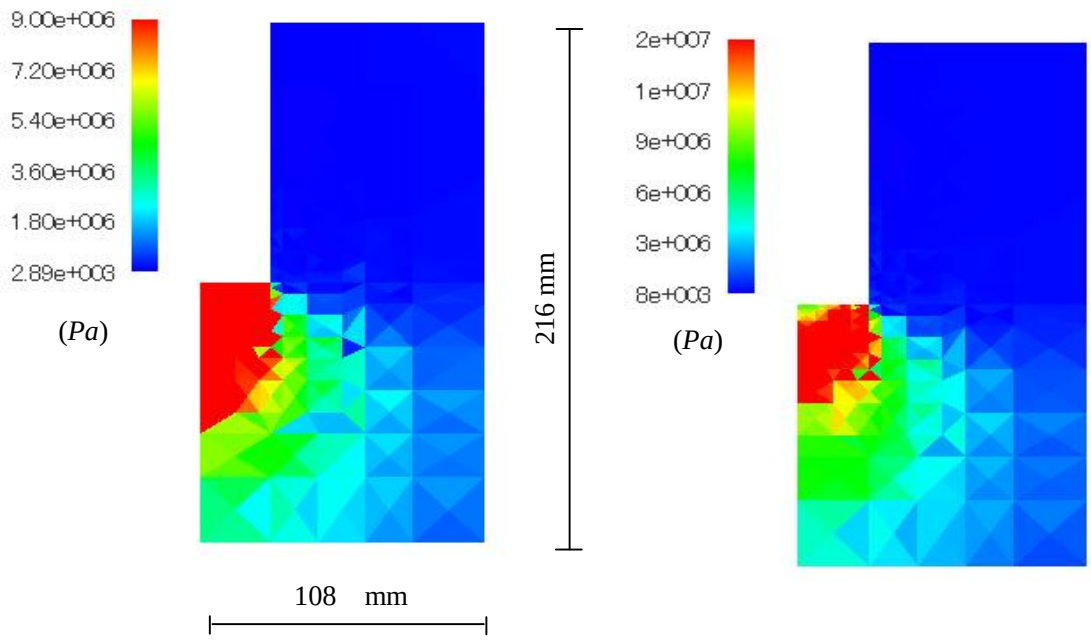

(a) Mean stress p (b) Deviatoric stress q

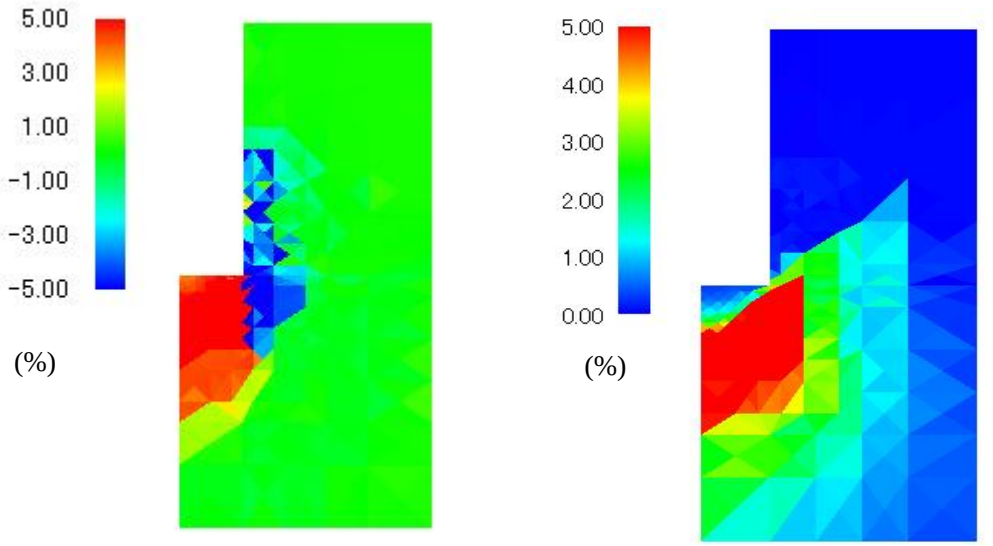

(c) Plastic volumetric strain ε_v^p (d) Plastic deviatoric strain ε_d^p

Figure 5.12 Distributions of stress and strain around pile tip with 30 mm diameter (Surcharge pressure=400 kPa, S/D= 1.0)

5.4 The comparison of predicted results from small and large deformation theory

5.4.1 Predicted values from small deformation theory and large deformation theory

The deformation of soil under complex stresses in the soil surrounding the pile tip exhibits typical large deformation behavior. Therefore, finite element analysis using large deformation theory is an effective approach to tackle the driving and penetrating pile process. To overcome the deficiency in numerical analysis from small deformation theory, the mixed incremental method for UL method and joint element are employed explained in chapter 4 to solve the large deformation behavior. The procedure of the numerical analysis is the same that used in small deformation theory.

The predicted relationships between the normalized bearing stress and normalized displacement from the small and large deformation theory are compared with experimental results under three kinds of surcharge pressure. The broken curves represent the experimental results, and the solid curves express the predicted values. Although both the predicted values from small and large deformation theory overestimates the experimental results. It is noticed that the predicted precision from large deformation theory is more close to actual solution results with increasing the pile penetration depth in Figure 5.13 and Figure 5.14. The predicted result from large deformation theory improves almost 5 percent predicted accuracy than the results from small deformation theory when the surcharge pressure is 200 kPa in Figure 5.13. The predicted result from large deformation theory agrees quite well when the surcharge pressure is 600 kPa in Figure 5.14. The predicted accuracy could be improved by applying the large deformation theory and joint element into finite element analysis. More actual behavior of soil around soil tip can be estimated.

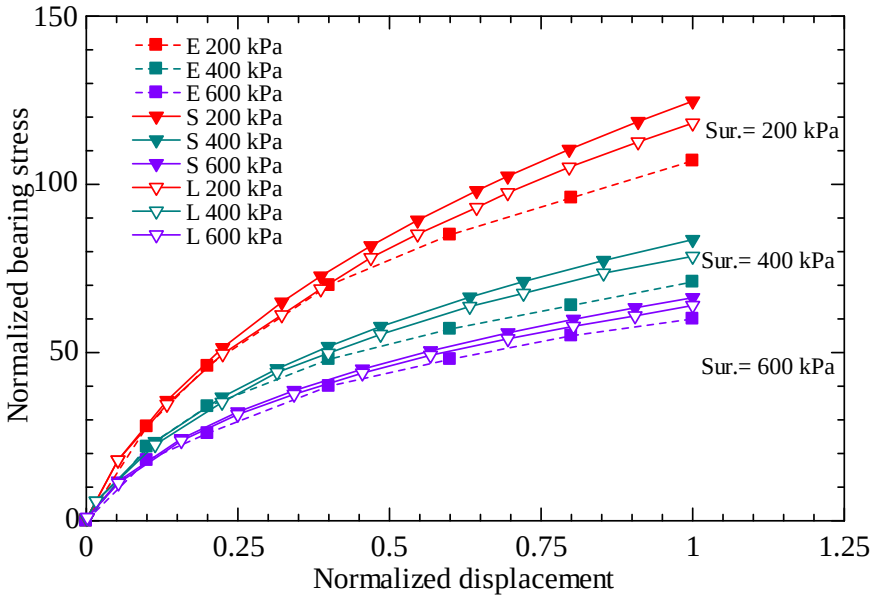

Figure 5. 13 Comparison of predicted (large and small strain) and measured normalized bearing stress displacement curves for model pile with diameter 30 mm

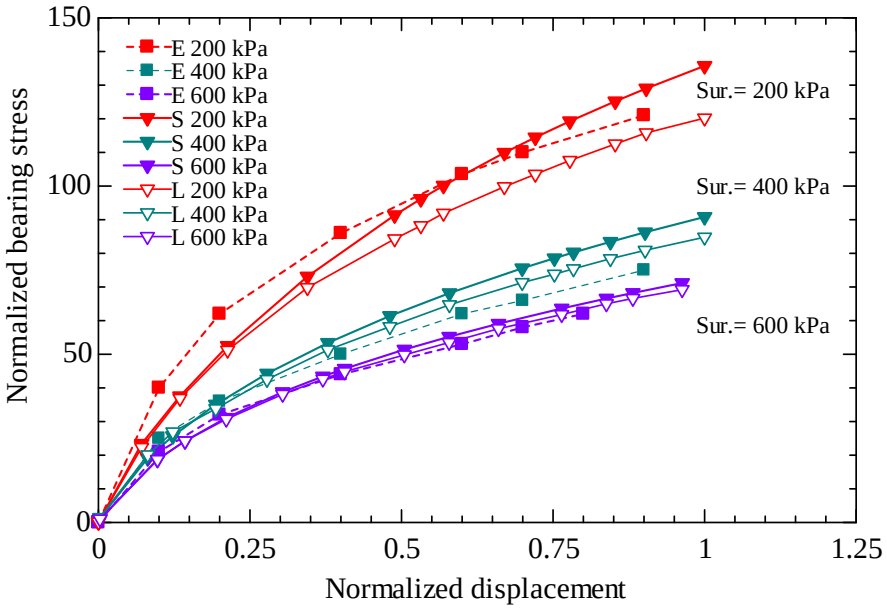

Figure 5. 14 Comparison of predicted (large and small strain) and measured normalized bearing stress displacement curves for model pile with diameter 54 mm

5.4.2 Deformation of meshing elements around pile tip

To intuitively understand the soil deformation behavior around the pile tip, only partial meshing

surrounding the pile tip is shown in detail. The figures of deformed mesh for model pile with diameter 30 mm are represented at penetration depth as 0 mm, 15 mm and 30 mm. The displayed region of meshing is 120 mm in radius (four times the pile half-diameter) and 120 mm in height. The deformed elements after loading help to demonstrate the soil behavior and movement. The diameter of model pile is 30 mm.

The initial stage meshing is shown in Figure 5.15 (a). The medium stage meshing is shown in Figure 5.15 (b), and its displacement is equal to half of the diameter of pile. The final stage meshing is depicted in Figure 5.15 (c). According to Figures 5.15 (b) and (c), the area beneath the pile tip element is significantly deformed and compressed. The elements located near the pile shaft are severely distorted and sheared. The irregular deformations worsen the results of the prediction. Overall, the deformed elements display spherical or elliptic shapes in Figure 5.15 (c). However, the element distortion failure noted by previous researchers is not found.

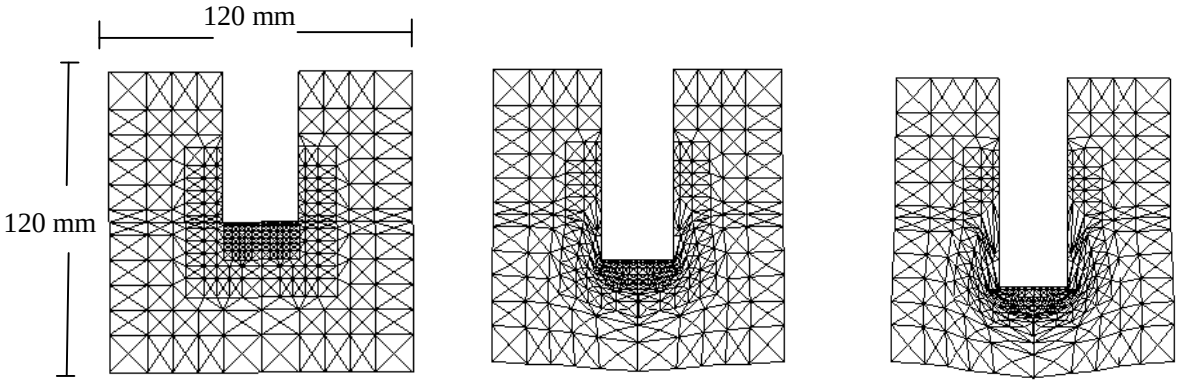

(a) Displacement 0 mm (b) Displacement 15 mm (c) Displacement 30 mm

Figure 5.15 Initial and deformed elements (120 mm in width, 120 mm in height in case of large deformation)

5.5 Summary

The numerical analysis of model pile loading in sand under three levels of surcharge pressures is presented in this chapter. The analytical program is implemented by displacement–controlled method for more precisely predicted results.

To investigate the bearing mechanism of pile, the pile loading test with two kinds of diameter were performed. The model pile with diameter 30 mm and 54 mm are employed in the test. The confining effect on the bearing capacity of pile is discussed with the different diameter ratio of the model ground and pile under the same loading condition. The predicted results show that the bearing stress is less affected by the confining pressure when the diameter ratio is larger than 20. When diameter ratio is less than 10, the confined effect is serious and calculation is incredible.

The predicted relationship between the normalized bearing stress and displacement are compared with experimental measurements, showing good agreement. Once the confining stress increases, the normalized bearing stress decreases on the contrary. The deceasing tendency of the normalized bearing stress is related to the particle crushing.

The developments of the stress and strain around pile tip under different surcharge pressures and penetrating depths are also depicted. The high compressive and sheared region can clarified based on the above analysis. Some conclusions about the distributions can be summarized as follows. The distribution of the stress value expands with larger surcharge stress and displacement. The distributed shape of the mean stress is ellipse and becomes wider with larger surcharge pressure and displacement. The distributed shape of the high-level deviatoric stress appears firstly near the edge of pile tip and forms the shear band. The volumetric contraction (negative dilatancy) is beneath the pile tip. The area of

the predicted compression forms wedge and expands with larger surcharge pressure and displacement in down direction. The area of the predicted volumetric expansion (positive dilitancy) appears near the pile shaft because the sand particles are highly rotated and sheared. With increasing the surcharge pressure, the volumetric expansion slightly compacts because of the crushing and rearrangement of particles. The dilatancy change around pile tip can be reasonably described.

It is concluded that the crushing model integrating into the finite element method is an effective method to estimate the bearing capacity of pile.

Reference

Dijkstra, J., Broere, W. and Van, A.F. (2006). “Numerical investigation into stress andstrain development around a displacement pile in sand”. Proceedings of the Sixth European Conference on Numerical Methods in Geotechnical Engineering, 595-600.

Dijkstra, J.,Broere, W. and Heeres,O.M. (2011). “Numerical simulation of pile intallation”, Computers and Geotechnics., 38(5),612-622.

Kuwajima, K., Hyodo, M. and Hyde, A.F.L. (2009). “Pile bearing capacity factors and soil crushability”, Journal of Geotechnical and Geoenvironmental Engineering, 135(7), 901-913

Li, W. and Yamamoto, H. (2005). “Numerical analysis on soil behavior around pile-tip under vertical load”, Journal of Structural Engineering, 51(B), 147-157. (In Japanese)

Lobo-Guerrero, S. and Vallejo, L.E. (2005). “DEM analysis of crushing around driven piles in granular materials”, Geotechnique, 55(8), 617-623.

Lobo-Guerrero, S. and Vallejo, L.E. (2007). “Influence of pile shape and pile interaction on the crushable behavior of granular materials around driven piles: DEM analyses”, Granular Matter, 9(3–4), 241–250.

Sun, D. A., Huang, W. X., Sheng, D.C. and Yamamoto, H. (2007). “An elastoplastic model for granular materials exhibiting particle crushing”. Key Engineering Materials, 41, 1273-1278.

Wu, Y. and Yamamoto, H. (2011a). “Confined Effects for Vertical Bearing Capacity of Pile in Sand”, Japan geotechnical society 46th national conference, 602-603.

Wu, Y. and Yamamoto, H. (2011b): Confined and surcharge stress level effects on bearing capacity of pile in sandy soil, Proceeding JSCE 13th International Summer Symposium, Kyoto, 203-206.

Yamamoto, H., Li, W., Tominaga, K. and Ogura, H. (2003). “Experimental study on effects of overburdening pressures and end shapes for point bearing capacities of pile”, Journal of Structural Engineering, 49(B), 157-162. (In Japanese)

Yang, J. (2006) “Influence Zone for End Bearing of pPiles in Sand”, Journal of Geotechnical and Geoenvironmental Engineering, 132(9), 1229-1237.

Yang, J., and Mu, F. (2008) “Use of State-Dependent Strength in Estimating End Bearing Capacity of Piles in Sand”, Journal of Geotechnical and Geoenvironmental Engineering, 134(7), 1010-1014.

CHAPTER 6

EFFECT OF PILE TIP SHAPE ON THE SOIL BEHAVIOR AROUND PILE TIP

Underreamed (enlarged-base) piles are commonly employed in engineering practice. The pile tip is often made into different shapes. Underreamed piles are usually used to increase the size of the pile base diameters and hence provide greater bearing capacity at a more economical cost than a straight-shaft pile. The model pile loading test is presented in Chapter 5. The model pile adopts the straight pile and the enlarged-base pile in the test. The diameter of straight model pile is 30 mm and 54 mm. The numerical analysis of straight pile is implemented and explained in previous chapter.

There exists very limited research on the effect of pile tip shape on the behavior of the surrounding soil. Lobo-Guerrero and Vallejo (2007) remarked that pile tip shape has a significant impact on pile penetration and particle crushing. Herein, the emphasis is focused on the effect of the pile tip shape on the bearing mechanism of the pile and the mechanical behavior of the sand around the pile. A finite element analysis combined with a mixed incremental method for the updated Lagrangian method is presented using a small strain integration formulation to solve the large deformation problem. Constitutive model for sand with particle crushing and joint elements are used to represent the behavior of sand around the pile and the interactive surface between the sand and the pile.

The underreamed piles include flat base piles and the pencil-shaped base piles, as shown in Figure 6.1. The diameter of pile shaft is 30 mm. The base-enlarged part, with a diameter 54 mm, is made of mortar. The convergent angle ~ , which is between the axial line and the line of the pile base, is used to describe the shape of the pile base. The model piles were tested at convergent angles ~ of 30, 60 and 90 degrees.

The model piles with different pile base shapes are jacked into a ground tank container filled with

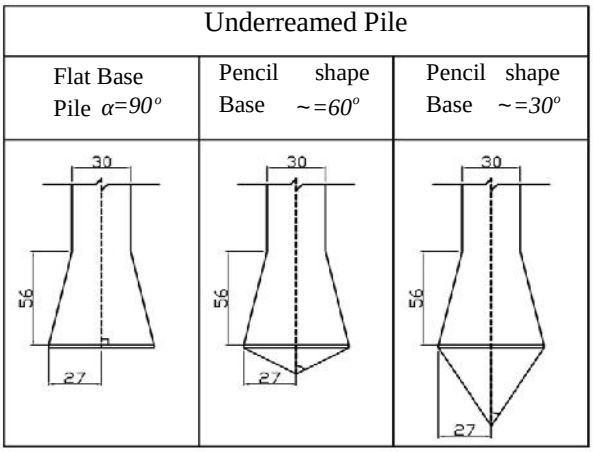

Figure 6.1 Different types of pile tip

Toyoura sand to demonstrate the effects of pile base shape and surcharge pressure level on the bearing capacity and to investigate the movement of sand particles around the pile tip area.

The behavior of the sand ground is represented by the constitutive model considering particle crushing. The joint element is applied to simulate the interface behavior during the pile loading process. The joint elements are placed on the pile shaft and the pile tip. For calculation simplicity, the meshing was finished using three nodal triangular elements. The total numbers of triangular elements, joint elements and nodes for different piles are shown in Table 6.1.

Table 6.1 Total number of meshing elements for underreamed piles

	Flat Base	Pencil-shape	Pencil-shaped Base Pile
Convergent angle	90	60	30
Triangular element number	822	779	747
Joint element number	18	24	26
Node number	450	428	412

The numerical calculations are conducted using the displacement-controlled method. The displacement control points are at the bottom of the pile tip and all control points descend simultaneously. The displacement is added by equivalent increments. The final displacement is equal to the shaft diameter of the pile in each calculation step. The influence of the pile installation on the bearing capacity is neglected because the model pile is installed before the model ground is created.

The boundary-constrained condition for the model ground is set to correspond to the model pile loading test setup. The basic physical features of Toyoura sand in the triaxial compression test and the ground material in the model pile loading tests are the same in Chapter 6.

The predicted relationship between the normalized displacement and bearing stress is compared with the test results, showing good agreement. The effect of pile tip shape on the bearing capacity of pile is also discussed. The displacement vectors of soil around pile with different shapes are displayed. The stress and strain contours of soil around pile with different pile tip shapes are presented and visualized. Furthermore, the mechanical behavior of soil element in different depths beneath the pile tip is compared. The numerical results clearly indicate that the soil beneath the pile tip at different depths displays various volumetric changes and confirms the necessity of the constitutive model for sand with particle crushing.

6.1 Relationship between the normalized bearing capacity and displacement

6.1.1 Normalized bearing stress and normalized displacement

In this study, the normalized bearing stress is defined as the ratio of the current bearing stress at the

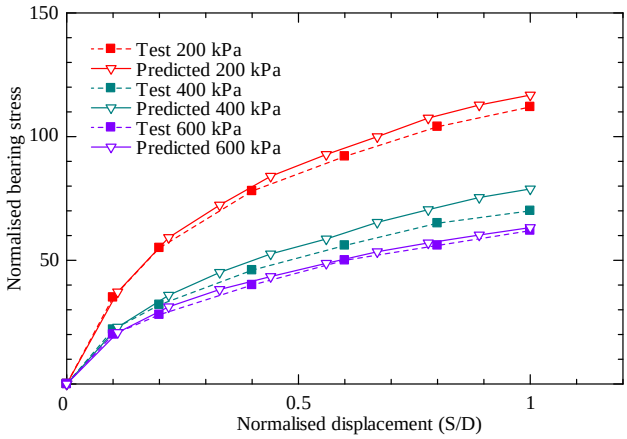

Figure 6.2 The relationship between normalized bearing stress and normalized displacement (~=90^o)

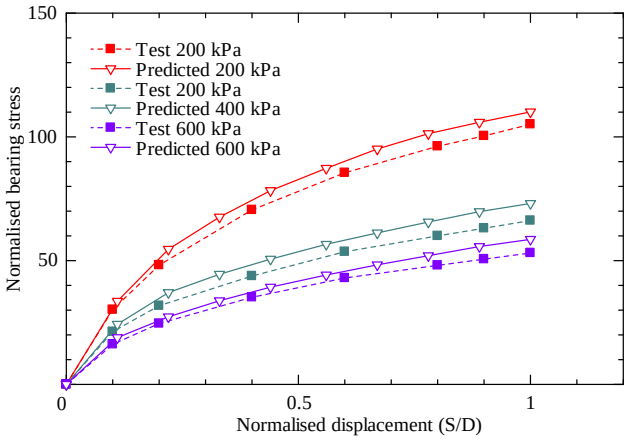

Figure 6.3 The relationship between normalized bearing stress and normalized displacement (~=60^o)

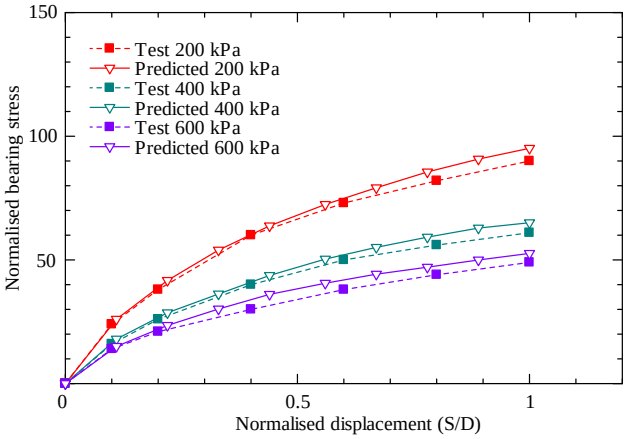

Figure 6.4 The relationship between normalized bearing stress and normalized displacement (~=30^o)

pile tip to the surcharge pressure. The normalized displacement is often used in analyses, as defined by the ratio of the current displacement (S) to the pile shaft diameter (D). In the numerical simulation, the pile is pushed into the sandy soil by the prescribed displacements. The vertical reaction forces are summed to the pile tip. Predicted values by numerical analysis of underreamed piles with flat bases and pencil-shaped bases are compared with experimental results in Figure 6.2, Figure 6.3 and Figure 6.4. The broken lines show the experimental results, while the solid lines show the predicted values. The convergent angles of the pencil-shaped piles are 60 and 30 degrees.

The predicted values agree well with the experimental results during the entire loading process for each surcharge pressure. The accuracy of the predicted value is especially good when the displacement is small. All the predicted values slightly overestimate the actual test results, as shown in Figures 6.2, 6.3 and 6.4. The predicted discrepancy is less affected by pile shape. The maximum discrepancy between predicted and measured results occurs when the surcharge pressure is 400 kPa. Li and Yamamoto (2005) also predicted the same relationship using small deformation analysis and the modified Cam Clay model revised using the SMP criterion. The predicted result only agreed with test results when the normalized displacement was smaller than 0.5. The accuracy of the prediction is improved by incorporating the large deformation analysis and mechanical characteristics of the joint element and by using the constitutive model for sand with particle crushing.

The bearing stress of the pile with the enlarged base has been increased during the test. However, the rate of increase of the bearing stress depends on the shape of the enlarged base. The numerical results show that the bearing stress of the underreamed pile decreases as the convergent angle deceases. The normalized bearing stress of the pencil-shaped base pile with a 30-degree convergent angle loses approximately twenty percent at the final state (S/D= 1.0). The confining stress on the soil particles in

the area around the pile tip decreases as the convergent angle decreases. Although the surcharge pressure acting on the top surface of the model ground increases, the normalized bearing stress decreases, contrary to the expected trend. This decreasing in the normalized bearing stress is related to the particle crushing. It can be explained by the high number of sand particles that are crushed under the high surcharge pressure.

6.1.2 Effect of pile tip shape on the normalized bearing capacity of pile

The influence of pile tip shape on bearing capacity of model pile is studied by comparing the bearing capacity of the underreamed pile to that of the straight pile. Here, bearing capacity of straight pile with diameter 54 mm is assumed to be the reference standard pile bearing capacity $q_{(\Phi 54).}$ Bearing capacity of other underreamed piles are compared to the reference pile of model pile's bearing capacity with normalized bearing capacity $q_{(\Phi 54)}$. From the specific ratio variation of the model with normalized displacement ratio, the influence of pile tip shape is understandable. Three figures show the relationship between bearing capacity ratio $q/q_{(\Phi 54)}$ and the displacement ratio S/D of pile with convergent angle 90^o and 30^o. In each figure, analytical curves of two underreamed model pile under different surcharge pressures are shown in Figures 6.5 (a), (b) and (c). In each figure, the vertical axis means the ratio of bearing capacity by the reference standard pile bearing capacity $q_{(\Phi 54)}$, and the horizontal axis means the pile displacement ratio (S/D). The broken curves mean the test results, and the solid curves express the prediction values. Prediction values are agreeable with the test results; however, prediction values slightly underestimate the actual results. All curves decrease with displacement ratio enhancing and prediction curves reasonably show such tendency.

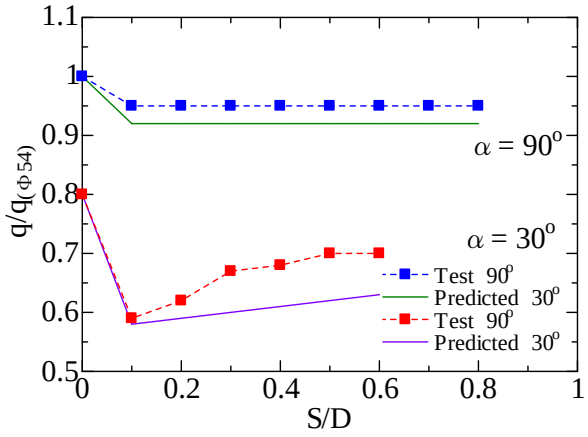

(a) When surcharge pressure is 200 kPa

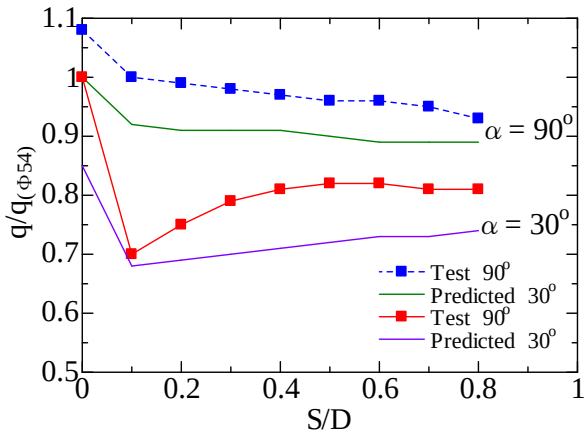

(b) When surcharge pressure is 400 kPa

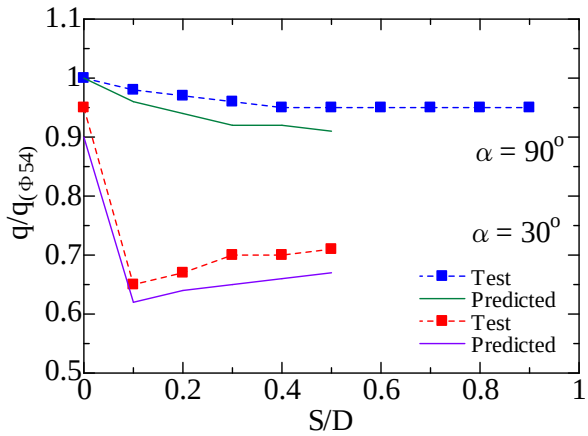

(c) When surcharge pressure is 600 kPa

Figure 6.5 Relationships between bearing capacity ratio $q/q_{(\Phi 54)}$ and settlement to pile end diameter ratio S/D of pile with convergent angle 90° and 30°

Curves of underreamed model pile with convergent angle with 90^o decrease and reach to a steady ratio value. Besides, curves of underreamed model with convergent angle with 30^o go down firstly until displacement ratio is around 0.1, then increase slightly and gradually to the steady ratio value. The ratio of bearing capacity are less than unit, it shows that bearing capacity reduces in various degree.

Bearing capacity reduction of model pile are obviously observed and can be explained that the soil in surrounding of underreamed pile is less confined compared to that of straight pile. The soil around underreamed pile can move and rotate easily in all direction. Therefore, the bearing capacity of underreamed model pile will descend to some extent. Pile bearing capacity will decrease when the convergent angle become much sharper.

6.2 Distribution of displacement vector

6.2.1 Displacement vector

The distributions of soil element displacement vector for straight pile and undereamed piles with different convergent angles are shown in Figure 6.6. The penetration of the model pile is equal to the diameter of pile shaft under the same surcharge pressure. Figure 6.6 (a) shows the distribution of displacement vector of straight, while those of underreamed pile with convergent angle 90, 60 and 30 degree are displayed in Figures 6.6 (b), (c) and (d) respectively.

The distributions of displacement will help us to understand the soil deformation behavior visually.

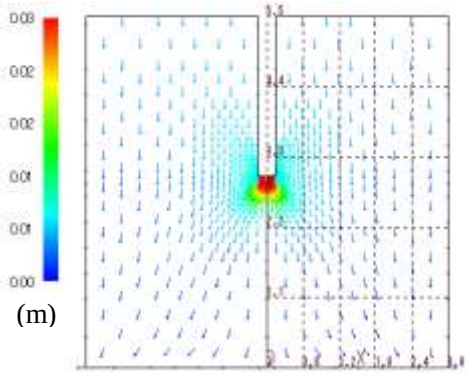

(a) Straight pile diam=30 mm

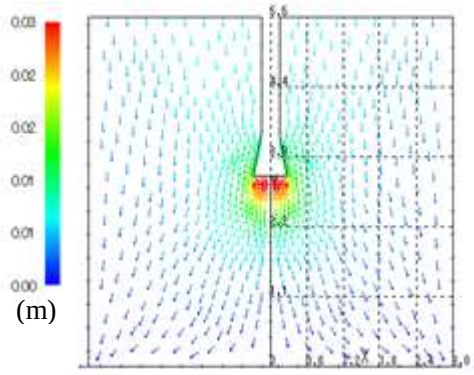

(b) Underreamed pile with convergent angle 90 ^{o}

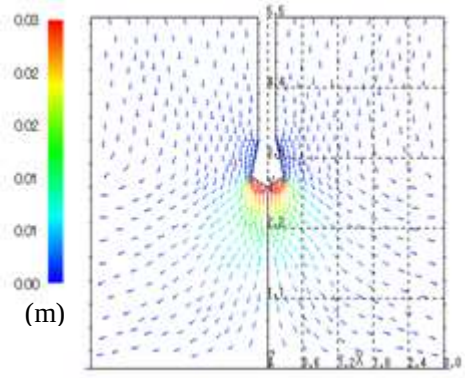

(c) Underreamed pile with convergent angle 60 ^{o}

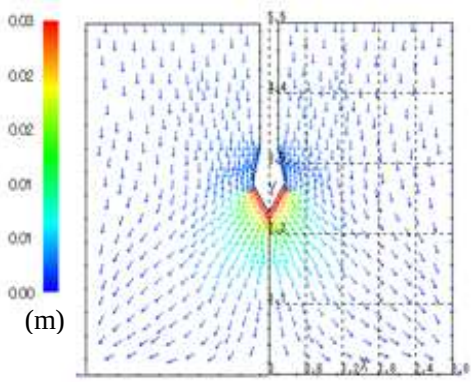

(d) Underreamed pile with convergent angle 30 ^{o}

Figure 6.6 The distribution of displacement vector of three types of model pile
(S/D= 1.0, Surcharge pressure = 200 kPa)

The predicted results shows that the displacement vector distribution range (no-zero displacement) of underreamed piles in Figure 6.6 (c) and (d) is large than that of pile with flat base in Figure 6.6 (a) and (b). The distributed range of the highest value displacement vector (red color) of underreamed pile is small that those of the pile with flat base. The distribution pattern around pile tip shows oval-shapes. In the compressive region beneath pile tip, it is observed that the angle between the displacement vector to the vertical axial become large with convergent angle decreasing.

6.2.2 Distribution of the displacement contour with different depths

To investigate the soil behavior around pile with different penetration, displacement contours of pile is represented. Figures 6.7, 6.8 and 6.9 show the distributions of displacement contours when the normalized displacement is 1.0, 1.5 and 2.0. In each figure, (a) shows the distribution of displacement vector of straight, while those of underreamed pile with convergent angle 90, 60 and 30 degree are displayed in figures (b), (c) and (d) respectively. The surcharge pressure is set as 200 kPa. Among the three figures, it is observed that the high-value distributed area of displacement contous for the underreamed pile is wider and extensive than that of the straight pile. Moreover, the shape of the distributed area in sourrounding of pile tip is ellipsoid. It is also displayed that the distributed area of

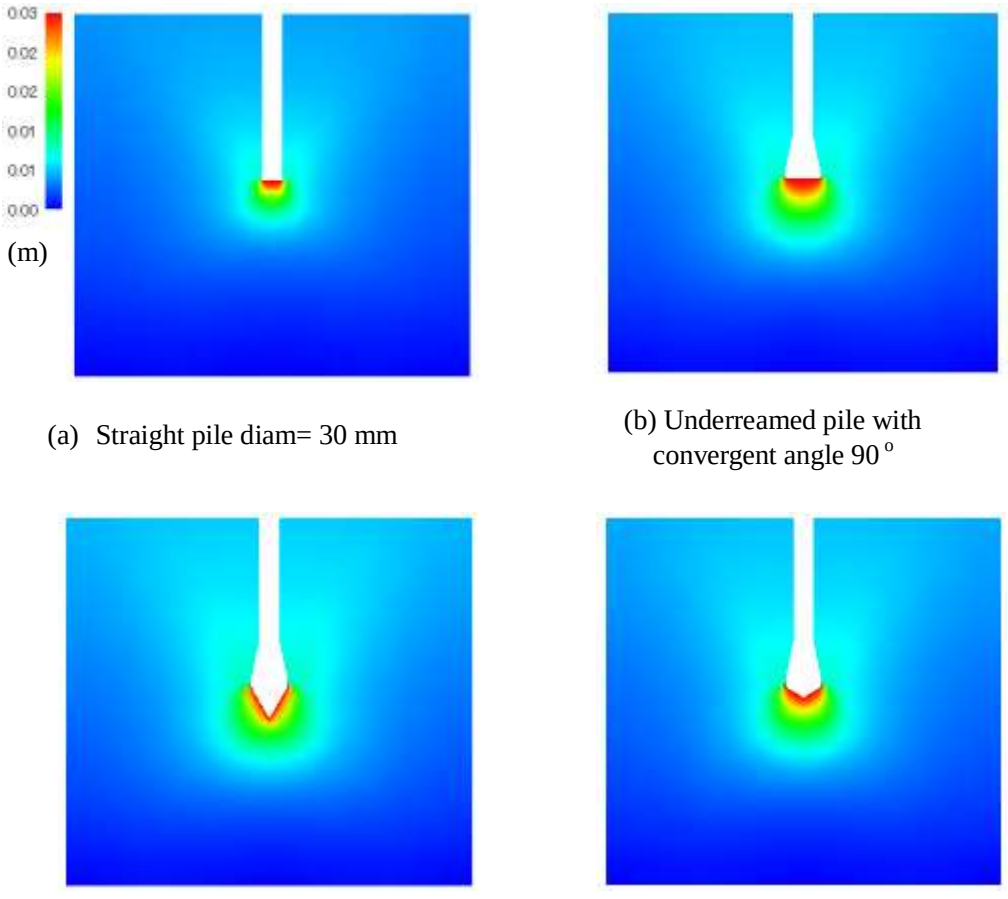

(a) Straight pile diam= 30 mm

(b) Underreamed pile with convergent angle 90 ^{o}

(c) Underreamed pile with convergent angle 60 ^{o}

(d) Underreamed pile with convergent angle 30 ^{o}

Figure 6.7 The distribution of displacement contour when S/D= 1.0

displcament contour extend in both axial-down and radial direction. The distributed range of the dispalacement contour close to the pile shaft become obvious with the normarlized displacement value increseing. From comparation of figure (b), (c) and (d), the distributed area of maximum displacment contracts as convergent angle gets shaper. From comparation among the Figures 6.7, 6.8 and 6.9, the distribution of displacement contours near to the pile shaft becomes obvious. It is observed that distributed range of displacement contour in vertical-down is not affected by the penetration of pile. However, the distributed range expands in radial direction with larger penetration. These three group of figures benefit us to apprehend the soil deformation around pile with different penetrations.

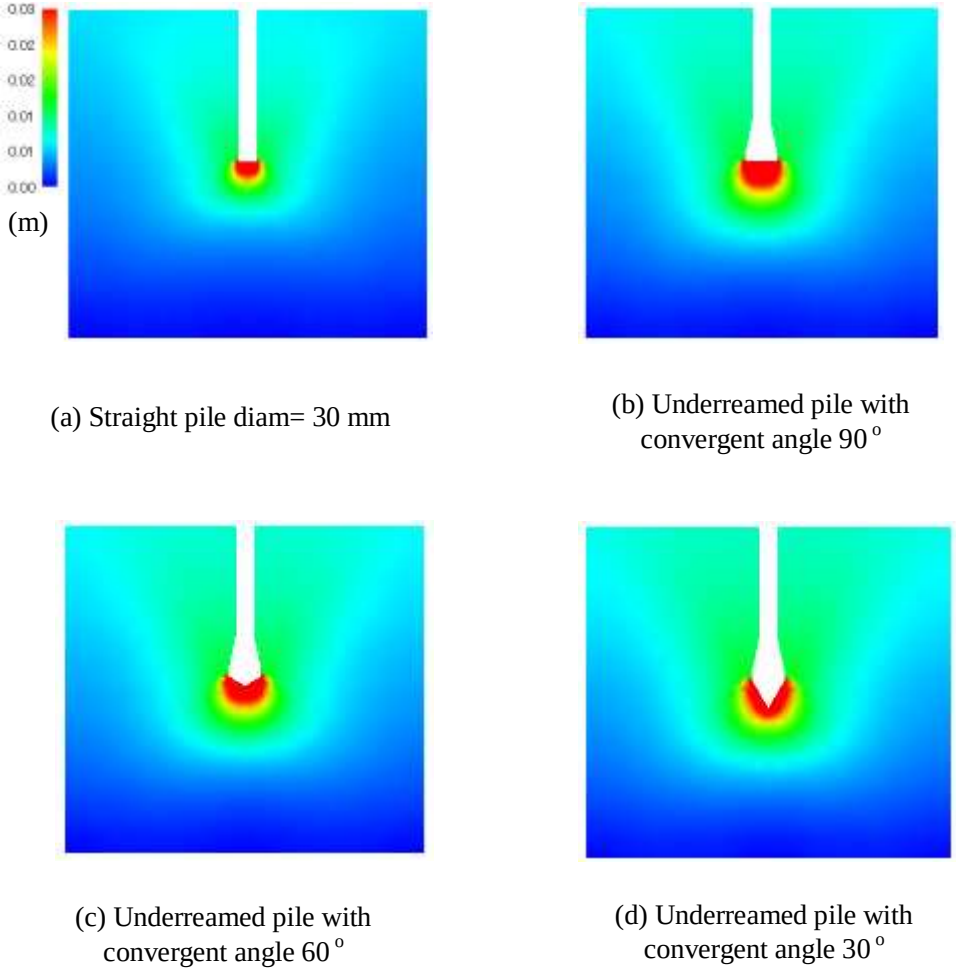

(a) Straight pile diam= 30 mm

(b) Underreamed pile with convergent angle 90 ^{o}

(c) Underreamed pile with convergent angle 60 ^{o}

(d) Underreamed pile with convergent angle 30 ^{o}

Figure 6.8 The distribution of displacement contour when S/D= 1.5

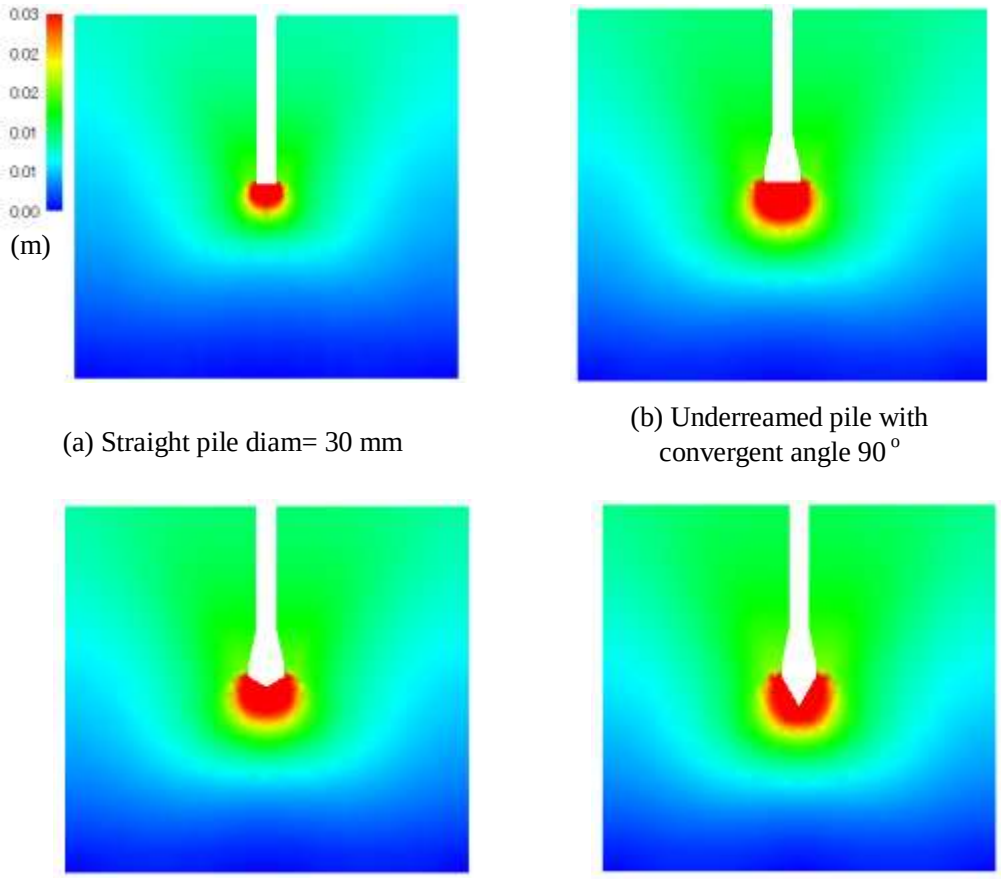

(a) Straight pile diam= 30 mm

(b) Underreamed pile with convergent angle 90 ^{o}

(c) Underreamed pile with convergent angle 60 ^{o}

(d) Underreamed pile with convergent angle 30 ^{o}

Figure 6.9 The distribution of displacement contour when S/D= 2.0

6.3 Distribution of the stress and strain contours

The visualization of the stress and strain contours helps in understanding the soil behavior when pile is jacked into sandy soil. Dijkstra et al. (2009) also implemented the axisymmetric analysis of pile installation in both loose and dense sand layers. The distribution of radial stress, vertical stress and circumferential stress contours in the sand around the underreamed pile are shown in Figures 6.10, 6.11 and 6.12, respectively. The distribution of radial strain, vertical strain and circumferential strain

contours of sand around the underreamed pile are shown in Figures 6.14, 6.15 and 6.16, respectively. In this study, (a), (b) and (c) in each figure represent the distribution of stress or strain contours of pile with convergent angles of 90, 60 and 30 degrees. The stress and strain contours are shown for the pile penetrating at different depths for the same surcharge pressure level. The normalized displacement reaches 0.5 and 1.0 in (c) and (d) in each case. The initial surcharge pressure, 200 kPa, is given to all the elements of the model ground in the vertical direction. The lateral coefficient of earth pressure is set as 0.5. The compressive direction is taken as the positive in all the stress and strain contours.

The maximum radial stress first occurs at the corner of the pile base in Figure 6.10 (a). The pile base

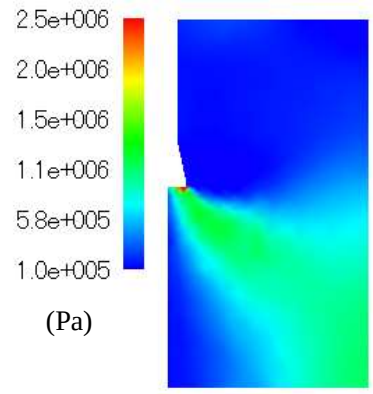

(a) S/D= 1.0, $\alpha=90^o$

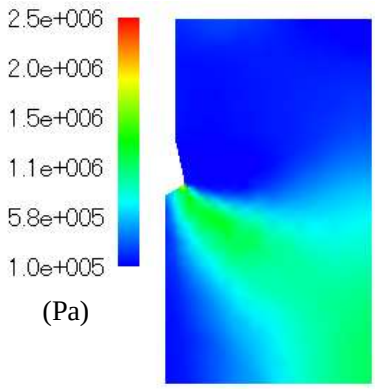

(b) S/D= 1.0, $\alpha=60^o$

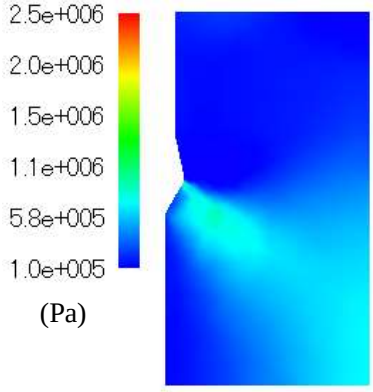

(c) S/D= 0.5, $\alpha=30^o$

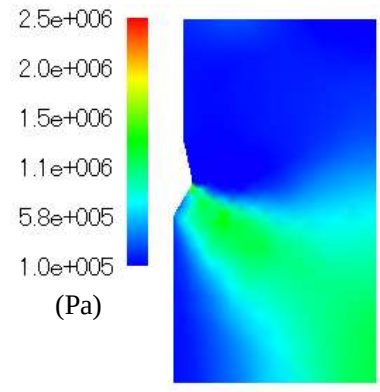

(d) S/D= 1.0, $\alpha=30^o$

Figure 6.10 The radial stress contours (Surcharge pressure 200 kPa)

was made of mortar, and crack failure was observed on the surface of the flat base of the pile in Figure 6.13 (a) when the tests were completed. Once crack failure occurs in the pile base, the bearing capacity of the pile decreases. The results in Figure 6.10 (a) and Figure 6.10 (d) show that the radial stress around the pile with the pencil-shaped base is smaller than that of the pile with the flat base. The underreamed pile with the pencil-shaped base is capable of preventing crack failure, as shown in Figure 6.13 (b). The crack failure in this case is explained as the result of significant radial stress acting on the pile base when the pile base shape is flat.

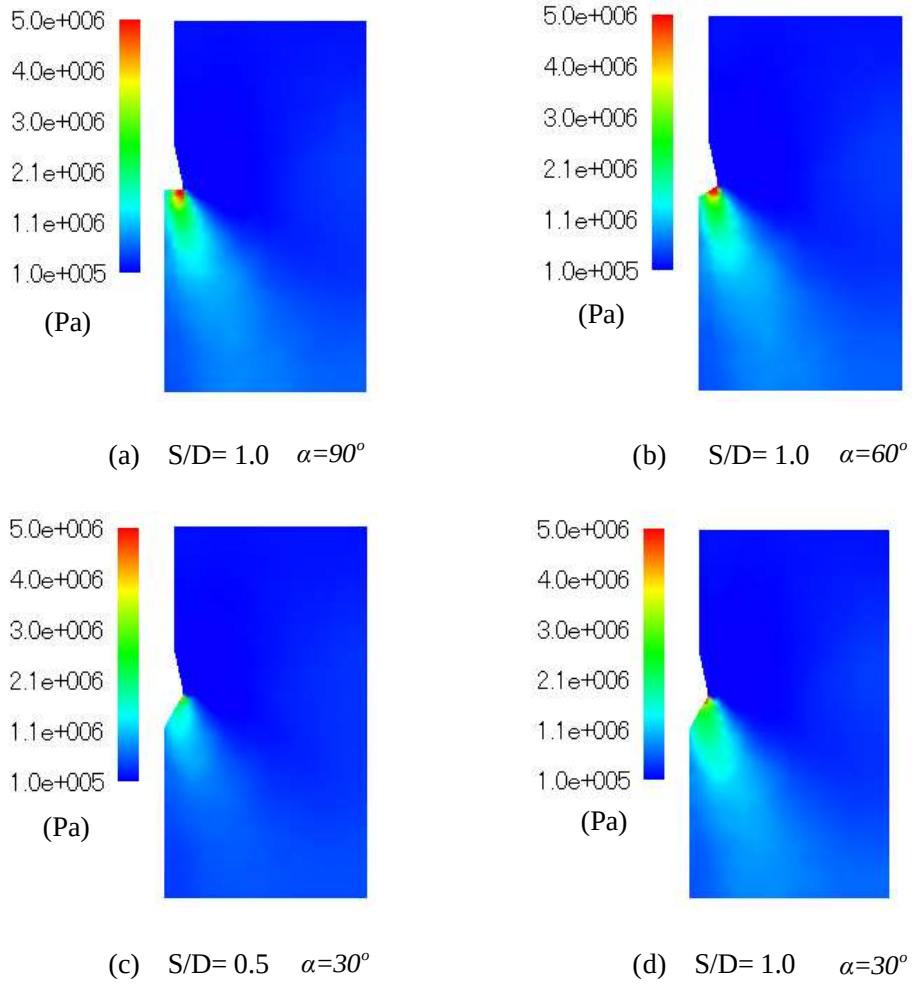

(a) S/D= 1.0 $\alpha=90^o$ (b) S/D= 1.0 $\alpha=60^o$

(c) S/D= 0.5 $\alpha=30^o$ (d) S/D= 1.0 $\alpha=30^o$

Figure 6. 11 The vertical stress contours (Surcharge pressure 200 kPa)

The distribution of the vertical stress contours is displayed in Figure 6.11. The distributed area of high-value vertical stress is approximately three diameter lengths in the vertical down direction and three diameter lengths in the radial direction. The high-value vertical stress concentrates in the corner just beneath the pile base in Figure 6.11 (a) and Figure 6.11 (b). The distributed shape of vertical stress contour expands as the pile penetrates deeper in the sand, as observed by comparing Figure 6.11 (c) with Figure 6.11 (d). The range of the high-value vertical stress decreases markedly as the convergent angle decreases, as shown in Figure 6.11 (d).

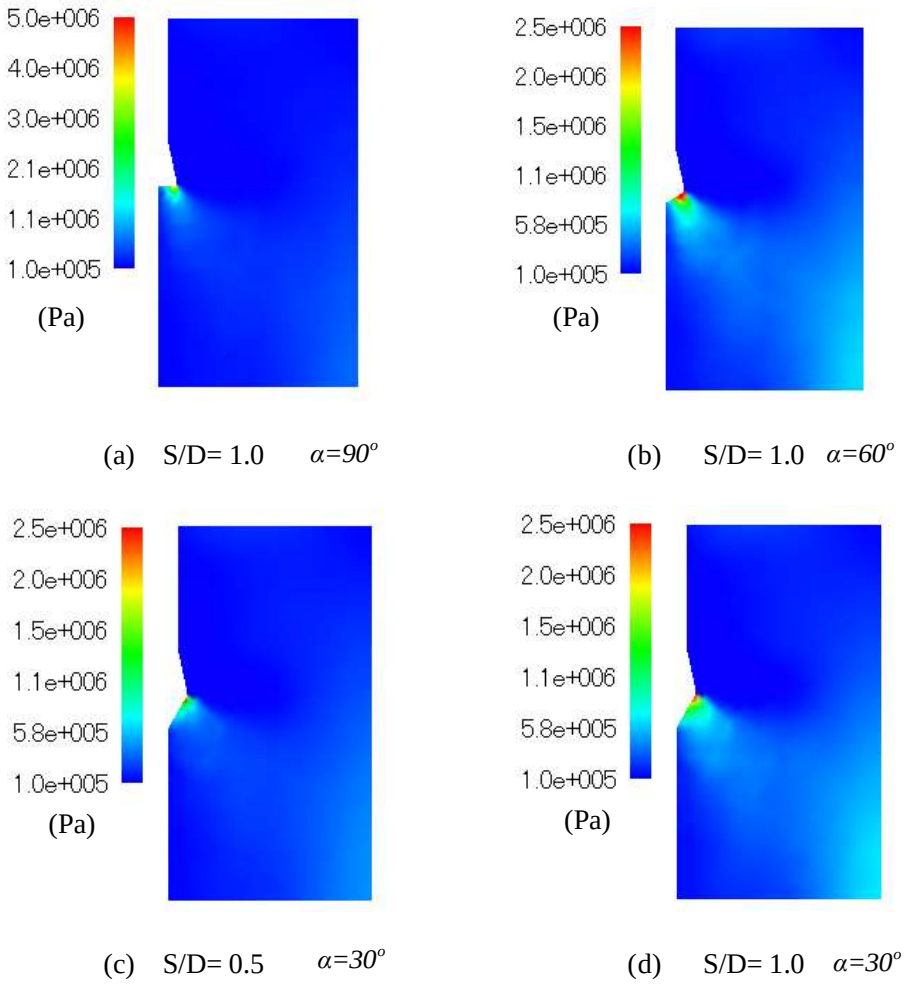

(a) S/D= 1.0 $\alpha=90^o$ (b) S/D= 1.0 $\alpha=60^o$

(c) S/D= 0.5 $\alpha=30^o$ (d) S/D= 1.0 $\alpha=30^o$

Figure 6.12 The circumferential stress contours (Surcharge pressure 200 kPa)

The distributed range of the high-value circumferential stress is one diameter length in the vertical down direction and one diameter length in the radial direction, as shown in Figure 6.12. The distributed area of the high-value circumferential stress is less affected by the pile tip shape. By comparing the

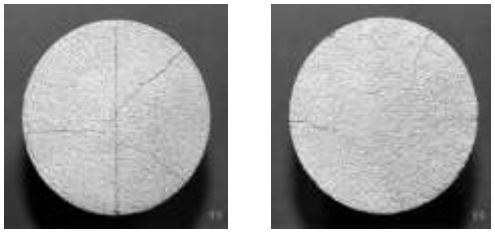

(a) $\alpha=90^o$ (b) $\alpha=60^o$

Figure 6.13 Crack failures on the surface of two pile bases (Surcharge pressure 200 kPa)

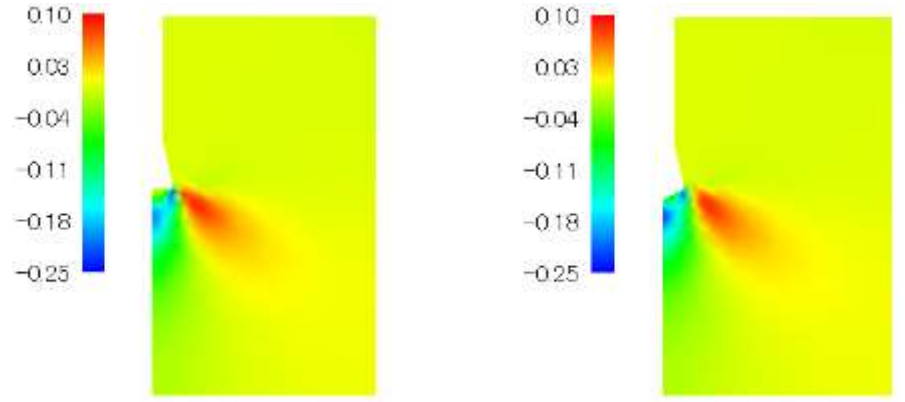

(a) S/D= 1.0 $\alpha=90^o$ (b) S/D= 1.0 $\alpha=60^o$

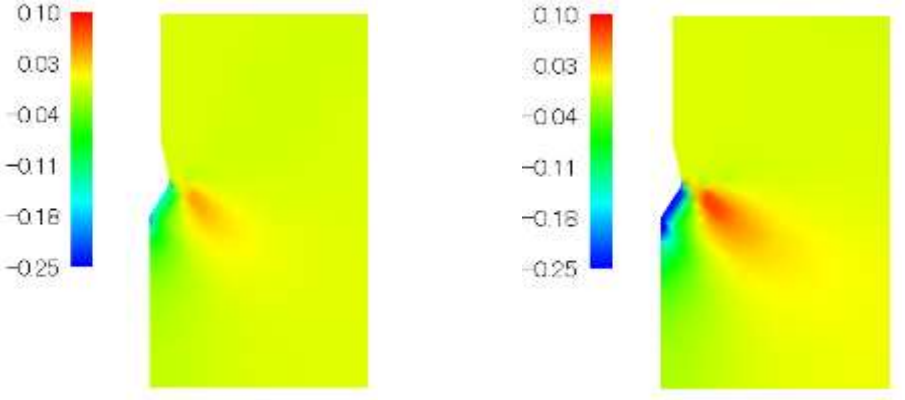

(c) S/D= 0.5 $\alpha=30^o$ (d) S/D= 1.0 $\alpha=30^o$

Figure 6.14 The radial strain contours (Surcharge pressure 200 kPa)

distribution of stress contours in Figures 6.10 (c) and 6.10 (d), Figures 6.11 (c) and 6.11 (d) and Figures 6.12 (c) and 6.12 (d), the distributed area of the high-value stress contour expands in both the vertical down and radial direction as the driving depth increases.

The high negative-value radial strain contours are just beneath the pile tip. In addition, the region of the high negative-value radial strain expands as the convergent angle decreases, as seen by comparing Figures 6.14 (a) and 6.14 (d). The high negative-value radial region is concentrated two diameter lengths in the vertical down direction. The non-irregular elliptic distribution of the high positive-value radial strain counter is located in the corner of the pile base. The results show that the volumetric

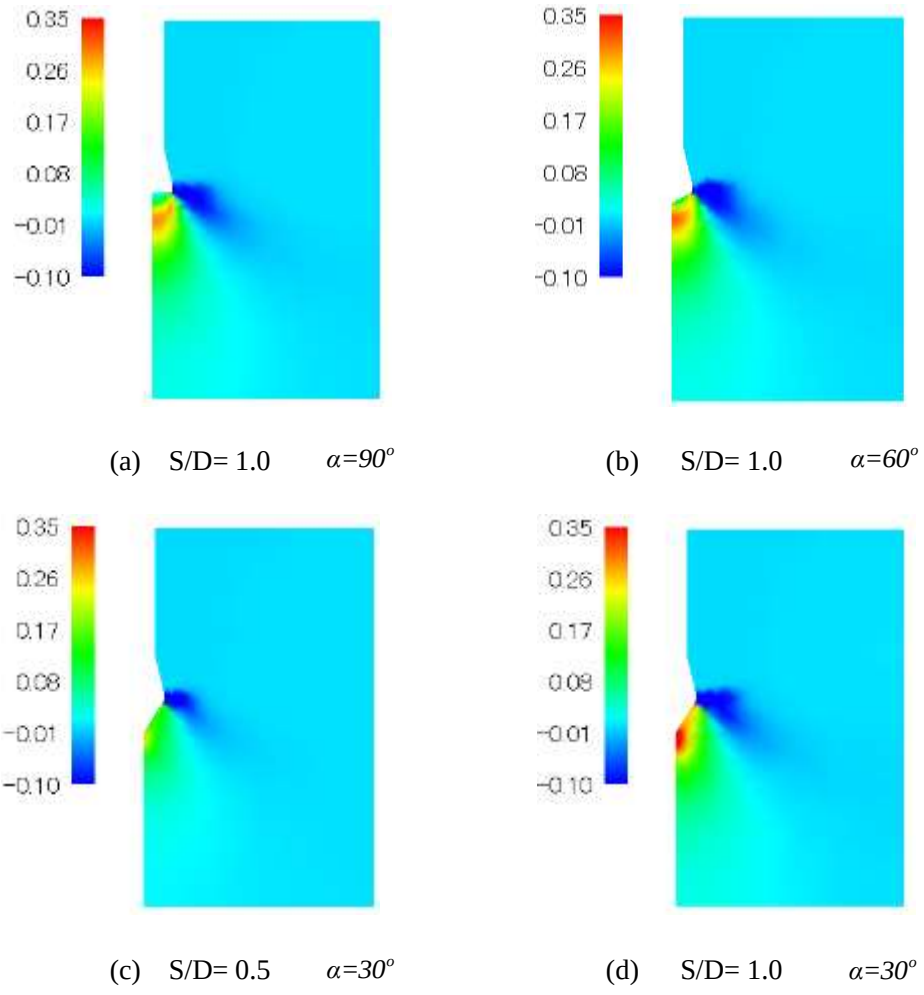

(a) S/D= 1.0 $\alpha=90^o$ (b) S/D= 1.0 $\alpha=60^o$

(c) S/D= 0.5 $\alpha=30^o$ (d) S/D= 1.0 $\alpha=30^o$

Figure 6.15 The vertical strain contours (Surcharge pressure 200 kPa)

expansion beneath the pile tip turns to volumetric compression in the corner of the pile base. Such a tendency is compatible with the predicted result by Sheng et al. (2008). The distributed area of the high positive-value radial strain is not influenced very much by the shape of the pile tip.

The high positive-value vertical strain is beneath the pile tip, four diameter lengths deep, as shown in Figures 6.15 (a), 6.15 (b) and 6.15 (d). The soil particles in this area are heavily compressed. The size of the distributed area of the high positive-value vertical strain increases as the convergent angle becomes smaller. However, the high negative-value distributed shape becomes smaller as the convergent angle becomes smaller. The high negative-value vertical strain appears around the corner of the pile base and the distributed irregular shape is not influenced by the convergent angle.

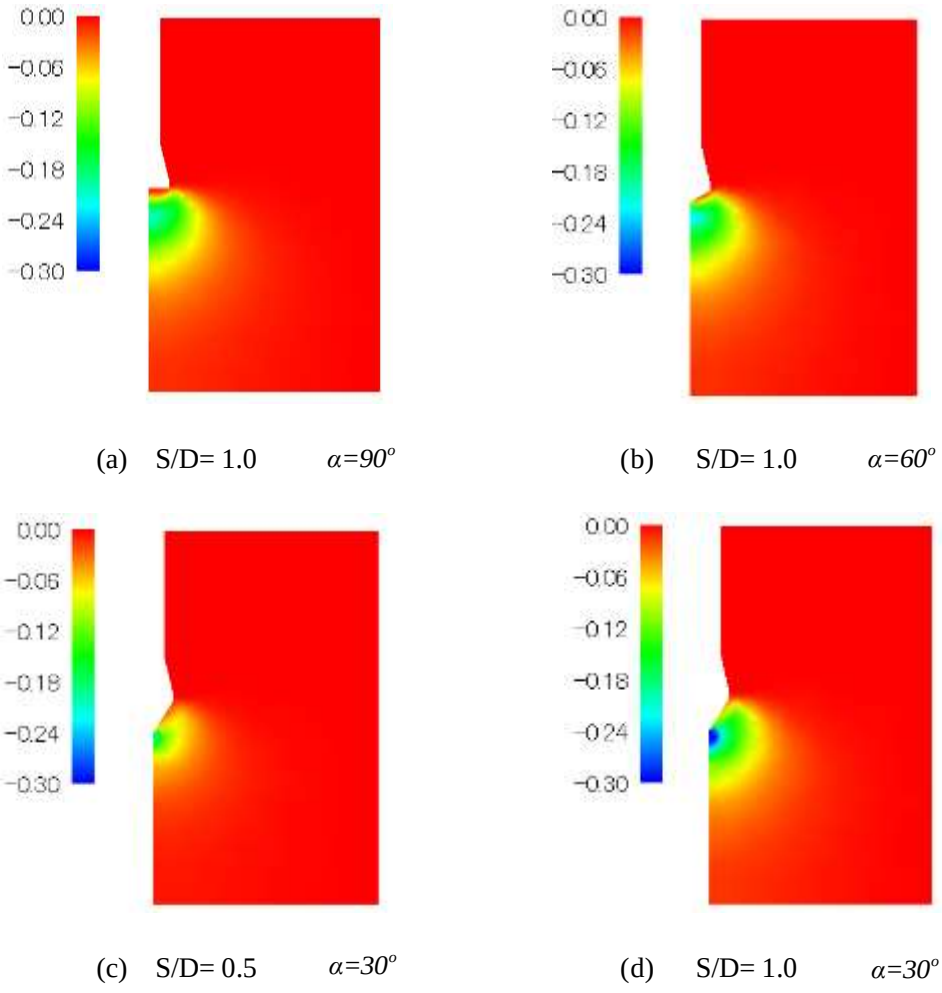

(a) S/D= 1.0 $\alpha=90^o$ (b) S/D= 1.0 $\alpha=60^o$

(c) S/D= 0.5 $\alpha=30^o$ (d) S/D= 1.0 $\alpha=30^o$

Figure 6.16 The circumferential strain contours (Surcharge pressure 200 kPa)

The distributions of circumferential strain contour are shown in Figure 6.16. The shape of the distribution of circumferential strain is elliptical. The area of the distributed elliptical shape is one diameter length in the vertical down direction and two diameter lengths in the radial direction. The minimum negative-value circumferential strain appears in Figure 6.16 (d) for the underreamed pile with a 30-degree convergent angle. The distributed shape of the high negative-value circumferential strain is affected by the pile tip shape. Moreover, the distribution of the high-value strain contours expand in both the vertical down and the radial direction with larger penetrating depth, as shown in Figures 6.14 (c) and 6.14 (d), Figures 6.15 (c) and 6.15 (d) and Figures 6.16 (c) and 6.16 (d).

6.4 Behavior of element in different depths beneath pile tip

To investigate the soil behavior of elements at different depths and to emphasize the necessity of applying the constitutive model with particle crushing in numerical computations, three elements at different depths beneath the pile tip are selected and their mechanical behavior relationships are shown.

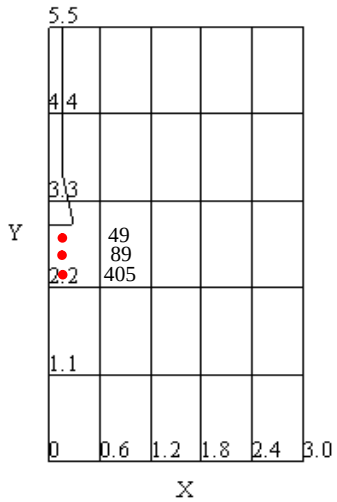

Figure 6.17 Three elements beneath pile base at different depths

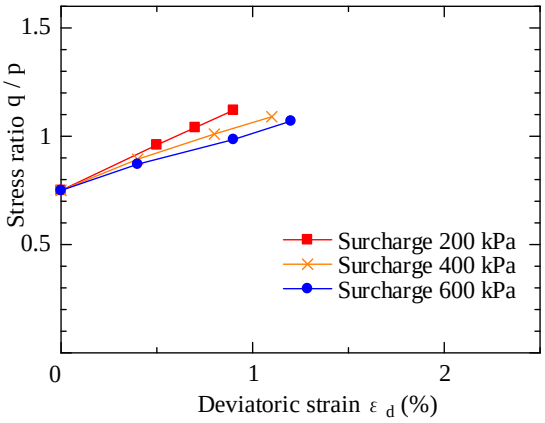

(a) Point 49

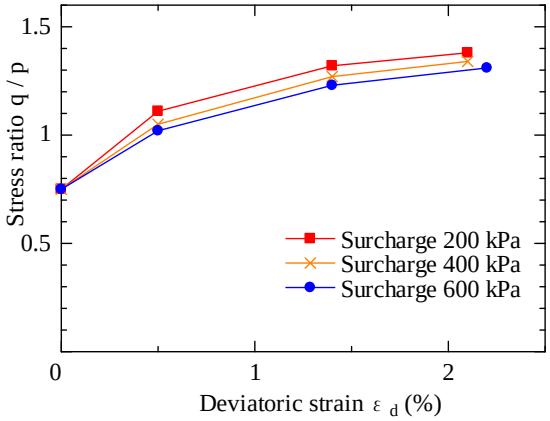

(b) Point 89

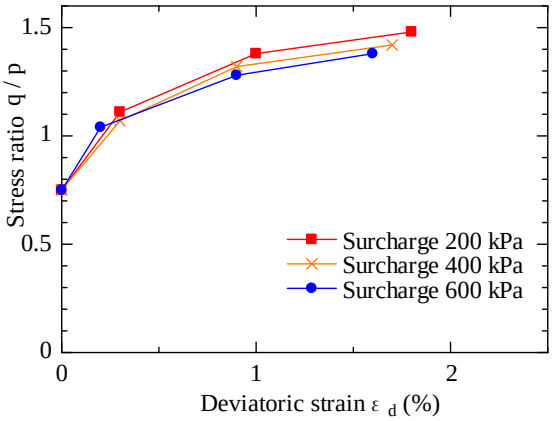

(c) Point 405

Figure 6.18 The relationship between the stress ratio and the deviatoric strain of the elements at different depth beneath pile tip

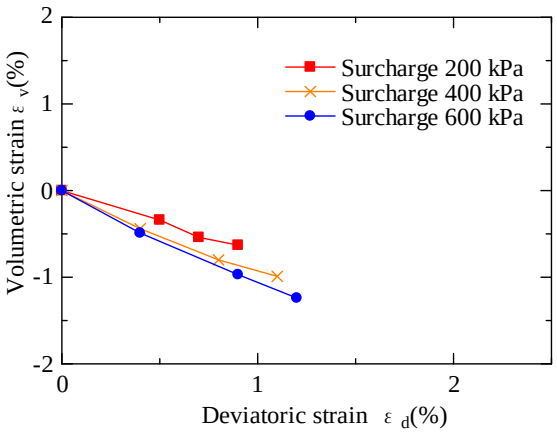

(a) Point 49

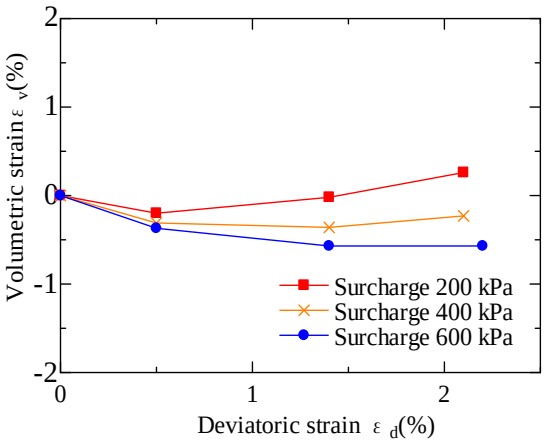

(b) Point 89

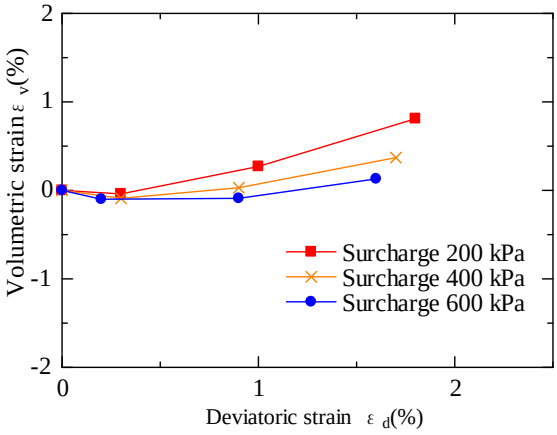

(c) Point 405

Figure 6.19 The relationship between the volumetric strain and the deviatoric strain of the elements at different depth beneath pile tip

The coordinates of Element No. 49, No 89 and No. 405 is (X= 0.12, Y=2.93), (X=0.12, Y=2.83) and (X=0.12, Y=2.28). The outline of the model ground and the three elements numbered 49, 89 and 405 are shown in Figure 6.17. Figure 6.18 shows the relationship between the stress ratio and deviatoric strain under different surcharge pressures for these three elements. Sub-titles (a), (b) and (c) of each figure indicate the predicted values of the mechanical relationship for element No. 49, No. 89 and No. 405, respectively. The stress ratio is defined as the ratio of the mean stress to the deviatoric stress. The stress ratio decreases as the surcharge pressure increases at a single element. Figures 6.18 (a), 6.18 (b) and 6.18 (c) shows that the stress ratio increases with increasing depth beneath the pile tip with the same surcharge pressure level. The initial stress ratio is 0.75 because the lateral coefficient of earth pressure is assumed to be 0.5, as in previous. The predicted results show that the deviatoric strain of element No. 89 is larger than that of the other two elements because element No. 89 is in the region of significant shear beneath the pile tip. The predicted relationship between the volumetric strain and the deviatoric strain are shown in Figure 6.19. The volume contraction and expansion of the element at different depths are reasonably demonstrated by the predicted values, as shown in Figure 6.19. In Figure 6.19 (a), the volume of the element No. 49, in the significant compressive region, shrinks under all three levels of surcharge pressure. The volume contraction is from the particle crushing and rearrangement. The degree of volume reduction increases with increasing surcharge pressure. The volume of element No. 89 contracts initially, and then expands when the surcharge pressure reaches 200 kPa. The only volumetric contraction of element No. 89 is observed when the 400 kPa and the 600 kPa surcharge pressure are applied, as shown in Figure 6.19 (b). The volume expansion of element No. 405 is predicted under all three surcharge pressures, as shown in Figure 6.19 (c). The degree of positive dilatancy becomes more noticeable as the surcharge pressure decreases. The markedly positive dilatancy tendency shown in the

model means that the confining pressure on element No. 405 is weakened.

The soil elements at different depths or positions beneath the pile base may experience various volumetric changes. Consequently, it is important to integrate the constitutive model for sand with particle crushing with finite element analysis of the model pile loading test. The extent of the volume contraction is not quite distinctive of element No. 49 in Figure 6.19 (a) and can also be attributed to the stress condition of the soil behavior just beneath the pile base, which may differ from that measured in the triaxial compression test.

6.5 Stress path of joint element

To investigate the interaction between the pile and model ground, stress path of the joint element are examined. Two joint elements near to the pile head and pile base of the flat-base model pile are selected respectively. The stress paths in joint element are shown in Figure 6.20 and Figure 6.21. The initial surcharge pressure is 200 kPa. The initial normal stress is 100 kPa.

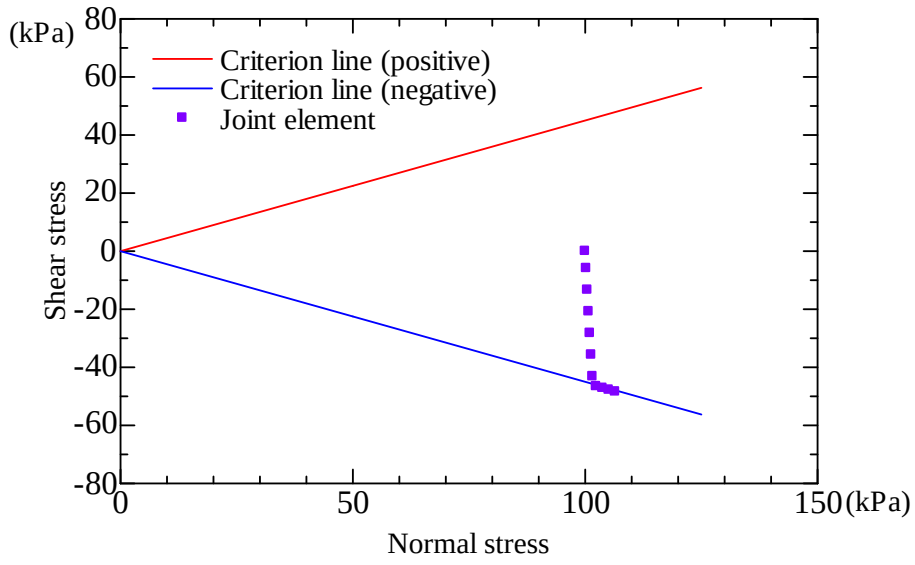

Figure 6.20 The stress path in joint element near pile head

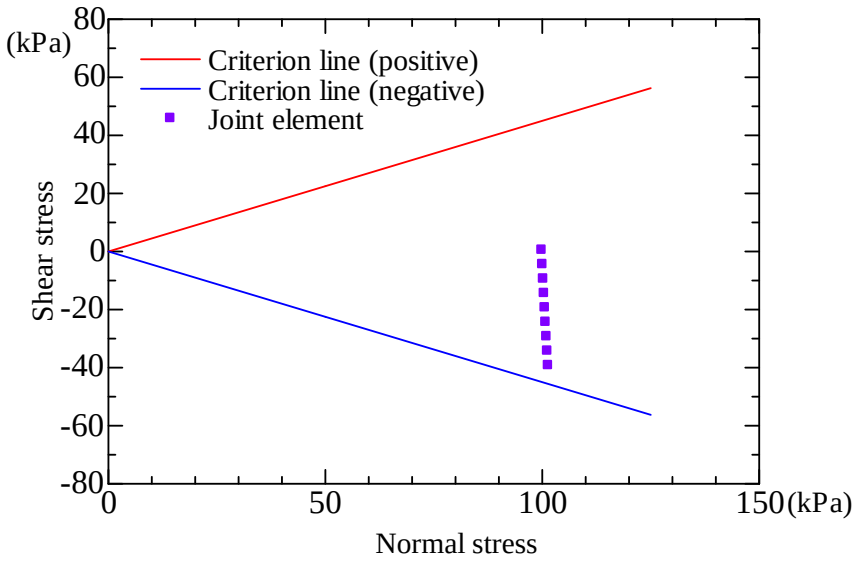

Figure 6.21 The stress path in joint element near pile base

It is shown that the stress path in the joint element near to pile head does not touch the criterion line in Figure 6.20, the slip not occurs. However, the stress path in the joint element near to pile base reaches the moves along the criterion line in Figure 6.21. Slip occurs between the pile and model ground.

6.6 Summary

To investigate the effect of pile tip shape on soil behavior around a pile, the application of finite element analysis is presented that incorporates the mixed incremental method for the UL method and the characteristics of particle crushing. The major findings of the effects on pile tip shape are summarized below.

The predicted values of the relationship between normalized bearing stress and normalized displacement of underreamed model piles agreed with the experimental results. The predicted results represent that the pile bearing capacity will decrease when the convergent angle become much sharper.

Displacement vector: The distributed range of the highest value displacement vector of underreamed pile is small that those of the pile with flat base. The distribution pattern around pile tip shows oval-shapes. In the compressive region beneath pile tip, it is observed that the angle between the displacement vector to the vertical axial become large with convergent angle decreasing.

The distribution of stress contours: The distribution area of the high radial stress contours around the underreamed pile increases as the convergent angle decreases. A significant finding is that an underreamed pile with a smaller convergent angle can prevent crack failure on the pile base surface. The distributed area of the high-value vertical stress contour is approximately three diameter lengths in the vertical down direction and three diameter lengths in the radial direction. The high-value vertical stress concentrates in the corner just beneath the pile base and decreases as the convergent angle decreases to 30 degrees. The distributed area of high-value circumferential stress is less affected by the shape of the pile tip.

The distribution of strain contours: The negative-value radial strain contours are just beneath the pile tip. In addition, the distributed region of the high negative-value radial strain expands as the convergent angle decreases. The distributed area of the high positive–value vertical strain develops beneath the pile tip and becomes more significant for the underreamed pile with a 30-degree convergent angle. The high negative-value vertical strain appears around the corner of the pile base, and its distributed shape is not influenced by the convergent angle. The distributed shape of the high negative-value circumferential strain is affected by the shape of the pile tip.

The mechanical behavior of elements beneath the pile tip at different depths is examined. The predicted relationship between the stress ratio and the deviatoric strain shows that the stress ratio variances for the three elements exhibit nearly the same tendency. The stress ratio decreases with increasing surcharge pressure for the same element. As the position of the element closes to the pile base, the stress ratio in the element decreases. However, the volumetric contraction is remarkable. Three elements display different volumetric change close to real behavior. Consequently, it is vital to integrate the constitutive model for sand with particle crushing into finite element analysis of the model pile loading test.

Reference

Dijkstra, J.,Broere, W. and Heeres,O.M. (2011). “Numerical simulation of pile intallation”, Computers and Geotechnics., 38(5),612-622.

Li, W. and Yamamoto, H. (2005). “Numerical analysis on soil behavior around pile-tip under vertical load”, Journal of Structural Engineering, 51(B), 147-157. (In Japanese)

Lobo-Guerrero, S. and Vallejo, L.E. (2007). “Influence of pile shape and pile interaction on the crushable behavior of granular materials around driven piles: DEM analyses”, Granular Matter, 9(3–4), 241–250.

Sheng, D. C., Yamamoto, H. and Wriggers, P. (2008). “Finite element analysis of englarged end piles using frictional contact”. Soils and Foundations, 48(1), 1-14.

CHAPTER 7

CONCLUSIONS AND FURTHER WORK

7.1 Concluding remarks

With demand of the higher super-structure recently, the foundation of structure is designed to provide high-level bearing capacity. The importance of sand particle crushing in significant stress region around pile tip comes to be realized. The significance of soil crushability for the design and construction of pile foundations is highlighted from a practical stand point.

The innovation of current research is that numerical analysis of pile loading is implemented in consideration of both the geometrical and material nonlinearities. The elastoplastic constitutive model and joint element are employed to represent the behavior of sand ground and interactive region between sand ground and pile. The finite element analysis incorporating large deformation theory is utilized to solve pile loading and penetration. In numerical analysis, the features representation and change during particle crushing process is emphasized.

To understand particle crushing in geotechnical engineering, the experimental and numerical studies are conducted respectively. The simple one dimensional high compression test on three kinds of granular materials is performed and the occurrence of particle crushing is confirmed. The compression loading state simulates the high stress condition existing beneath the pile tip. The numerical analysis of sand behavior, represented by the crushing model for sand with particle crushing, around tip incorporating large deformation theory and joint element is presented in this research.

7.1.1 Conclusions of <High compression test on granular materials>

The particle crushing occurrence of the three kinds granular materials in high compression test are confirmed by comparing the grain size distributed curves and directly observing the size of particle using digital microscopic before and after test. It is noticeable that particle crushing pattern of the three kinds of granular materials is quite different. The particle separates into many small pieces for Toyoura sand and Ota river sand under high compressive stress. However, the glass beads are crushed into several relative large portions. From comparing the relationship between the vertical stress and volumetric strain, it is concluded that the crushability of Ota river sand is higher than Toyoura sand and glass beads. The hardest sand is the manufacturing glass beads. The crushing ability is dependent on its component and inherent features. Owing to the limitation of the developed high compression test, the ratio of the vertical stress and circumstantial stress keep constant value during the entire loading process. From investigating the plastic work in the in interior particles under loading, the higher crushing ability the granular material owns, the more plastic work is needed for being crushed.

7.1.2 Conclusions of <Constitutive model with particle crushing and large deformation theory>

Particle crushing occurs when the outer force overcomes its strength resistance. Particle crushing is a progressively failure process and the soil particles will rearrange to another stable state again.

The constitutive model for sand with particle crushing is reviewed in detail. The constitutive model is capable of predicting the dialatancy behavior of sand from positive to negative under low confining pressure, and only the negative dilatancy under high confining pressure. This model could response the strength reduction of sand with increasing confining pressure.

To obtain more accurate and reliable numerical solutions and insightfully capture the essence of the problem, it is necessary to employ the finite element analysis using large deformation theory to tackle the pile loading and penetrating problem.

A mixed incremental method for UL method is reviewed and fully explained in this chapter. The constitutive model for small deformation theory is directly employed in this mixed incremental method and the integration process of stress and strain is equal to that of small deformation theory. This theory is suitable for description the behaviour of structure with large deformation and large rotation. The axis-symmetric finite element formulation is obtained and convenient to implement the numerical analysis.

7.1.3 Conclusions of <Effect of confining effect of model ground >

In the model test, the bearing capacity of pile in ground tank is affected by the confining from the interior surface of the ground tank. In this theoretical analysis, the diameter of ground tank is fixed as 600 mm. The diameter of model pile is assumed to be variable from 7.5 mm to 120 mm. The confining effect on the bearing capacity of pile is discussed with the different diameter ratio of the model ground and pile under the same loading condition. The meshing method for finite element computation is the same. From the relationship between the bearing stress and diameter ratio, the predicted results show that the bearing stress is less affected by the confining pressure when the diameter ratio is larger than 20. When diameter ratio is less than 10, the confined effect is serious and calculation is incredible. It is represented that the level of bearing stress decreases as surcharge pressure increases under the same pile ratio condition.

7.1.4 Conclusions of <Numerical analysis on soil behavior around pile tip >

It is encouraging that the predicted values are well agreeable with experimental results during the entire loading process. It is further observed that the normalized bearing stress decreases on the contrary although the surcharge pressure is enhanced.

The distribution of the stress value expands with larger surcharge stress and displacement. The distributed shape of the mean stress is ellipse around pile tip and becomes wider with larger surcharge pressure and displacement. The distributed shape of the deviatoric stress appears firstly near the edge of pile tip and forms the shear band. The volumetric contraction (negative dilatancy) is beneath the pile tip. The area of the predicted compression forms wedge and expands with larger surcharge pressure and displacement in down direction. The area of the predicted volumetric expansion (positive dilitancy) appears near the pile shaft because the sand particles are highly rotated and sheared. With increasing the surcharge pressure, the volumetric expansion slightly compacts because of the crushing and rearrangement of particles. The dilatancy change can be reasonably described.

The distributed shape of the deviatoric strain shows the same tendency as the deviatoric stress. The remarkable band indicating high-level shear stress is also formed. The developments of stress and strain around pile tip help us to understand the bearing mechanism of pile.

The predicted relationship between the normalized displacement and normalized bearing stress using the small deformation theory and large deformation theory are represented and compared with the experimental results respectively. The prediction accuracy by the large deformation theory and joint element is more agreeable with the experimental results.

7.1.5 Conclusions of < Effect of pile tip shape on the soil behavior around pile>

The numerical analysis on sand behavior around pile tip incorporating the large deformation and joint element is implemented. It is found that the predicted values of the relationship between normalized bearing stress and normalized displacement of underreamed model piles agreed with the experimental results. The predicted results represent that the pile bearing capacity will decrease when the convergent angle become much sharper. The distribution pattern of displacement vector around pile tip shows oval-shapes. In the compressive region beneath pile tip, it is observed that the angle between the displacement vector to the vertical axial become large with convergent angle decreasing.

The distribution of stress contours: The distribution area of the high radial stress contours around the underreamed pile increases as the convergent angle decreases. A significant finding is that an underreamed pile with a smaller convergent angle can prevent crack failure on the pile base surface. The distributed area of the high-value vertical stress contour is approximately three diameter lengths in the vertical down direction from the pile tip and three diameter lengths in the radial direction from the central axis. The high-value vertical stress concentrates in the corner just beneath the pile base and decreases as the convergent angle decreases to 30 degrees. The distributed area of high-value circumferential stress is less affected by the shape of the pile tip.

The distribution of strain contours: The negative-value radial strain contours are just beneath the pile tip. In addition, the distributed region of the high negative-value radial strain expands as the convergent angle decreases. The distributed area of the high positive–value vertical strain develops beneath the pile tip and becomes more significant for the underreamed pile with a 30-degree convergent angle. The high negative-value vertical strain appears around the corner of the pile base, and its distributed shape is not

influenced by the convergent angle. The distributed shape of the high negative-value circumferential strain is affected by the shape of the pile tip.

The mechanical behavior of elements beneath the pile tip at different depths is examined. The predicted relationship between the stress ratio and the deviatoric strain shows that the stress ratio change for the three elements exhibits nearly the same tendency. The stress ratio decreases with increasing surcharge pressure for the same element. As the position of the element closes to the pile base, the stress ratio decreases. However, the volumetric contraction is remarkable. Three elements display different volumetric change close to real behavior. Consequently, it is vital to integrate the constitutive model for sand with particle crushing into finite element analysis of the model pile loading test.

7.2 Recommendation for further research

The numerical analysis presented in this paper can be improved in some aspects.

7.2.1 More reasonable interface element

In this study, the interactive region between sand ground and pile is represented the perfect plastic model-joint element. A more advantageous model that is capable of predicting dilatancy and strength softening should be incorporated in the numerical analysis in further work.

7.2.2 Estimation the degree of particle crushing around pile tip

It is presented that the interior energy consumption accompany with the particle deformation, crushing and rearrangements. The particle crushing is quantified by different definitions of the breakage factors by measuring the change of grain size distribution curves or determined by the critical crushing stress of single particle. The description of mechanical change from energy viewpoint is more reasonable than that from only one parameter- critical crushing stress. Based on the previous experimental results, the numerical relationship between the plastic work and breakage index is well established. The computed plastic work consumption is corresponding to the breakage index in each soil particle. The prediction of the particle crushing degree benefits us to find the highly-crushed region, moderate-crushed region and slight crushed region in surrounding of pile tip. The distribution of particle crushing of sand around pile tip is significant to understand its mechanical behavior.

Besides, particle crushing is heavily affected by the shear stress acted on. The particle being exerted high shear stress is liable to be crushed, although under low compressive stress. The shear stress level is important for the further experimental and numerical studies.

Publication list regarding this study

Journal paper (refereed)

1) Yang, W., Yamamoto, H. and Yao. Y. P.: Numerical study on bearing behavior of pile considering sand particle crushing, Geomechanics and Engineering, An international Journal, 5(3), pp. 241-261, 2013.

2) Yang, W. and Yamamoto, H. : Numerical analysis of the shape of pile tip on the bearing behavior of soil around pile, Geotechnical Engineering Journal of the SEAGS & AGSSEA (under review)

3) Yang, W. and Yamamoto, H. : Finite Element Analysis with Joint Element for Model Pile under Vertical Loading, Advanced Materials Research,Vols.671-674, pp. 349-352, 2013.

Conference paper (refereed)

4) Yang, W. and Yamamoto, H. : CONFINED AND SURCHARGE STRESS LEVEL EFFECTS ON BEARING CAPACITY OF PILE IN SANDY SOIL, Proceeding of JSCE 13th International Summer Symposium, Kyoto, pp. 203-206, Aug. 2011.

5) Yang, W. and Yamamoto, H. : Numerical analysis of the underreamed pile under vertical loading in sand, Proc. of 5th International Symposium on Deformation Characteristics of Geomaterials, Seoul, Korea, pp. 941-948, Sep. 2011.

6) Yang, W. and Yamamoto, H. : Study on Sand Behaviour around Pile Tip using Large Deformation Analysis and Particle Crushing Model, Proc. of 9th International conference on Testing and Design Methods for Deep Foundations , Kanazawa, Japan, pp. 823-832, Sep. 2012 .

7) Yang, W. and Yamamoto, H. : Large deformation finite element analysis of pile behavior, Proc. of 5th China-Japan geotechnical symposium , Chengdu, China, pp.544-552, May. 2013.

Oral presentation (No-refereed)

8) Yang, W. and Yamamoto, H. : Analytical study of Un-cohesive Soil behavior using Constitutive Model with Particle Crushing, Japan architecture society Chugoku branch 2009 conference, Nishi-takaya, Proceeding of conference (CD-ROM), Mar. 2010.

9) Yang, W. and Yamamoto, H. : Study on Stress State around the Tip of Pile Foundation under Vertical Loading, Japan architecture society Chugoku branch 2010 conference, Tokuyama, Proceeding of conference (CD-ROM), Mar. 2011.

10) Yang, W. and Yamamoto, H. : Confined Effects for Vertical Bearing Capacity of Pile in Sand, Japan geotechnical society 46th national conference, Kobe, Proceeding of conference (CD-ROM), July. 2011.

11) Yang, W. and Yamamoto, H. : Study on Pile Tip Behavior considering Large Deformation Theory，Japan Architecture society annual national conference， Nagoya, Proceeding of conference (CD-ROM), Sep.2012

12) Yang, W. and Yamamoto, H. : Numerical Analysis on Sand Behavior around Pile Tip Incorporating with Interface Element , Japan architecture society Chugoku branch 2013 conference, Okayama, Proceeding of conference (CD-ROM), Mar. 2013.

13) Yang, W. and Yamamoto, H. : Experimental Study on Sand Crushing under One-dimensional High Compression Test, Geotechnical seminar of Japan geotechnical society Chugoku branch, Okayama, July. 2013

14) Yang, W. and Yamamoto, H. : Numerical Study on the Effect of Pile Tip Shape on Soil Behavior around Pile, Geotechnical seminar of Japan geotechnical society Chugoku branch, Okayama, July. 2013